STATISTICAL ANALYSIS AND CHANNEL MODELING IN NEXT GENERATION WIRELESS COMMUNICATION SYSTEMS

By

AMIT KACHROO

Bachelor of Technology in Electronics and Communication Engineering
National Institute of Technology
Srinagar, India
2009

Master of Science in Electronics and Computer Engineering
Istanbul Sehir University
Istanbul, Turkey
2017

Submitted to the Faculty of the
Graduate College of the
Oklahoma State University
in partial fulfillment of
the requirements for
the Degree of
DOCTOR OF PHILOSOPHY
May, 2021

STATISTICAL ANALYSIS AND CHANNEL MODELING IN NEXT GENERATION WIRELESS COMMUNICATION SYSTEMS

Dissertation Approved:

Dr. Sabit Ekin

Dissertation Advisor

Dr. Subhash Kak

Dr. Charles Bunting

Dr. Lan Zhu

ACKNOWLEDGMENTS

First and foremost, I would like to thank my parents, and my sister for their immense patience, and support during this Ph.D. time and in general. Being a first generation college student from a remote part of the world, the struggles can get sometimes very intense, and without their constant help and support, this journey to Ph.D. (first in the family) would not be possible.

Secondly, I would like to express my sincere gratitude to my advisor, Dr. Sabit Ekin for his continuous support and guidance during this Ph.D study. I can't think of an adviser, who drove a U-haul truck with his graduate student (me) in the back with robotic arm in the lap to move it to an anechoic chamber for research. He has been a great mentor, and most importantly, a good friend. Besides my advisor, I would also like to thank, Dr. Subhash Kak for his tremendous support, motivation and guidance throughout my stay in USA. He has been like a family member, who has constantly inspired and motivated me.

Last not but the least, I would like to thank my Ph.D. committee members: Dr. Charles Bunting, Dr. Lan Zhu, and Dr. Subhash Kak; TWISTER team members: Dr. Wooyeol Choi, Dr. John O'hara, and Dr. Ichkyun Song; Dr. He Bai, Dr. Keith Teague, and Dr. James West for their kind help and guidance during my time at OSU. I would also like to put on record special thanks to Dr. Wooyeol Choi, without whose guidance and knowledge, the research project on millimeter wave would not have been possible. I would also like to mention, Hisham, and all the undergraduate students with whom I had the opportunity to work as a GTA in the ECEN 2714/2011 course for almost 3 years, for their friendship, support and help during my time at OSU.

Acknowledgments reflect the views of the author and are not endorsed by committee members or Oklahoma State University.

Name: AMIT KACHROO

Date of Degree: MAY, 2021

Title of Study: STATISTICAL ANALYSIS AND CHANNEL MODELING IN NEXT GENERATION WIRELESS COMMUNICATION SYSTEMS

Major Field: ELECTRICAL ENGINEERING

Abstract: In this thesis, statistical analysis and channel modeling in next generation wireless communication systems is presented in detail. The primary focus of this thesis is on the statistical modeling of interference temperature (IT) in cognitive radio systems, and empirical study of wireless channel characterization of unmanned aerial vehicle (UAV)-assisted communications at ultra-wideband (UWB) and at millimeter wave (mmWave) frequencies.

Firstly, in the cognitive radio system, a novel idea to statistically model the dynamic interference threshold (IT) from user traffic demand is presented in detail. It is shown that the cognitive radio system with dynamic IT will have high capacity performance with less outage probability over a system that does not utilize dynamic IT. The detailed theoretical analysis with expressions for mean capacity and outage probability in general operation region, and in high power region are derived and subsequently, validated with the simulations results. In addition, the effect of secondary user interference on primary user is also examined in this part.

In the second part, wireless channel characterisation for unmanned aerial vehicle-to-wearables (UAV2W) at UWB frequency is analysed, and studied empirically in an indoor warehouse environment. The frequency and distance dependent path gain analysis at different bandwidths for a corresponding carrier frequency with time dispersion characteristics is presented in detail. Furthermore, from statistical modeling, it was shown that the Log-normal distribution is the best fit distribution model to characterize fading in these UAV2W systems.

Finally, a novel emulation method for UAV motion by a robotic arm is presented to study the mmWave channel characteristics (Doppler spreading and path loss) at 28 GHz. In addition to that, empirical study is carried out to analyze the propeller modulation effect caused by the propellers in UAVs with an actual UAV setup. These important statistical analysis, and channel modeling discussed in this thesis are very critical in designing, analysing, and in implementation of fifth generation (5G) and beyond 5G (B5G) communication for the future. This thesis is a stepping stone in that direction.

TABLE OF CONTENTS

LIST OF TABLES

LIST OF FIGURES

CHAPTER I

INTRODUCTION

Since its inception in the early 1980s, wireless communication systems have seen a lot of technological advancements and development over time. From the very early popular wireless technology of Advanced Mobile Phone System (AMPS), Global System of Mobile Communication (GSM) or Code Division Multiple Access (CDMA) to Wideband Code Division Multiple Access (third generation) systems, from third generation (3G) to fourth generation or LTE (Long Term Evolution), and from fourth generation (4G) to presently considered fifth generation (5G) or beyond 5G (B5G) networks, the technological development is still going on. This is mainly because of the increase in the user proliferation and devices with the ever increasing demand of high data speed for data obsessive applications and services. Although, this wireless technology evolution has been revolutionary in terms of data speed, it never caught up with the high data demands over the years. Now, even more data obsessive applications, such as mobile games or augmented reality applications etc. are coming into picture, in addition to the rise in devices owned by users, which will certainly put a lot of stress on the available wireless spectrum. Additionally, the inefficient use of radio resources in wireless communication systems aggravates this problem even further.

To overcome such challenges, not only do we need high bandwidth and high frequency systems, such as ultra-wideband (UWB) or millimeter wave (mmWave), but also the efficient utilization and optimization of spectrum is a must. Moreover, in recent times, the advancements in Unmanned Aerial Vehicle (UAV) assisted communication is playing a vital role in future 5G and B5G technologies. This thesis covers this in-depth study of next generation UAV-assisted wireless communication systems at UWB and at mmWave frequency band, and also focuses on the theoretical study of optimizing the spectrum usage in cognitive radio network (CRN) by studying and statistical modeling the dynamic interference temperature (IT) in CRN. This statistical modeling of dynamic IT, and its advantages over fixed IT systems is shown in Chapter II.

The use of UWB in UAV-assisted communication with wearable antennas is also referred to as ultra wide-band unmanned aerial vehicle to wearable (UAV2W) communication systems in this work, which is studied in an indoor warehouse environment. The mmWave on the other hand is studied by utilizing a novel emulation framework with the aid of a robotic arm in an anechoic chamber type environment. The mentioned scope of this thesis is also shown in Fig. 1. The understanding of the performance of these UAV-assisted next generation wireless networks at ultra-wide band (UWB) and at mmWave frequencies is very critical in successful design, analysis, and in implementation for future wireless communication systems. In this chapter, an overview of wireless technology evolution, an overview of cognitive radios, UAV-assisted UWB wearable technology and UAV-assisted mmWave technologies will be discussed

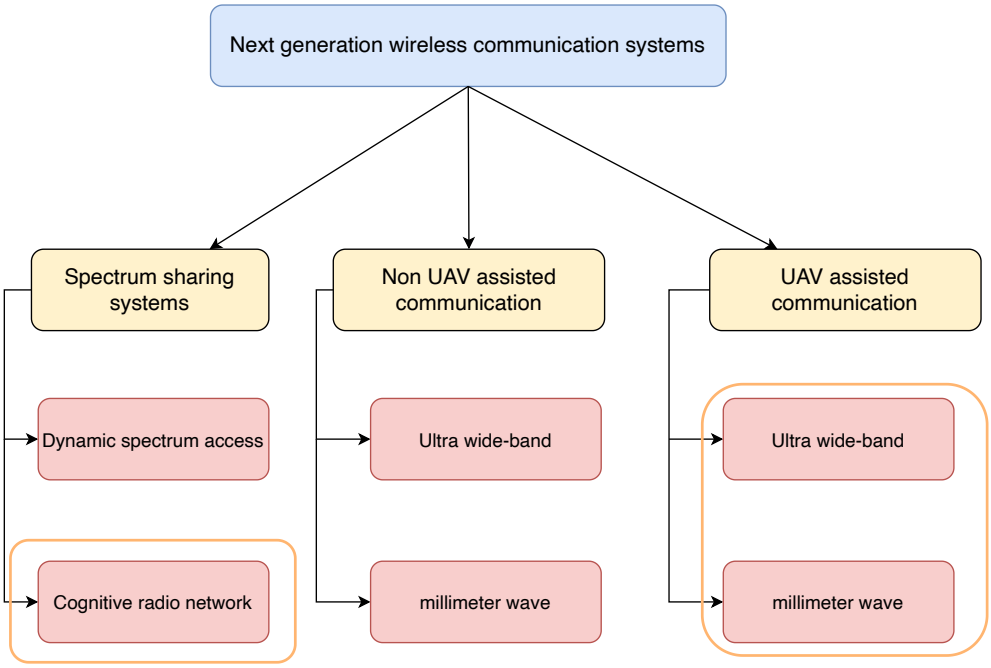

Figure 1: A brief overview of the next generation wireless communication systems. The ones that are considered in this thesis are shown in a box.

briefly in the coming sections.

1.1 Evolution of Wireless Technology

The evolution of wireless technology started in the 1980s with the advent of AMPS, also referred to as first generation (1G) systems. It was revolutionary technology at that time which allowed multiple user connections to a base station (BS), and also allowed hand-off between multiple BSs. This was later replaced by second generation (2G), 3G, 4G, and now with 5G. One interesting point to observe with this evolution or change in wireless technology is that this happens in increments of decades (Fig. 2). The initial wireless communication technology in the 1980s supported only voice, which then in 2G started to support text messages and data in the 1990s. It then further evolved to support high data rates in excess of megabits per second with other services such as text and voice in 3G. Now, with the advent of fourth generation (4G) or LTE networks, it is now possible to even live stream high-definition videos, play real-time games, and access other multimedia content with better quality of service (QoS).

This technology evolution over decades from 1980 to 2020 can be visualized in Fig. 2. One can also easily observe the exponential increase in the data rates from mere 2.4 Kilobits per second (Kbps) to 9.6 Kbps, and then to ∼100 Megabits per second (Mbps) in LTE, and to be more than 1 gigabits per second (Gbps) in the proposed 5G technologies. However, with the increase in the data speed, there is also the exponential growth of smart devices and users that has far exceeded the supported capacity of the present wireless technology. Therefore, to cater to this ever increasing user demand and access, 5G and B5G systems are now being considered. These systems will use UWB frequencies (3.1-10.6 GHz), and

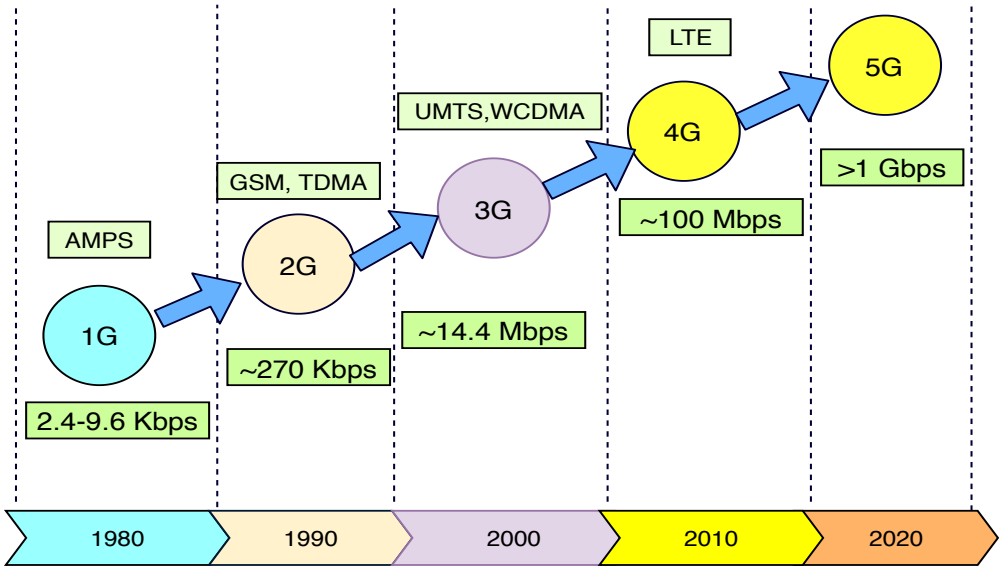

Figure 2: Evolution of wireless technology over time.

mmWave frequencies that range from 30 GHz to 300 GHz. Utilizing such a high frequency and high bandwidth technology improves the overall data rate by a factor of 1000.

Recently, UAVs have also been shown to assist these next generation technologies (UWB and mmWave) to increase connectivity with high data speeds. Therefore, study of UAV-assisted next generation technologies is a very important step in its realization for everyday use. Also, the optimization of the available wireless spectrum is very important to realize the efficient utilization of the available radio resources. This optimization of radio resources, especially in CRNs has become a topic of focus in academia and in industry for some time. In this thesis, the empirical study of these UAV-assisted next generation wireless technologies, and theoretical statistical modeling of cognitive radio systems is presented in detail. Before moving on to the overview of these next generation wireless communication technologies, a brief overview of a wireless communication system is presented in the next section.

1.2 Cognitive Radio Systems

Cognitive radios are radio devices that can be dynamically configured and programmed to use the available wireless resources in an optimal way. The main idea behind using CRs is to improve the spectrum efficiency and enhance network performance. CR was first defined and originally coined by Mitola [1] in a seminar at KTH (the Royal Institute of Technology in Stockholm) and later on, in his research paper in 1999 [2]. He defined CR's as, "a really smart radio that would be self, RF (radio frequency) and user aware, and would include language technology and machine vision along with a lot of high-fidelity knowledge of the radio environments". The other well known definition came from Simon Haykin [3,4]. He described it as, "cognitive radio is an intelligent wireless communication system that is aware of its surrounding environment (outside world), and uses the methodology of understanding-by-building to learn from the environment and adapt its internal states to statistical variations in the incoming RF stimuli by making corresponding changes in certain operating param-

eters (e.g., transmit-power, carrier-frequency, and modulation strategy) in real-time, with two primary objectives in mind: 1) highly reliable communications whenever and wherever needed and 2) efficient utilization of the radio spectrum". The important terminology to notice from Haykin's definition are awareness, intelligence, learning, adaptivity, reliability, and efficiency [4]. All these terms are associated with the CR principles, sometimes referred to as the spectrum sharing principles. The shared spectrum access model of CR highlights the concepts of primary user (PU) and secondary user (SU). PUs are defined as the licensed users of the spectrum whereas the SUs are the unlicensed users which have the capability to access the licensed spectrum opportunistically.

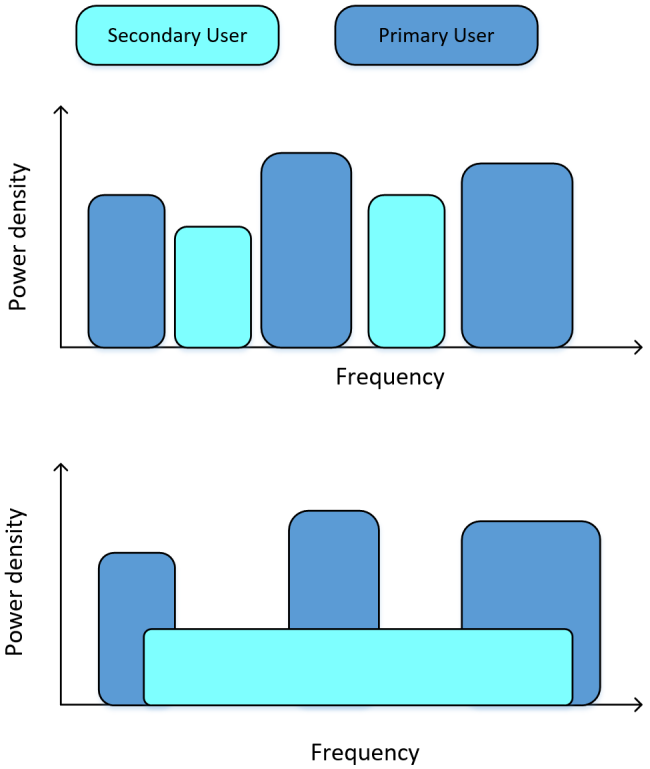

Figure 3: Spectrum overlay and spectrum underlay access methods.

The opportunistic spectrum access by a SU is done mainly by two ways (Fig. 3),

- *Spectrum overlay*: This is a very conservative spectrum access approach, where the SU accesses the frequency spectrum, if and only if it is free or not being used by any PU. This method requires sensing of the white spaces available in the spectrum before accessing it.

- *Spectrum underlay*: In this access method, the SU and PU can access the spectrum concurrently, provided that the SU transmit power does not interfere with the PU transmissions. The transmit power threshold enforced by PU makes sure that the QoS is not affected at PU-Rx. This threshold is also known as interference temperature (IT) [5–7], which plays an important role at SU for transmit power adaptations.

In this thesis, the underlay network is assumed where the SUs adapt their transmit power to maintain the required IT constraint. To maintain IT, SU will either adapt its peak or average transmit power [8–11]. Traditionally, the interference power threshold or IT for SUs is kept constant, however, some studies, such as [12] have thoroughly analyzed the concept of interference probability in a relay assisted CRN, assuming imperfect channel state information (CSI). Further, the well-known main requirement of CRN is to maintain QoS of PUs (legacy users), while aiming at increasing spectral efficiency of the whole system by allowing SUs to access the spectrum opportunistically. However, fixed IT constraint is considered a strict requirement for satisfying this QoS of PUs. Therefore, this idea of studying dynamic IT [13] in CRN was considered in this thesis, and is discussed in great detail in Chapter II.

1.3 Unmanned Aerial Vehicles in Wireless Communication Systems

Besides optimizing the available spectrum for efficient usage, UAVs, also referred to as drones, are now considered to be one of the main contributing factors for the next generation of UAV-assisted wireless communication systems. With the exponential growth in the consumer UAVs, it is a very promising business prospect for all the network operators as it brings extra revenue when these UAVs are connected to their network. It also opens up another opportunity for these cellular operators where a UAV can itself be used as a base station (flying base station), which gives an advantage of better coverage, spectral efficiency and high user quality of experience (QoE). The growth in drone fleet is expected to double in 2022 to 2.4 million compared to 2014 (1.1 million) [14]. Standardization bodies such as Third Generation Partnership Project (3GPP) are looking into the are looking into the aspect of using UAVs in cellular networks [15–17]. 3GPP refers to this as aerial user equipment (UE) by having UAVs serve as another UE. Academia, on the other hand, is not only looking at it as a UE but also as BSs or relays. In addition, Electronic Communications Committee (ECC) within the European Conference of Postal and Telecommunications Administrations (CEPT) in Europe is also looking into the aspects of spectrum regulations in UAVs [18]. The International Telecommunication Union Telecommunication Standardization Sector (ITU-T) is working on defining capabilities of UAVs in the service and application support layer for integration of UAVs in IMT-2020 networks with high security protocols [19]. The European Telecommunications Standards Institute (ETSI) technical report (TR) 103 373 is defining the UAV-specific use cases and deliberating on the spectrum rules that may be required to enable the UAV based communication [20], and finally, the Institute of Electrical and Electronics Engineers (IEEE) had a drones Working Group in 2015. The aim is to develop a standard for consumer drones while putting emphasis on privacy and security concerns [21, 22].

The main advantages of UAVs are that they are very easy to operate remotely or autonomously, and hence, can be easy deployed anywhere. UAVs also have higher maneuverability, lower operating and maintenance costs, and are highly capable of providing a highly reliable and cost effective mode of communication [23–27]. UAVs have been deployed as a flying BS to provide ubiquitous wireless communication access, and as an alternative support for 5G and B5G cellular mobile communication. Furthermore, UAVs can be used as mobile relays to provide wireless connectivity among partitioned UEs that lack any direct

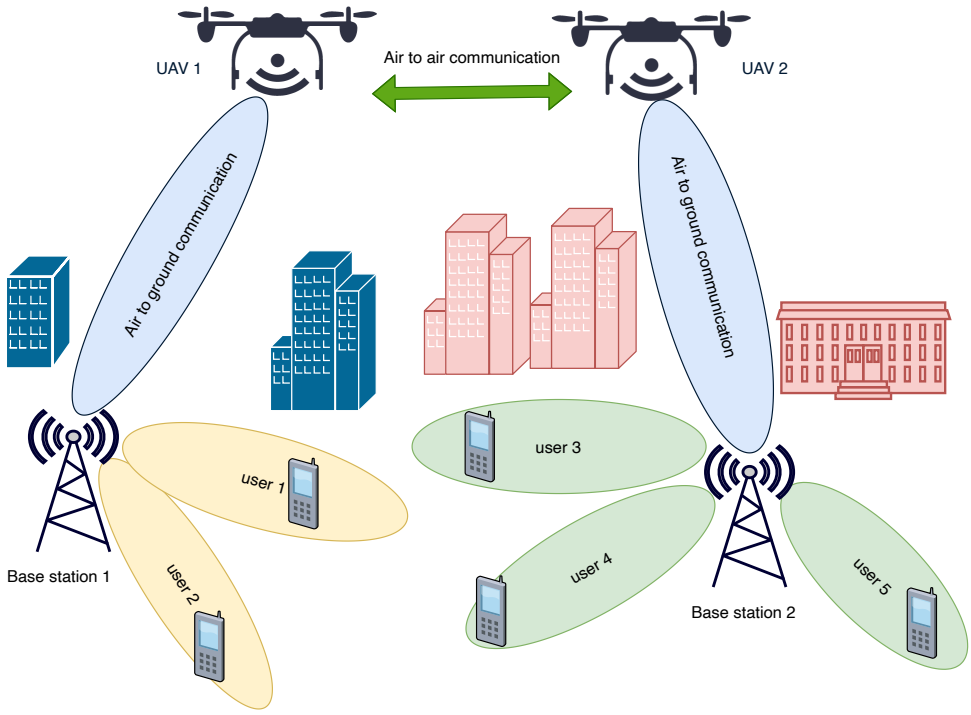

Figure 4: UAV-assisted wireless communication system.

line of sight (LOS) communication between the BS and UE. This can be visualized in Fig. 4, where user-2, and user-5 do not have LOS between them as there is no communication link between BS-1 and BS-2, and user-2 is connected to BS-1,and user-5 is connected to BS-2. However, with air-to-air communication link between UAV-1 and UAV-2, user-2 and user-5 can communicate with each other. Other than using UAVs as a flying BS or relay, UAVs have found application in areas such as aerial data collectors, aerial caching, and aerial power source etc. Multiple UAVs can also coordinate, and self organize to form different network architectures such as flying adhoc networks (FANETs), internet of drones etc.

1.4 Challenges with UAV-assisted Wireless Communication Systems

There are many new challenges associated with a UAV-assisted next-generation wireless communication system, especially if it has to serve as a flying BS. Some of these challenges are, a) placement optimization- this problem becomes a 3D-placement optimization problem, where the objective can be maximizing system capacity or minimizing interference from these flying BSs to the cellular network [28, 29], b) Power efficiency- This is one of the most challenging problem with UAVs, the limited power. The only way to conserve power is to have efficient scheduling algorithms, or to minimize the transmit power of these aerial BSs [30–32]. There are now studies in optimal scheduling of beacons, and minimizing transmit power but a real proof of concept is still missing. Apart from reducing energy, recharging of UAVs is another idea to increase their short lifetime. However, it is a very complex issue as recharging or replacing points need to be properly designed especially in crowded urban areas [33, 34], c) Security- Due to its unmanned nature, the security with UAVs as flying

BS becomes more important than ever. Cases of eavesdropping, jamming, denial of services (DoS), spoofing and hijacking can be very real with these type of platforms. Thus, there is a big need of research and application for secure wireless communication protocols in these UAV-assisted wireless communication networks.

Last, but not the least, as we move towards high frequencies in the radio frequency spectrum, the need to have a realistic channel model in UAV-assisted communication become more crucial. Presently, UAV-assisted communication has become more reliable with tested channel models in sub-6 GHz channel but not much has been done for frequency beyond that. Most of the research with UWB and mmWave is picking up for the UAV-assisted communication but most of it relies either on simulations based on ray tracing software and lacks any empirical data. This is one of the challenges being addressed in this thesis. Fig. 5 shows these unique challenges, with UAV types, and the standardization efforts going on with the UAV-assisted next generation wireless communication.

At present, mainly simulation based studies are being used to study UAV-assisted communication at UWB and mmWave band. One of the main reasons behind this dependence on simulation software is the constraint in flying the UAV itself because of the regulations imposed by Federal Aviation Administration (FAA) [35]. These rules include that the UAVs have to maintain a visual line of sight from the pilot at all times, the maximum flight height has to be 400 feet (122 meters) above ground, maximum speed is set at 100 mph (161 Km/h), while the maximum weight has to be 55 pounds (25 Kg). In addition to that, only daylight operations are permitted with strict flying restrictions near areas such as airports, hospitals, public areas etc., and for certain operations, a licensed pilot is required.

In this thesis, after the theoretical studies of cognitive radio networks, empirical study of UAV-assisted wireless communication systems is covered in detail.First, the unmanned aerial vehicle-to-wearables (UAV2W) at UWB frequencies are examined, and then the emulation of UAV motion to study mmWave channel characteristics at 28 GHz is examined in detail, and finally, the propeller modulation effect in UAVs is also considered to fill the lacunae caused by the lack of field data. In the coming sections, first the UAV-assisted UWB and then the UAV-assisted mmWave technology will be discussed briefly.

1.5 Ultra-wideband Technology for Unmanned Aerial Vehicle-to-Wearables System

UWB is a very popular radio technology that works at a frequency bandwidth of more than 500 MHz. The main reasons behind its popularity are the low-power consumption and high bandwidth with low probability of interception [36–39]. The low power consumption and short wavelength make the UWB a best possible candidate for the body-centric wireless network [40, 41] in health-care applications [37, 38]. The Federal Communication Commission's (FCC) power requirement of -41.3 dBm/MHz or 75 nanowatts/MHz classifies UWB as an unintentional radiator which allows it to lie near the noise floor for a narrowband receiver, and thereby allows it to coexist with current wireless technologies, such as WiFi with minimal or no interference at all. In summary, the main advantages of UWB can be listed as follows,

- Low power consumption with high data rate. The received power in UWB lies very

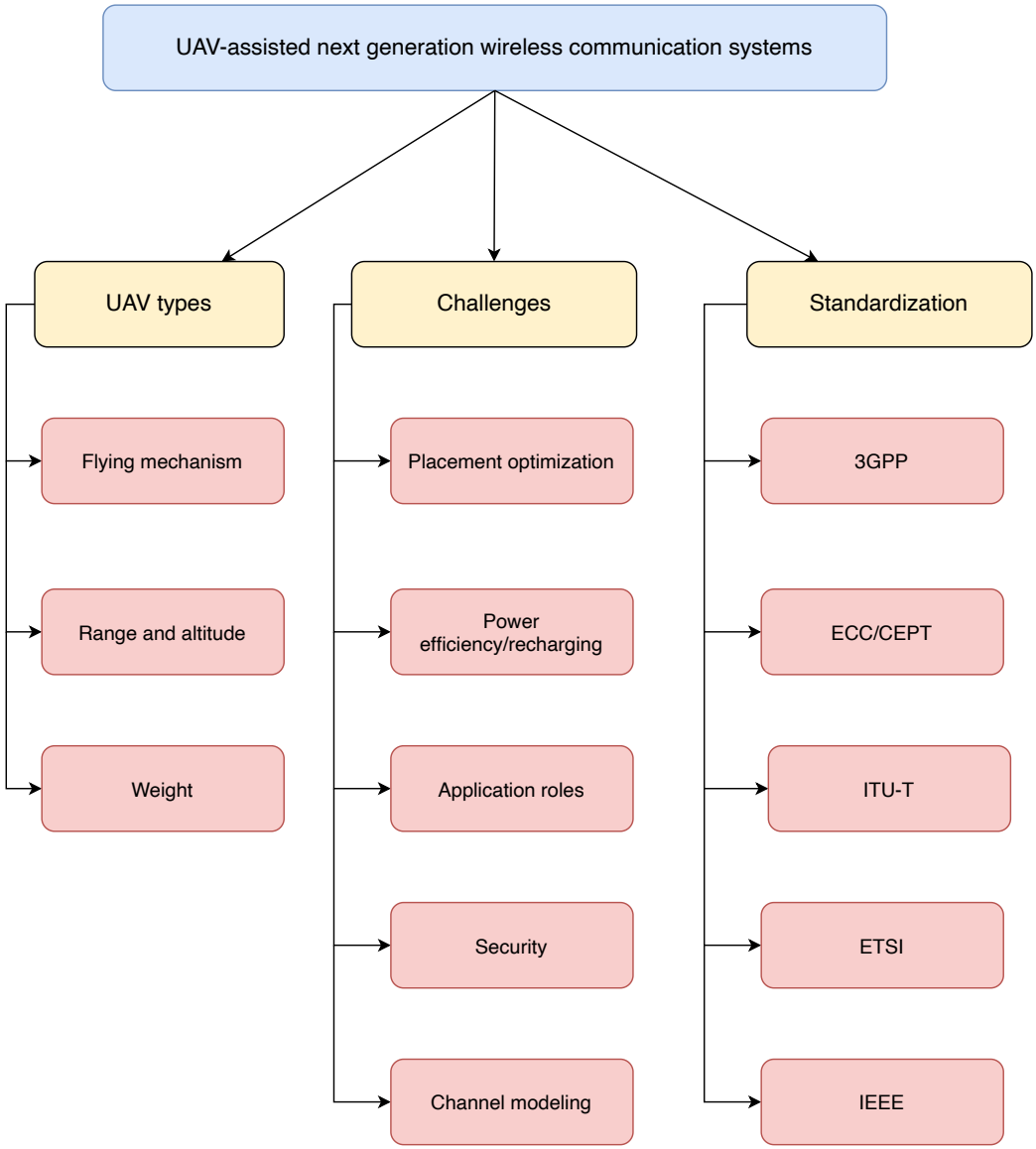

Figure 5: A top view of the UAV-assisted next generation wireless communication systems.

close to the noise floor [36–39, 42].

- Control over duty cycle makes the battery last longer.
- Low probability of detection as it is close to the noise floor and any attempt of jamming or eavesdropping will make the signal noisy [43].
- Small wavelength with low power makes it a perfect fit for body-centric wireless network [37, 38].

Because of all these advantages, one of the major applications of UWB is in the body area networks or with UAV to wearable devices. Fig. 6 shows an example of a UAV to wearable system used for health monitoring applications. These systems are referred to as unmanned aerial vehicle-to-wearables (UAV2W) systems in this thesis [42].

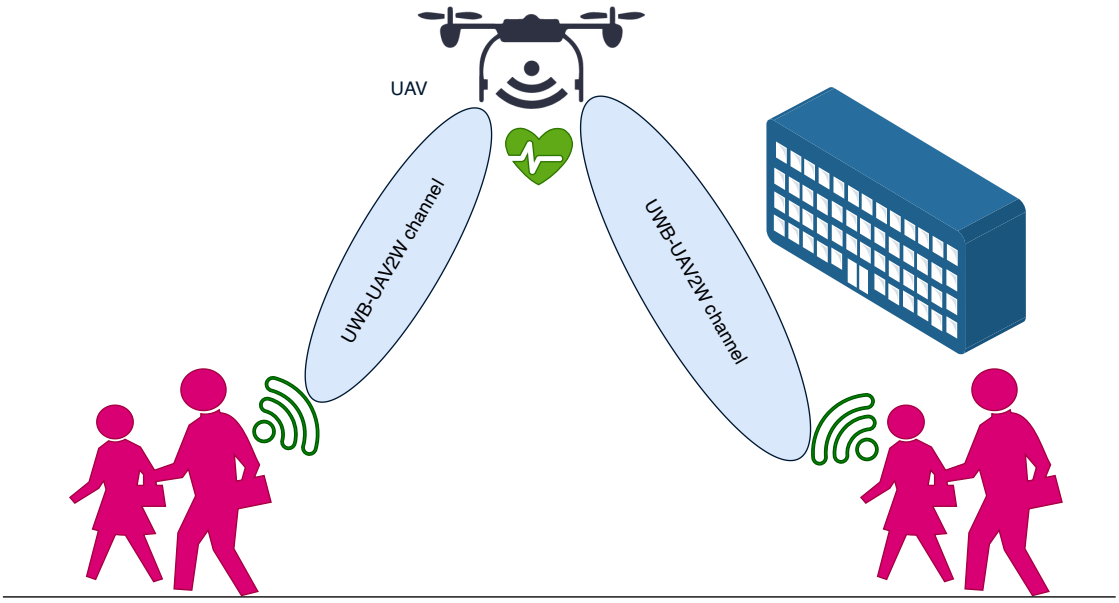

Figure 6: An example of a UWB-UAV2W health monitoring system.

In this empirical study, the operating-frequency range that is considered is from 3.1 GHz to 10.6 GHz with different sub-bandwidths at corresponding different central frequencies. In Chapter III, this in-depth empirical study and modelling of the distance and frequency dependent path loss factors at different bandwidths, and time dispersion characteristics of UAV2W system at UWB frequency is examined in detail.

1.6 Millimeter Wave Technology for Unmanned Aerial Vehicle Assisted Communication

After studying UAV2W at UWB frequency, the next topic of this thesis is to examine UAV-assisted mmWave communication systems, especially channel characteristics such as Doppler spread and path-loss, and also the propeller modulation effect at 28 GHz. In 2015, FCC released millimeter wave frequencies for licensed and unlicensed use. The newly licensed frequencies are 28 GHz, 37 GHz, and 39 GHz, while the unlicensed bands are 64∼71 GHz [44]. Access to these mmWave frequencies allows multi gigabit wireless communication which will enable 5G and B5G communications. In addition to the high data rates, small antenna size, and circuits at millimeter wavelength provide reliable, highly directional and secure communication links against any eavesdropping and jamming. However, mmWave communication suffers highly from the propagation attenuation, shadowing effect (blocking), beam misalignment, and Doppler shift [45–48]. Doppler spread becomes more critical when there is movement of transmitter or receiver or both with respect to each other. In addition to that, as the wavelength is very small (millimeters), these Doppler effects become more prominent.

It is also well known that in a given mobile and multipath environment, each multipath component (MPC) will experience a different Doppler shift according to the motion, which leads to the spectral broadening at the receiver. This spectral broadening causes erroneous

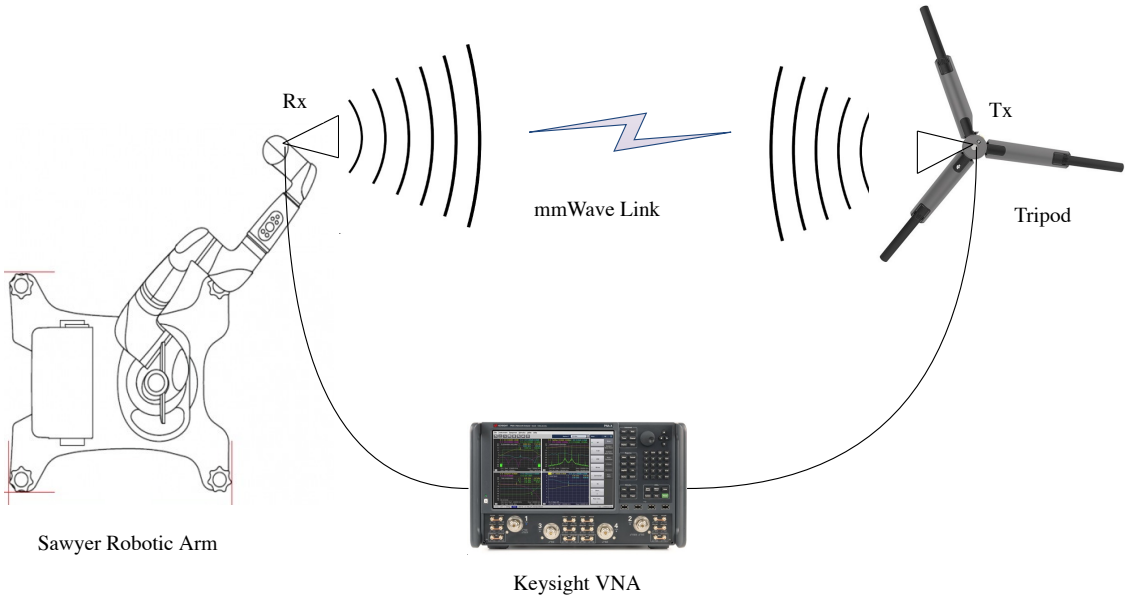

Figure 7: Top view of the measurement study setup. The transmitter is placed on the end of the robotic arm, while the receiver is hooked on the tripod.

signal reception or communication failure for a communication network. Therefore, modeling physical UAV motion as close as possible to an actual UAV motion is very important in understanding the design constraints, and performance of a mmWave based UAV communication system. Techniques to analyze and combat the Doppler effects have been studied extensively, which as mentioned previously are based on simulations that ignore the actual UAV motion, and UAV dynamics under real atmospheric conditions (wind gusts) [23, 26, 49].

Thus, to properly analyze and study the mmWave channel characteristics, such as Doppler and path-loss, emulating actual UAV motion under wind gusts is very much required. In this thesis, the close to the real UAV motion is emulated by a robotic arm in an anechoic chamber with wind gusts modelled by the famous Dryden wind model. The measurement study setup for such a case is shown in Fig. 7. The complete analysis and statistical characteristics of mmWave wireless communication channel is discussed in detail in Chapter IV.

Moreover, the propeller modulation caused by the propellers in the UAV is also investigated in this chapter. This modulated waveform at the receiver is basically an amplitude modulated wave because of the propeller. In this work, propeller modulation with a real UAV (hexcopter) is studied for the first time at 28 GHz. The correlation between propeller speed and its corresponding frequency component is also investigated in great length. A set of experiments with UAVs at different heights, and with different permutations of propeller-on and -off between Tx and Rx is conducted in detail.

1.7 Contributions

The overall contributions of this thesis can be summarized as follows,

- Statistical modeling of dynamic interference threshold and its effect on network capacity and outage probability in CR is presented in detail. The derived theoretical expressions are verified with simulation results, and the overall advantages of dynamic IT over fixed IT is also examined.
- Analysis of SU interference on PU network and subsequent performance analysis is provided.
- Extensive measurement study and statistical modelling of radio characteristics in a UAV2W system in an indoor warehouse environment is presented in detail. These channel characteristics and modeling have the biggest application the health care domain, and in generic UAV-assisted wireless communication systems at UWB frequencies.
- Measurement study and modelling of mmWave channel characteristics in UAVs by emulating real life UAV motion by using a robotic arm is detailed. This is one of the novel studies that does not rely on simulation software, but emulates actual UAV motion by a robotic arm. The frequency under consideration is 28 GHz and the environment under consideration is an anechoic chamber. Channel characteristics such as Doppler spread and path-loss are investigated in this emulation based empirical study.
- Propeller modulation is studied in detail with two real UAVs that have mmWave horn antennas attached to them. One of the two UAVs acts as Tx, while the other behaves as a Rx. Different scenarios with different heights, and with different permutations of propeller-on and -off are considered in this thesis.

1.8 Organization

The thesis is organized as follows, Chapter II discusses the details on the study of dynamic IT in cognitve radio systems. Chapter III details the measurement study and statistical modelling of radio characteristics in UAV2W system in an indoor environment at UWB frequency, while Chapter IV examines the mmWave channel characteristics (Doppler and path-loss) by conducting a measurement study in an anechoic chamber with the actual UAV Motion performed by a robotic arm. The propeller modulation effect with real UAV is also investigated in this Chapter IV. Finally, the conclusions are drawn and future work is described in Chapter V.

CHAPTER II

INTERFERENCE TEMPERATURE IN COGNITIVE RADIO NETWORK

2.1 Introduction

In this chapter, we will look into the optimization of the available radio spectrum problem in a cognitive radio network, and delve into the modeling of interference temperature that controls the way the licensed spectrum is accessed. In the later part of this chapter, we will analyze the effect of secondary user interference on the primary user network. In the last decade, measurement studies on the actual spectrum usage has highlighted that a large portion of the licensed spectrum that is auctioned by the FCC is less utilized than the unlicensed ones. These studies also reflect the inefficient and inflexible spectrum usage that is leading to the spectrum scarcity for the end users [50–52]. This spectrum scarcity as mentioned in Chapter 1 is because of the rapid proliferation of new end users, devices and the high data demands from the users. To overcome this challenge of crowded spectrum, cognitive radio theory was introduced, where radios that are using unlicensed spectrum can exploit the available licensed spectrum opportunistically, and thereby utilise the spectrum optimally [1–3, 53, 54]. This type of optimal access leads to a better network performance in terms of overall capacity and in less outage probability.

In cognitive radio network (CRN), the users of the radio spectrum are divided into two categories- licensed and unlicensed users. Depending on the network configuration, the unlicensed users, also known as secondary users (SUs) are allowed to access the spectrum of the licensed users or the primary users (PUs) either when it is not in use by a PU or concurrently with PU transmissions, if and only if the SU does not degrade the quality of service (QoS) of PU transmission. To maintain this QoS, there is a certain interference power threshold that PU-Rx can tolerate and this threshold is known as interference temperature (IT) [8, 55–57]. The spectrum sharing network with concurrent access of the available spectrum is known as underlay cognitive network, while the network that allows spectrum access only during idle time is known as an overlay cognitive network [3, 4]. The network configuration under consideration in this chapter is the underlay network configuration.

In the underlay network configuration, the SUs adapt their peak or average transmit power [8–11] to maintain the IT threshold. In [58], Kang *et al.* have studied and derived the optimal power strategies for SU to maximize outage and ergodic capacity under both (peak and average power) constraints. Similarly, in [59], Srinivasa *et al.* considered peak and average power adaptation to maximize the SU signal to noise ratio (SNR) and capacity. However, peak power adaptation protects and guarantees instantaneous interference prevention at PU, and in many cases, the PU QoS would be limited by the instantaneous signal to interference plus noise ratio (SINR) at the receiver. Therefore, peak power adaptation

is considered in this chapter, however, it is important to note that the insights from peak power adaptation will still be valid even if average power adaptation is considered.

This type of power adaptation scheme requires the knowledge of channel state information (CSI) at SU-Tx, so that the SU can adapt its transmit power accordingly. Recent research studies have shown that this can be achieved either by utilizing feedback channels with acknowledgment/non-acknowledgement (ACK/ NACK) packet information or by detecting the transition of modulation and coding schemes (MCS) [60–64]. In our considered network, this job is accomplished by a central entity known as CBS (central base station), which periodically senses the CSI information of PUs and SUs in a CRN. This type of CRN with CBS is also known as a centralized CRN system [60, 63, 64]. Apart from sensing CSI, CBS also senses the primary network activity, and controls the SUs via dedicated sensing and control channels. However, in reality, the CSI knowledge is not perfect [65], but since one of the main aims of this chapter is to statistically highlight the advantages of dynamic IT over fixed IT, perfect CSI knowledge at SU-Tx can be safely assumed.

In short, statistical analysis of dynamic IT in CRN, and its performance compared to static IT and the case of SU interference on PU will be examined in detail in this chapter. With the dynamic IT settings, the IT for SU can be relaxed during the less traffic time or ideal time in the PU network, which in turn will allow the SU to opportunistically increase its transmit power, and thereby improve the overall network performance of the CRN. The system model for this case is discussed in the next section.

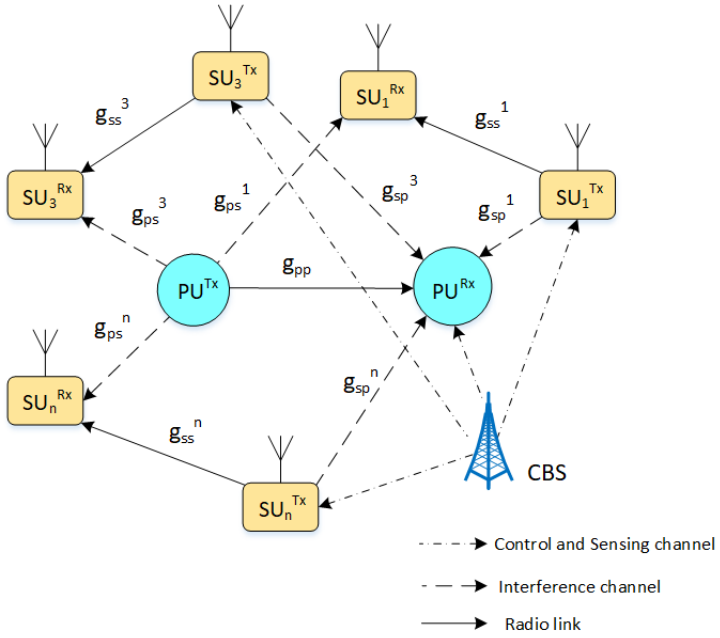

Figure 8: System model with N-SUs and a PU link.

2.2 System Model

In this section, the system under consideration is discussed in detail. The system model is shown in Fig. 8, which consists of a PU network and N-SUs in an underlay network config-

uration in which the available primary user spectrum is shared with N-SUs. Furthermore, it is assumed that the orthogonal frequency division multiple access (OFDMA) method is employed in the CRN that allows every PU to access orthogonal spectrum bands from the available bandwidth, and for each allocated PU orthogonal frequency band, the SUs will operate in separate sub-bands of it. This will result in no interference among SUs, but will cumulatively cause interference at the PU-Rx, whose spectrum is shared by these SUs. The various channel gains assuming point-to-point flat Rayleigh fading channels are given as, $g^1_{sp} = ||h^1_{sp}||^2$, $g^1_{ps} = ||h^1_{ps}||^2$, $g^1_{ss} = ||h^1_{ss}||^2$, and $g^1_{pp} = ||h^1_{pp}||^2$, where g represents the channel power gain, h represents the channel transfer function or channel response (Rayleigh), and subscript p represents PU while subscript s represents SU. Also, the superscripts $1, \ldots, n$ present the SU or PU index number, for example g^1_{ss} is the channel between the SU^{Tx}_1 and SU^{Rx}_1. Rayleigh fading model is the commonly used channel model in these types of theoretical studies. Other small-scale channel fading models such as Nakagami and Rician could be definitely considered, however, the insights and observations obtained from this study would remain the same. Moreover, we denote the exponentially distributed probability density functions (PDFs) of these random variables as $f_{g_{sp}}(x)$, $f_{g_{ps}}(x)$, $f_{g_{ss}}(x)$ and $f_{g_{pp}}(x)$. These PDFs are governed by corresponding rate parameters, which depend on the mean of the exponential distribution as $E(g_{sp}) = 1/\lambda_{sp}$, $E(g_{ps}) = 1/\lambda_{ps}$, $E(g_{ss}) = 1/\lambda_{ss}$ and $E(g_{pp}) = 1/\lambda_{pp}$.

It is worth noting that the mean values of channel power parameters in small-scale fading models incorporate the effect of large-scale fading such as path-loss and shadowing under the assumption that there are immobile users, i.e., path-loss and shadowing will be constant [66, 67]. Consequently, a low mean parameter would imply a larger distance between a PU-Rx and a SU-Tx than a high mean value; the mean value here refers to the received signal mean power over a distance. As an example, from Fig. 8, since SU-1 is nearer to PU-Rx than SU-3, it will have a higher mean value ($E(g_{sp}{}^1)$) than the SU-3. Therefore, selection of these rate parameters will take care of the distance dependency in itself. Apart from that, it is also assumed that the channels are flat in our model. Since the main motivation is to show the network performance gain in utilizing dynamic IT over fixed IT, traffic scheduling and access control are not considered. Moreover, a CRN with a single PU with single SU is considered for the analysis, which can be further extrapolated to multiple SUs with a single PU case, or multiple PU case with different number of SUs.

As mentioned in the earlier section, the centralized CRN [60, 63, 64] has a CBS that controls the CRN operation by sensing the PU activity periodically via sensing channels, and sets the dynamic IT for SUs via control channels. It is also important to highlight here that the CSI knowledge cannot be obtained perfectly in a practical wireless network, but with this centralized CRN, the CBS is assumed to have near to perfect CSI by periodic updates. This may lead to extra overheads in the network but for functionality of a centralized CRN, a near to perfect CSI is assumed to be true. In addition, the thermal additive white Gaussian noise (AWGN) in the network is assumed to have circularly symmetric complex Gaussian distribution with zero mean and variance as σ^2, i.e., $\mathcal{CN}(0, \sigma^2)$. Finally, to improve the readability of this Chapter, the most frequently used symbols are described in Table 1. In the next section, we will look into the modeling part of IT from a network capacity perspective.

Table 1: Notations.

Symbol	Description
c	Capacity
γ_p	SINR at PU-Rx
γ_s	SINR at SU-Rx
α	Continuous random variable for PU-Rx SINR
α_k	Discrete random variable for PU-Rx SINR, where $k = 1, 2, \ldots, \infty$
ψ	Interference plus noise
λ_p	Poisson rate parameter
λ_{xx}	Channel rate parameter (exponential rate) with subscript x can be s or p implying SU or PU
σ^2	AWGN variance
P_{rx}	Received power at PU-Rx
p	Peak transmit power
x	Dummy variable

2.3 Interference Temperature Modeling from Capacity distribution

In this section, we will now derive the interference power threshold from the variable traffic demand distribution considering a CRN system as described in the previous section[1]. First of all, it is well known that the data traffic distribution or the variable capacity distribution is discrete in nature, and therefore has been modelled by different available discrete distributions [68–72]. However, among those discrete distributions, Poisson distribution is a very strong candidate as it has been widely used in telecommunication since the advent of computer networks, and with proper selection of parameters, it can be made to fit most network traffic models [73, 74]. Also, since the traffic capacity demand changes over time, and the occurrences of the traffic demand events are independent from each other, the applicability of Poisson distribution to a network traffic model is further strengthened. Moreover, in different scenarios and conditions, Poisson distribution has been shown to match, and model the traffic data in a network [69, 70, 75, 76].

Ideally, one can use any of the available continuous or discrete distributions, but considering the close applicability of discrete distributions and usage for capacity demand modeling, Poisson distribution is the best candidate to represent the PU capacity demand [68–72]. Besides that, the insights provided in this study by modelling capacity demand by any of the available distributions will remain the same. The traffic/capacity demand assuming Poisson distribution with rate parameter λ_p is given as,

$$P_c(x_k) = \frac{\lambda_p^{x_k}}{x_k!} e^{-\lambda_p}, \ \forall \ \lambda_p > 0, \ x_k \in \{0, 1, 2, 3, \ldots, \infty\}. \tag{2.3.1}$$

[1]Note that the interference power threshold and interference temperature (IT) are used interchangeably throughout this chapter.

In Poisson distribution, this λ_p is the mean of the distribution, which in our case represents the mean capacity value. This Poisson distributed capacity demand will be used to find the corresponding SINR distribution, and afterwards from that SINR distribution, IT distribution will be determined. These statistical random variable transformations are done in steps by applying the well known cumulative distribution function (CDF) method [77,78]. To begin with, the relationship between instantaneous capacity and SINR is given as,

$$c = \log(1 + \gamma_p), \ \forall \ \gamma_p \geq 0,$$

where γ_p represents the instantaneous SINR at PU-Rx[2]and c represents the instantaneous capacity in (nats/s)/Hz. Using transformation of random variables, the probability mass function (PMF) of SINR at PU-Rx is given as,

$$P(\gamma_p) = P(c)\big|_{\gamma_p = e^c - 1} = \left. \frac{e^{-\lambda_p} \lambda_p^{c_k}}{c_k!} \right|_{c = \log(1+\gamma_p)}. \tag{2.3.2}$$

This transformed discrete distribution can be easily changed to a continuous distribution with the aid of Dirac-delta function [79] as,

$$f_{\gamma_p}(x) = \sum_{x_k \in \mathbb{R}} \frac{e^{-\lambda_p} \lambda_p^{\log(x_k+1)}}{\log(x_k+1)!} \delta(x - x_k). \ \forall \ x \geq 0, \tag{2.3.3}$$

where $\delta(x)$ is a Dirac-delta function. This transformation from discrete to continuous random variable will save a lot of effort in computations that involve mixed random variable distributions (continuous and discrete distributions) to derive the network performance expressions. However, this simple discrete random transformation needs more careful inspection.

The SINR at the PU-Rx is given as the ratio of the received signal power from PU-Tx to the interference plus noise power, that is $\gamma_p = P_{PU}^{Rx}/\psi$, where ψ represents the interference plus noise power. Therefore, ψ can be written as,

$$\psi = \frac{g_{pp} p}{\gamma_p}, \forall \ \gamma_p = \{0, 1, 2, \ldots, \infty\} \in \mathbb{R}, \tag{2.3.4}$$

where p is the peak transmit power. The peak transmit power of SU and PU is assumed to be the same.For $\gamma_p = 0$ in (2.3.4), ψ would be undefined, which will lead to an undefined data distribution. Therefore, to overcome this challenge, we can either begin by truncating the PU capacity distribution from Poisson to zero-truncated Poisson distribution [80–82], or we can truncate the distribution of SINR (γ_p) itself, which will have the range of $\gamma_p = \{1, 2, \ldots, \infty\}$, that is $\gamma_p \in \mathbb{R}^+$. Fig. 9 shows a case of truncating capacity distribution from general Poisson distribution to a zero-truncated Poisson distribution. One can observe the increase in the probabilities of all the samples after truncation with the shape remaining unchanged, for example at $x_k = 2, \lambda_p = 2$, the probability is $P(x) = 0.2707$ and at the same parameters in zero-truncated Poisson distribution the probability is $P(x) = 0.313$. The increase in the probability is due to the shrinking of the sample space.

[2]SINR is usually denoted by γ, but in this chapter, γ_p and γ_s are used to easily distinguish between the SINR at PU-Rx and SINR at SU-Rx respectively.

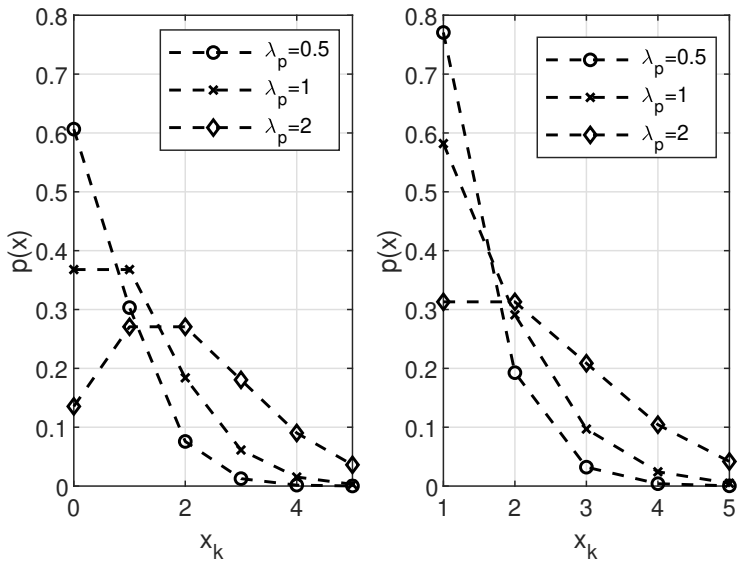

Figure 9: Comparison of normal Poisson distribution (left) with zero truncated Poisson distribution (right) for different rate parameter of $\lambda_p = 0.5, 1, 2$. Here the line plot is used for better visualization.

In this scenario, we will proceed with the SINR truncation method. Since, $f_{\gamma_p}(x) = 1$ for $x \geq 0$ and $f_{\gamma_p}(x) = 0$ for $x < 0$, thus, we can write $f_{\gamma_p}(x)$ for the case of $x \geq 0$ as,

$$\begin{aligned} f_{\gamma_p}(x)\big|_{x\geq 0} &= f_{\gamma_p}(x)\big|_{x=0} + f_{\gamma_p}(x)\big|_{x>0}, \\ f_{\gamma_p}(x)\big|_{x>0} &= 1 - e^{-\lambda_p x}. \end{aligned} \tag{2.3.5}$$

Therefore, the SINR distribution with support region of $\gamma_p \in \mathbb{R}^+$ after normalizing (2.3.3) by (2.3.5) will be,

$$f_{\gamma_p}(x) = \sum_{x_k \in \mathbb{R}^+} \frac{e^{-\lambda_p} \lambda_p^{\log(1+x_k)}}{(1 - e^{-\lambda_p}) \log(1 + x_k)!} \delta(x - x_k), \quad x > 0. \tag{2.3.6}$$

Fig. 10 compares the PDF and CDF generated from the above theoretical SINR expression with simulations results[3], and it can be observed that both simulations and theoretical results match very well. Once the SINR distribution at PU is known, the interference plus noise distribution is then found as,

$$\psi = \frac{g_{pp} p}{\gamma_p} = \left(\frac{g_{pp}}{\gamma_p}\right) p. \tag{2.3.7}$$

This expression is basically a ratio of two random variables.

On careful observation, the numerator of this equation has a random variable g_{pp}, which is exponentially distributed channel power, while the denominator γ_p is the SINR (random

[3]In simulations, the primarily utilized MATLAB functions are: "poissrnd" for generating random numbers from Poisson distribution, "ecdf" for empirical cumulative distribution function and "histogram" for generating probabilistic plots for the simulation data.

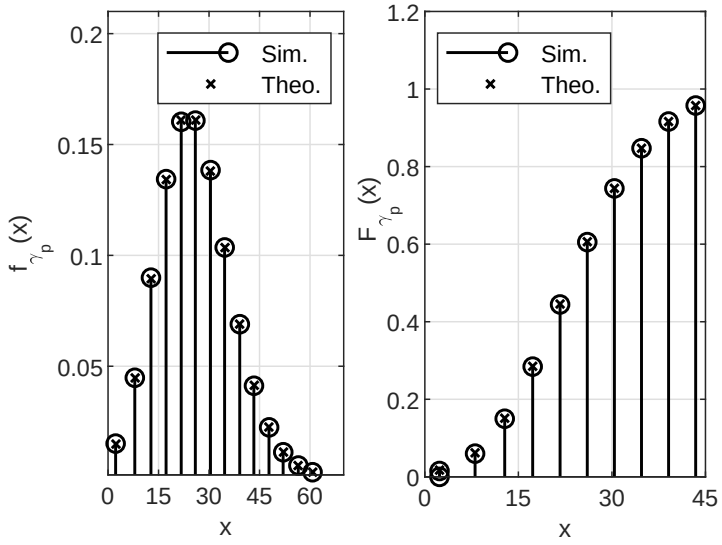

Figure 10: Simulation and theoretical PDF and CDF of SINR for $\lambda_p = 6$.

variable), whose distribution is derived in (2.3.6) using statistical transformations from Poisson distribution (capacity). The correlation between these two random variables is zero, hence, they are both independent. The only dependency between these random variables is ψ, which can be dynamically adjusted. In other words, the PU is allowed to transmit the data at maximum power p, so as to have high PU network capacity, while the SINR derived from the capacity is made dependent on the wireless channel conditions (g_{pp}) through IT (ψ). This in turn forces the SU to adapt its transmit power accordingly. Thus, setting a dynamic IT, will allow the CRN to change the transmit power of SU-Tx allowing it to increase during the relaxed IT threshold period.

Let $\frac{P_{PU}^{Rx}}{\gamma_p} = \frac{\beta}{\alpha}$, using the CDF method for ratio of two random variables [78, 79], the PDF is then given as,

$$f_\psi(x) = \int_0^\infty \alpha \cdot f_{P_{rx},\gamma_p}(x\alpha, \alpha) d\alpha, \tag{2.3.8}$$

Since, β and α are two independent random variables,

$$f_\psi(x) = \int_0^\infty \alpha \cdot f_{P_{rx}}(x\alpha)\ f_{\gamma_p}(\alpha)\ d\alpha, \forall\ \alpha > 0. \tag{2.3.9}$$

As the channel is assumed to be Rayleigh distributed, therefore, the channel power distribution will then be a scaled exponential distribution,

$$f_{P_{rx}}(x) = \frac{\lambda_{pp}}{p} e^{-\lambda_{pp} x/p}, \tag{2.3.10}$$

where λ_{pp} is the channel rate parameter between PU-Tx and PU-Rx, while p is the peak PU

transmit power. Substituting (2.3.10) and (2.3.6) in (2.3.9),

$$\begin{aligned} f_{\psi}(x) &= \int_0^{\infty} \alpha \left(\frac{\lambda_{pp}}{p} e^{-\lambda_{pp}\alpha x/p} \right) \left(\sum_{\alpha_k \in \mathbb{R}^+} \frac{e^{-\lambda_p}}{1-e^{-\lambda_p}} \frac{\lambda_p^{\log(1+\alpha_k)}}{\log(1+\alpha_k)!} \delta(\alpha - \alpha_k) \right) d\alpha, \\ f_{\psi}(x) &= \frac{\lambda_{pp}}{p} \sum_{\alpha_k \in \mathbb{R}^+} \frac{e^{-\lambda_p} \lambda_p^{\log(1+\alpha_k)}}{(1-e^{-\lambda_p}) \log(1+\alpha_k)!} \int_0^{\infty} \alpha e^{-\frac{\lambda_{pp}\alpha_k x}{p}} \delta(\alpha - \alpha_k) d\alpha. \end{aligned} \tag{2.3.11}$$

Using the property of delta function, $\int_{\alpha-\epsilon}^{\alpha+\epsilon} f(t)\delta(t-\alpha)dt = f(\alpha),\ \epsilon > 0$, the PDF expressions reduces to,

$$f_{\psi}(x) = \frac{\lambda_{pp}}{p} \sum_{\alpha_k \in \mathbb{R}^+} \frac{e^{-\lambda_p} \lambda_p^{\log(1+\alpha_k)}}{(1-e^{-\lambda_p}) \log(1+\alpha_k)!} \alpha_k e^{-\lambda_{pp}\alpha_k x/p}. \tag{2.3.12}$$

Now, the CDF of interference plus noise is found by integrating this PDF as,

$$\begin{aligned} F_{\psi}(x) &= \int_0^{x} \frac{\lambda_{pp}}{p} \sum_{\alpha_k \in \mathbb{R}^+} \frac{e^{-\lambda_p} \lambda_p^{\log(1+\alpha_k)} \alpha_k e^{-\lambda_{pp}\alpha_k x/p}}{(1-e^{-\lambda_p}) \log(1+\alpha_k)!} dx, \\ &= \frac{\lambda_{pp}}{p} \frac{e^{-\lambda_p}}{1-e^{-\lambda_p}} \sum_{\alpha_k \in \mathbb{R}^+} \frac{\lambda_p^{\log(1+\alpha_k)} \alpha_k}{\log(1+\alpha_k)!} \int_0^{x} e^{-\lambda_{pp}\alpha_k x/p} dx. \end{aligned} \tag{2.3.13}$$

On further evaluation, the final CDF expression comes out to be,

$$F_{\psi}(x) = \sum_{\alpha_k \in \mathbb{R}^+} \frac{e^{-\lambda_p} \lambda_p^{\log(1+\alpha_k)}}{(1-e^{-\lambda_p}) \log(1+\alpha_k)!} \left[1 - e^{-\lambda_{pp}\alpha_k x/p} \right]. \tag{2.3.14}$$

Fig. 11 shows the comparison between the simulation and theoretical results for the PDF derived in (2.3.12) at different values of λ_p. Since, the noise is assumed to be Gaussian distribution with zero mean and variance of σ^2, i.e., $\mathcal{CN}(0, \sigma^2)$, the interference plus noise can be considered as total interference threshold or IT with a constant noise variance σ^2 included in it. In simpler terms, ψ can be regarded as total interference threshold. The proof that (2.3.12) is a valid PDF is given in Appendix 5.3. So far the first step of deriving the dynamic distribution of IT for PU-Rx from the variable network traffic demand (Poisson distributed) has been found, the next step is to evaluate the SU network performance metrics by deriving, and analyzing outage probability and mean capacity distributions, which will be the topic in the next section.

2.4 Outage Probability and Mean Capacity in General Region

In this section, we will derive the outage probability and mean capacity of SU assuming peak power adaptation at SU-Tx. The SU transmit power with peak power adaptation [11] is given as,

$$P_{SU}^{Tx} = \min \left(\frac{\psi}{g_{sp}}, p \right), \tag{2.4.1}$$

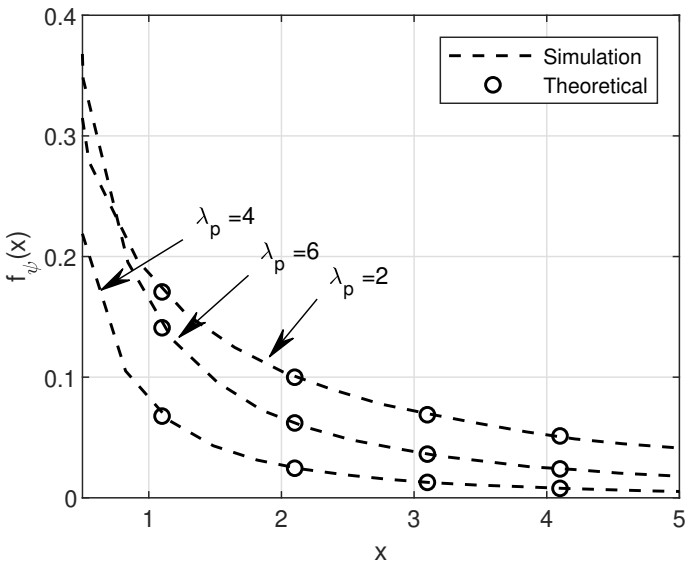

Figure 11: Simulation and theoretical PDF of interference plus noise for different values of $\lambda_p = 2, 4, 6$.

where p is the peak transmit power, g_{sp} is the channel between SU-Tx to PU-Rx and ψ is the total IT. To make the mathematical notation's simpler, we will use P_{tx} and P_{rx} for transmit and receiver power at SU, rather than P_{SU}^{Tx} and P_{SU}^{Rx}. Therefore, the SINR at SU-Rx is,

$$\gamma_s = \frac{P_{tx} g_{ss}}{p g_{ps} + \sigma^2} = \frac{P_{rx}}{p g_{ps} + \sigma^2}, \tag{2.4.2}$$

where g_{ss} is the channel power gain between SU-Tx and SU-Rx, while g_{ps} is the channel power gain between PU-Tx and SU-Rx, and p is the peak power at PU. Thus, the mean capacity expression for SU will be,

$$\bar{C} = B \int_0^\infty \log(1+x)\ f_{\gamma_s}(x) dx, \tag{2.4.3}$$

where $f_{\gamma_s}(x)$ is the PDF of SINR at SU-Rx, and B is the bandwidth. Using integration by parts [8, 83], the expression can be written as,

$$\bar{C} = \int_0^\infty \frac{1 - F_{\gamma_s}(x)}{1+x} dx, \tag{2.4.4}$$

where B is assumed to be 1 Hz and $F_{\gamma_s}(x)$ is the CDF of SINR or the outage probability. Therefore, to evaluate the mean capacity, we need to find the outage probability at SU. Following the same step-by-step statistical transformation approach as before, we will first derive γ_s from P_{tx}, and then derive the outage probability F_{γ_s} and finally the capacity C.

To find P_{tx} as given in (2.4.1), let $t = \frac{\psi}{g_{sp}} = \frac{u}{v}$. Then, the CDF of t will be given as,

$$F_T(x) = \Pr\left(\frac{u}{v} < x\right) = \Pr\left(u < vx,\ v > 0\right) = \int_0^\infty \int_0^{vx} f_{\psi, g_{sp}}(uv) du\ dv. \tag{2.4.5}$$

Since, ψ and g_{sp} are independent random variables, therefore,

$$F_T(x) = \int_0^\infty \int_0^{vx} f_\psi(u)du f_{g_{sp}}(v)dv = \int_0^\infty F_\psi(vx) f_{g_{sp}}(v)dv. \tag{2.4.6}$$

where $f_{g_{sp}}(v)$ is the PDF of the exponential channel power gain, and $F_\psi(x)$ is given in (2.3.14). On substituting these terms in the above equation,

$$\begin{aligned} F_T(x) &= \int_0^\infty \sum_{\alpha_k \in \mathbb{R}^+} \frac{e^{-\lambda_p} \lambda_p^{\log(1+\alpha_k)} \left[1 - e^{\frac{-\lambda_{pp}\alpha_k vx}{p}}\right]}{(1 - e^{-\lambda_p}) \log(1+\alpha_k)!} \lambda_{sp} e^{-\lambda_{sp} v} dv, \\ F_T(x) &= \frac{\lambda_{sp} e^{-\lambda_p}}{1 - e^{-\lambda_p}} \sum_{\alpha_k \in \mathbb{R}^+} \frac{\lambda_p^{\log(1+\alpha_k)}}{\log(1+\alpha_k)!} \left[\int_0^\infty e^{-\lambda_{sp} v} dv - \int_0^\infty e^{-\left(\frac{\lambda_{pp}\alpha_k x}{p} + \lambda_{sp}\right) v} dv \right]. \end{aligned} \tag{2.4.7}$$

On further evaluation, this expression finally reduces to,

$$F_T(x) = \frac{e^{-\lambda_p}}{1 - e^{-\lambda_p}} \sum_{\alpha_k \in \mathbb{R}^+} \frac{\lambda_p^{\log(1+\alpha_k)}}{\log(1+\alpha_k)!} \left(\frac{\eta \alpha_k x}{\eta \alpha_k x + p} \right), \tag{2.4.8}$$

where $\eta = \frac{\lambda_{pp}}{\lambda_{sp}}$. The PDF of $t = \frac{\psi}{g_{sp}}$ from its CDF will be,

$$f_T(x) = \frac{e^{-\lambda_p}}{1 - e^{-\lambda_p}} \sum_{\alpha_k \in \mathbb{R}^+} \frac{\lambda^{\log(1+\alpha_k)}}{\log(1+\alpha_k)!} \left[\frac{\eta \alpha_k p}{(\eta \alpha_k x + p)^2} \right]. \tag{2.4.9}$$

Thus, the distribution of P_{tx} as a minimum function of the constant p and random variable t is as follows,

$$\begin{aligned} P_{tx} &= \min\left(\frac{\psi}{g_{sp}}, p\right) = \min\,(t, p), \\ F_{P_{tx}}(x) &= F_T(x) + F_p(x) - F_T(x)F_p(x) = F_T(x)\,[1 - H(x-p)] + H(x-p), \end{aligned}$$

where the constant p is expressed as a random variable with CDF as a Heaviside function $H(x-p)$, and PDF as a Dirac delta function $\delta(x-p)$ [8, 79, 84]. Correspondingly, the PDF would be given as,

$$f_{P_{tx}}(x) = f_T(x)[1 - H(x-p)] + \delta(x-p) - F_T(x)\delta(x-p), \tag{2.4.10}$$

where $F_T(x)$ and $f_T(x)$ are given in (2.4.8) and (2.4.9).

From this given P_{tx} distribution, the next step is to determine the received power at SU-Rx, that is, $P_{rx} = P_{tx} g_{ss}$. This expression is a product of two random variables, one of which is exponential random variable g_{ss}, and the other one is P_{tx}. Let $P_{rx} = P_{tx} g_{ss}$ be

written as $P_{rx} = v_1 v_2$ where $v_1 = g_{ss}$ and $v_2 = P_{tx}$. Therefore,

$$\begin{aligned} F_{P_{rx}}(x) &= \Pr(v_1 v_2 \leq x) = \int_0^\infty \int_0^{\frac{x}{v_2}} f_{g_{ss}}\left(v_1 \leq \frac{x}{v_2}\right) f_{P_{tx}}(v_2) dv_2, \\ &= \int_0^\infty F_{g_{ss}}(x/v_2) f_{P_{tx}}(v_2) dv_2, \\ &= \int_0^\infty \left[1 - e^{-\lambda_{ss} x/v_2}\right] f_{P_{tx}}(v_2) dv_2, \\ &= 1 - \int_0^\infty e^{-\lambda_{ss} x/v_2} \; f_{P_{tx}}(v_2) dv_2. \end{aligned} \tag{2.4.11}$$

On substituting (2.4.8), (2.4.9) and (2.4.10) in (2.4.11),

$$\begin{aligned} F_{P_{rx}}(x) &= 1 - \int_0^\infty e^{-\lambda_{ss} x/v_2} \big[f_t(v_2)[1 - H(v_2 - p)] + \delta(v_2 - p) - F_t(v_2)\delta(v_2 - p) \big] dv_2, \\ &= 1 - \int_0^\infty \frac{e^{-\lambda_{ss} x/v_2} e^{-\lambda_p}}{(1 - e^{-\lambda_p})} \sum_{\alpha_k \in \mathbb{R}^+} \frac{\lambda_p^{\log(1+\alpha_k)}}{\log(1+\alpha_k)!} \left[\frac{\eta \alpha_k p}{(\eta \alpha_k v_2 + p)^2} \right] dv_2 \\ &+ \int_p^\infty \frac{e^{-\frac{\lambda_{ss} x}{v_2}} e^{-\lambda_p}}{(1 - e^{-\lambda_p})} \sum_{\alpha_k \in \mathbb{R}^+} \frac{\lambda_p^{\log(1+\alpha_k)}}{\log(1+\alpha_k)!} \left[\frac{\eta \alpha_k p}{(\eta \alpha_k v_2 + p)^2} \right] dv_2 - e^{-\frac{\lambda_{ss} x}{p}} \\ &+ \int_0^\infty e^{-\lambda_{ss} x/v_2} F_{P_{tx}}(v_2) \delta(v_2 - p) dv_2, \end{aligned} \tag{2.4.12}$$

which finally reduces down to,

$$\begin{aligned} F_{P_{rx}}(x) = 1 - e^{-\lambda_{ss} x/p} &+ \frac{e^{-\lambda_p}}{1 - e^{-\lambda_p}} \sum_{\alpha_k \in \mathbb{R}^+} \frac{\lambda^{\log(1+\alpha_k)}}{\log(1+\alpha_k)!} \frac{\eta \alpha_k \lambda_{ss} x}{p} \\ &\times e^{\frac{\eta \alpha_k \lambda_{ss} x}{p}} \Gamma\left(0, \frac{\lambda_{ss}(\eta \alpha_k + 1) x}{p}\right), \end{aligned} \tag{2.4.13}$$

where $\Gamma(a, x)$ is an incomplete Gamma function [85] that is defined as,

$$\Gamma(a, x) = \int_a^\infty t^{a-1} e^{-t} dt, \; \forall \; a > 0, \; x \geq 0.$$

Finally, from this distribution of P_{rx}, the distribution of SINR at SU-Rx will be the ratio of two independent random variables P_{rx} and $pg_{ps} + \sigma^2$, which can be easily found out by using the same CDF method. That is,

$$\gamma_s = \frac{P_{rx}}{pg_{ps} + \sigma^2}. \tag{2.4.14}$$

Let $\frac{P_{rx}}{pg_{ps} + \sigma^2} = \frac{u}{v}$, therefore,

$$
\begin{aligned}
F_{\gamma_s}(x) = \Pr\left(\frac{u}{v} \leq x\right) &= \int_{\sigma^2}^{\infty} \int_{0}^{vx} f_{P_{rx}}(u \leq vx) f_v(v)\ du\ dv, \\
&= \int_{\sigma^2}^{\infty} \left(\int_{0}^{vx} f_{P_{rx}}(u \leq vx)\ du \right) f_v(v) dv, \\
&= \int_{\sigma^2}^{\infty} F_{P_{rx}}(vx)\ f_v(v) dv.
\end{aligned} \tag{2.4.15}
$$

Since, $v = pg_{ps} + \sigma^2$ is a scaled and shifted exponential distribution, while $F_{P_{rx}}(vx)$ was found in (2.4.13). Therefore,

$$
\begin{aligned}
F_{\gamma_s}(x) = \int_{\sigma^2}^{\infty} \Bigg[1 - e^{-\frac{\lambda_{ss} x}{p}} + \frac{e^{-\lambda_p}}{1 - e^{-\lambda_p}} \sum_{\alpha_k \in \mathbb{R}^+} \frac{\lambda_p^{\log(1+\alpha_k)}}{\log(1+\alpha_k)!} \frac{\eta \alpha_k \lambda_{ss} vx}{p} e^{\frac{\eta \alpha_k \lambda_{ss} vx}{p}} \\
\times \Gamma\left(0, \frac{\lambda_{ss}(\eta \alpha_k + 1) vx}{p}\right) \Bigg] \frac{\lambda_{ps}}{p} e^{-\frac{\lambda_{ps}}{p}(v - \sigma^2)} dv, \\
= \int_{\sigma^2}^{\infty} \frac{\lambda_{ps}}{p} e^{-\frac{\lambda_{ps}}{p}(v-\sigma^2)} dv - \int_{\sigma^2}^{\infty} \frac{\lambda_{ps}}{p} e^{-\frac{\lambda_{ss} x}{p}} \times e^{-\frac{\lambda_{ps}}{p}(v-\sigma^2)} dv + \int_{\sigma^2}^{\infty} \frac{e^{-\lambda_p}}{1 - e^{-\lambda_p}} \\
\times \sum_{\alpha_k \in \mathbb{R}^+} \frac{\lambda_p^{\log(1+\alpha_k)}}{\log(1+\alpha_k)!} \frac{\eta \alpha_k \lambda_{ss} vx}{p} e^{\frac{\eta \alpha_k \lambda_{ss} vx}{p}} \Gamma\left(0, \frac{\lambda_{ss}(\eta \alpha_k + 1) vx}{p}\right) \frac{\lambda_{ps}}{p} e^{-\frac{\lambda_{ps}}{p}(v-\sigma^2)} dv,
\end{aligned} \tag{2.4.16}
$$

which can be expressed as,

$$
F_{\gamma_s}(z) = I_1 - I_2 - I_3. \tag{2.4.17}
$$

Evaluating these integrals individually,

$$
I_1 = \int_{\sigma^2}^{\infty} \frac{\lambda_{ps}}{p} e^{-\frac{\lambda_{ps}}{p}(v-\sigma^2)} dv = 1. \tag{2.4.18}
$$

Here I_1 is the PDF that is integrated over its full range resulting in the value being 1. I_2 on the other hand is evaluated as,

$$
I_2 = \int_{\sigma^2}^{\infty} e^{-\lambda_{ss} x/p} \frac{\lambda_{ps}}{p} e^{-\frac{\lambda_{ps}}{p}(v-\sigma^2)} dv = \frac{\lambda_{ps} e^{\lambda_{ps} \sigma^2}}{p} \int_{\sigma^2}^{\infty} e^{-\frac{\lambda_{ss} x + \lambda_{ps}}{p} v} dv, \tag{2.4.19}
$$

which on further evaluation yields,

$$
I_2 = \frac{\lambda_{ps}}{\lambda_{ps} + \lambda_{ss} x} e^{-\frac{\lambda_{ss} \sigma^2 x}{p}}. \tag{2.4.20}
$$

Lastly, evaluating I_3,

$$
\begin{aligned}
I_3 = \frac{e^{-\lambda_p} \lambda_{ps}}{(e^{-\lambda_p} - 1) p} e^{\frac{\lambda_{ps}}{p} \sigma^2} \sum_{\alpha_k \in \mathbb{R}^+} \frac{\lambda_p^{\log(1+\alpha_k)}}{\log(1+\alpha_k)!} \frac{\eta \alpha_k \lambda_{ss} x}{p} \int_{\sigma^2}^{\infty} v e^{\frac{\eta \alpha_k \lambda_{ss} vx}{p}} e^{-\frac{\lambda_{ps}}{p} v} \\
\times \Gamma\left(0, \frac{\lambda_{ss}(\eta \alpha_k + 1) vx}{p}\right) dv,
\end{aligned} \tag{2.4.21}
$$

Which on further evaluation yields,

$$I_3 = \sum_{\alpha_k \in \mathbb{R}^+} \frac{\eta \lambda_{ps} \lambda_{ss} \alpha_k x e^{-\lambda_p} (e^{-\lambda_p} - 1)^{-1}}{(\lambda_{ps} - \eta \alpha_k \lambda_{ss} x)^2 (\lambda_{ps} + \lambda_{ss} x)} \frac{\lambda_p^{\log(1+\alpha_k)}}{\log(1+\alpha_k)!} \Bigg[(\lambda_{ps} - \eta \alpha_k \lambda_{ss} x) e^{-\lambda_{ss} \sigma^2 x / p} \times (\lambda_{ps} + \lambda_{ss} x) \Bigg\{ e^{\eta \alpha_k \lambda_{ss} \sigma^2 x / p} \left(1 + \frac{(\lambda_{ps} - \eta \alpha_k \lambda_{ss}) \sigma^2}{p} \right) \Gamma \left(0, \frac{(\eta \alpha_k + 1) \lambda_{ss} \sigma^2 x}{p} \right) - e^{\lambda_{ps} \sigma^2 / p} \Gamma \left(0, \frac{(\lambda_{ps} + \lambda_{ss} x) \sigma^2}{p} \right) \Bigg\} \Bigg]. \tag{2.4.22}$$

Therefore, on substituting I_1, I_2 and I_3, $F_{\gamma_s}(x)$ or the outage probability will be given as in (2.4.24), and the proof that it is valid distribution is given in Appendix 5.3. Furthermore, substituting (2.4.24) in the mean capacity expression that is given as,

$$\bar{C} = \int_0^\infty \frac{1 - F_{\gamma_s}(x)}{1 + x} dx. \tag{2.4.23}$$

will result in (2.4.25).

$$F_{\gamma_s}(x) = 1 - \frac{\lambda_{ps} e^{-\frac{\lambda_{ss} \sigma^2 x}{p}}}{\lambda_{ps} + \lambda_{ss} x} + \sum_{\alpha_k \in \mathbb{R}^+} \frac{\eta \lambda_{ps} \lambda_{ss} \alpha_k x e^{-\lambda_p} (1 - e^{-\lambda_p})^{-1}}{(\lambda_{ps} - \eta \alpha_k \lambda_{ss} x)^2 (\lambda_{ps} + \lambda_{ss} x)} \frac{\lambda_p^{\log(1+\alpha_k)}}{\log(1+\alpha_k)!} \cdot \Bigg[(\lambda_{ps} - \eta \alpha_k \lambda_{ss} x) e^{-\lambda_{ss} \sigma^2 x / p} + (\lambda_{ps} + \lambda_{ss} x) \Bigg\{ e^{\frac{x \eta \alpha_k \lambda_{ss} \sigma^2}{p}} \left(1 + \frac{(\lambda_{ps} - \eta \alpha_k \lambda_{ss}) \sigma^2}{p} \right) \times \Gamma \left(0, \frac{(\eta \alpha_k + 1) \lambda_{ss} \sigma^2 x}{p} \right) - e^{\lambda_{ps} \sigma^2 / p} \Gamma \left(0, \frac{(\lambda_{ps} + \lambda_{ss} x) \sigma^2}{p} \right) \Bigg\} \Bigg] \tag{2.4.24}$$

Unfortunately, there is no closed form solution for the second integral (I_4) of (2.4.25), which therefore needs to be evaluated numerically. Thus far, we have derived the outage probability and mean capacity of a SU in a CRN network irrespective of their operable region. However, there can be a case where the peak power p is very high, so that during the peak power adaptation at SU-Tx, the final transmit power (P_{SU}^{Tx}) will always be $\frac{\psi}{g_{sp}}$. This region is also known as high power region [11], and it will be analyzed in the next section for deeper insights.

2.5 Outage Probability and Mean Capacity in High Power Region

In high power region, $p >> \frac{\psi}{g_{sp}}$ at SU-Tx, therefore, SU transmit power assuming peak power adaptation will then be given as,

$$\bar{C} = \int_0^\infty \frac{\lambda_{ps} e^{-\frac{\lambda_{ss}\sigma^2 x}{p}}}{(\lambda_{ps}+\lambda_{ss}x)(1+x)}dx - \int_0^\infty \sum_{\alpha_k \in \mathbb{R}^+} \Bigg(\frac{\eta\lambda_{ps}\lambda_{ss}\alpha_k x e^{-\lambda_p}(1+x)^{-1}}{(\lambda_{ps}-\eta\alpha_k\lambda_{ss}x)^2(\lambda_{ps}+\lambda_{ss}x)}$$
$$\times \frac{\lambda_p^{\log(1+\alpha_k)}}{(1-e^{-\lambda_p})\log(1+\alpha_k)!}\Bigg[(\lambda_{ps}-\eta\alpha_k\lambda_{ss}x)e^{-\lambda_{ss}\sigma^2 x/p}dx + (\lambda_{ps}+\lambda_{ss}x)$$
$$\times \Bigg\{ e^{\eta\alpha_k\lambda_{ss}\sigma^2 x/p}\Bigg(1+\frac{(\lambda_{ps}-\eta\alpha_k\lambda_{ss})\sigma^2}{p}\Bigg)\Gamma\Bigg(0,\frac{(\eta\alpha_k+1)\lambda_{ss}\sigma^2 x}{p}\Bigg) \tag{2.4.25}$$
$$- e^{\lambda_{ps}\sigma^2/p}\Gamma\Bigg(0,\frac{(\lambda_{ps}+\lambda_{ss}x)\sigma^2}{p}\Bigg)\Bigg\}\Bigg]\Bigg)dx$$
$$\bar{C} = \quad \frac{\lambda_{ps}}{\lambda_{ss}-\lambda_{ps}}\Bigg[e^{\lambda_{ps}\sigma^2/p}\Gamma\Bigg(0,\frac{\lambda_{ps}\sigma^2}{p}\Bigg) - e^{\lambda_{ss}\sigma^2/p}\Gamma\Bigg(0,\frac{\lambda_{ss}\sigma^2}{p}\Bigg)\Bigg] + I_4$$

$$P_{SU}^{Tx} = \min\left(\frac{\psi}{g_{sp}}, p\right) = \frac{\psi}{g_{sp}} = t, \tag{2.5.1}$$

which reduces the probability distribution of P_{tx} to $t(x)$ as given in (2.4.10). Therefore, the CDF of P_{rx} as $t = \frac{u}{v}$ is as follows,

$$\begin{aligned} F_{P_{rx}}(x) &= \int_0^\infty F_{g_{ss}}(x/v) f_{P_{tx}}(v)dv, \\ &= \int_0^\infty [1-e^{-\frac{\lambda_{ss}x}{v}}]\ \frac{e^{-\lambda_p}}{1-e^{-\lambda_p}} \sum_{\alpha_k\in\mathbb{R}^+} \frac{\lambda_p^{\log(1+\alpha_k)}}{\log(1+\alpha_k)!}\Bigg[\frac{\eta\alpha_k p}{(\eta\alpha_k x+p)^2}\Bigg]dv, \end{aligned} \tag{2.5.2}$$

which simplifies down to

$$F_{P_{rx}}(x) = 1 - \frac{e^{-\lambda_p}}{1-e^{-\lambda_p}} \sum_{\alpha_k\in\mathbb{R}^+} \frac{\lambda_p^{\log(1+\alpha_k)}}{\log(1+\alpha_k)!}\Bigg[1-\frac{\eta\alpha_k\lambda_{ss}}{p}xe^{\lambda_{ss}\eta\alpha_k x/p}\cdot\Gamma\Bigg(0,\frac{\lambda_{ss}\eta\alpha_k x}{p}\Bigg)\Bigg]. \tag{2.5.3}$$

Thus, the outage probability will be,

$$\begin{aligned} F_{\gamma_s}(x) &= \int_{\sigma^2}^\infty F_{P_{rx}}(vx) f_v(v)dv, \\ &= \int_{\sigma^2}^\infty \Bigg[1 - \frac{e^{-\lambda_p}}{1-e^{-\lambda_p}} \sum_{\alpha_k\in\mathbb{R}^+} \frac{\lambda_p^{\log(1+\alpha_k)}}{\log(1+\alpha_k)!}\Bigg(1-\frac{\eta\alpha_k\lambda_{ss}vx}{p}e^{\lambda_{ss}\eta\alpha_k vx/p} \\ &\qquad \times\Gamma\Bigg(0,\frac{\lambda_{ss}\eta\alpha_k xv}{p}\Bigg)\Bigg)\Bigg]\frac{\lambda_{ps}}{p}e^{-\frac{\lambda_{ps}}{p}(v-\sigma^2)}dv, \end{aligned} \tag{2.5.4}$$

$$F_{\gamma_s}(x) = 1 - \frac{e^{-\lambda_p}}{1-e^{-\lambda_p}} \sum_{\alpha_k \in \mathbb{R}^+} \frac{\lambda_p^{\log(1+\alpha_k)}}{\log(1+\alpha_k)!} - \frac{e^{-\lambda_p}}{1-e^{-\lambda_p}} \sum_{\alpha_k \in \mathbb{R}^+} \frac{\lambda_p^{\log(1+\alpha_k)} \eta \alpha_k \lambda_{ss} x}{\log(1+\alpha_k)!} \times \frac{1}{(\lambda_{ps} - \eta\alpha_k\lambda_{ss}x)^2} \left[\lambda_{ps} - \eta\alpha_k\lambda_{ss}x + \lambda_{ps} e^{\lambda_{ps}\sigma^2/p} \Gamma\left(0, \frac{\lambda_{ps}\sigma^2}{p}\right) \right], \tag{2.5.5}$$

which on further evaluation reduces to,

$$F_{\gamma_s}(x) = \sum_{\alpha_k \in \mathbb{R}^+} \frac{\lambda_p^{\log(1+\alpha_k)} \eta \alpha_k \lambda_{ss} x}{\log(1+\alpha_k)!} \frac{1}{(\lambda_{ps} - \eta\alpha_k\lambda_{ss}x)^2} \left[\lambda_{ps} - \eta\alpha_k\lambda_{ss}x - \lambda_{ps} e^{\lambda_{ps}\sigma^2/p} \times \Gamma\left(0, \frac{\lambda_{ps}\sigma^2}{p}\right) + \lambda_{ps} e^{\eta\alpha_k\lambda_{ss}x\sigma^2/p} \left(1 + \frac{(\lambda_{ps} - \eta\alpha_k\lambda_{ss}x)\sigma^2}{p}\right) \Gamma\left(0, \frac{\eta\alpha_k\lambda_{ss}x\sigma^2}{p}\right) \right]. \tag{2.5.6}$$

Finally, to determine the mean capacity, we will substitute (2.5.6) in (2.4.23). Unfortunately, this expression also does not have a closed form solution and has to be evaluated numerically. In the next section, we will validate and discuss all these derived expressions with simulation results in detail.

2.6 Results and Discussion

In this section, we will compare the analytical expression derived in the previous sections by comparing them with Monte Carlo Simulations in MATLAB®, and numerical evaluations in MATHEMATICA®. Furthermore, instantaneous and mean capacity, and outage probability of a dynamic IT based CRN, are compared with a fixed IT based CRN to show the advantages of setting a dynamic IT over fixed IT. The different distance dependent rate parameters used in the simulation were selected for illustrative purposes, but depending upon different scenarios (environment and distance), different values can be used. Nevertheless, the selection of parameters is inconsequential to the insights provided by choosing any set of rate parameters. For Rayleigh fading channels, the mean values were selected as $E(g_{sp}) = 1/\lambda_{sp} = 2$, $E(g_{ps}) = 1/\lambda_{ps} = 3.3$, $E(g_{ss}) = 1/\lambda_{ss} = 5$ and $E(g_{pp}) = 1/\lambda_{pp} = 4$, while the peak power was chosen depending on the analysis and case in hand. Also, the noise power was set to be $\sigma^2 = 1$. These different parameters are also summarized in Table 2.

First, we start with the simulation of the outage probability expression given in expression (2.4.24). In this case, the capacity demand (Poisson distribution) at PU is fixed at $\lambda_p = 2$, while peak power is kept at -10, 0 and $+10$ dB. Fig. 12 shows the result of comparison between the simulation and theoretical expression that are in very close agreement with each other. Intuitively, high transmit power will better accommodate the capacity/data traffic demand than the low transmit power, which is reflected in the outage probability plot of Fig. 12 with less outage values. As an example, one can observe that at every SINR value in Fig. 12, the outage probability is higher for low peak power value as compared to higher peak power value. Next, we fix the peak transmit power at 10 dB and analyze the effect of changing capacity/data traffic demand of PU on outage probability. The changing capacity demand is reflected in the Poisson rate parameter and the values selected in this scenario

Table 2: Different simulation parameters.

Parameter	Value
$E[g_{sp}]$	2
$E[g_{ps}]$	3.3
$E[g_{ss}]$	5
$E[g_{pp}]$	4
σ^2	1
p	-10,0,10 dB (depending on the given case)
λ_p	1,2...,6 (depending on the given case)

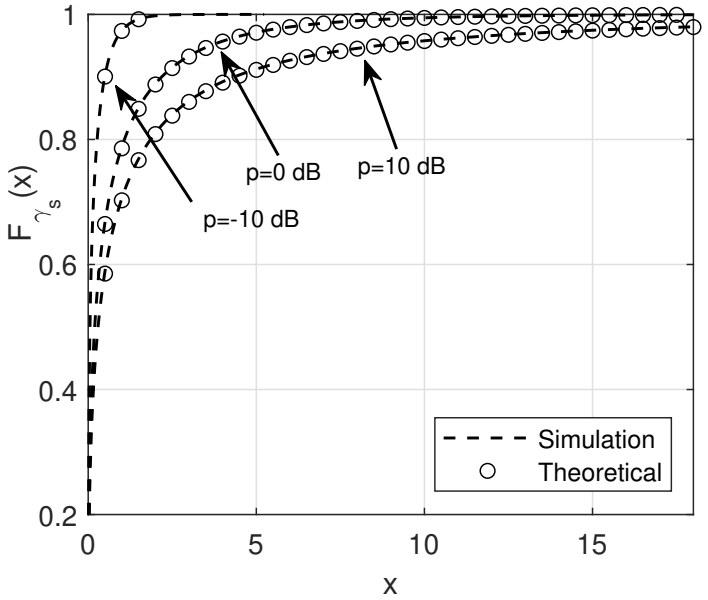

Figure 12: Simulation and theoretical outage probability in general region of SU at different peak power values of $p = -10, 0, +10$ dB.

for $\lambda_p = 2, 3$ and 4. It can be intuitively inferred that a high capacity demand from a PU should set the dynamic IT very tight, thereby restricting the transmit power for SU. Correspondingly, a low capacity demand from a PU should relax the IT, allowing the SU to opportunistically increase its transmit power. This phenomenon can be easily seen from Fig. 13, where for any SINR value, the outage in case of $\lambda_p = 4$ is more than $\lambda_p = 3$, and that is even more than the case of $\lambda_p = 2$. In case of high power region, the expression given in (2.5.6) will yield similar inferable results.

Moving forward, first the effect of varying λ_p (capacity parameter) at fixed SU transmit power levels, and then the effect of changing peak power at various fixed λ_p will be evaluated and analyzed for the mean capacity expression generated for SU in (2.4.25). For the first case, we select three peak power levels of $p = 5, 10, 15$ dB, while λ_p is varied from 1 to 5. As one may expect, high peak transmit power will allow the SU to have higher capacity as compared to low peak transmit power, however, as the λ_p increases (high PU capacity demand), the dynamic IT that will be set by CBS for SU will become tighter. This tight IT will therefore limit the SU transmit power, ultimately resulting in a lower mean capacity.

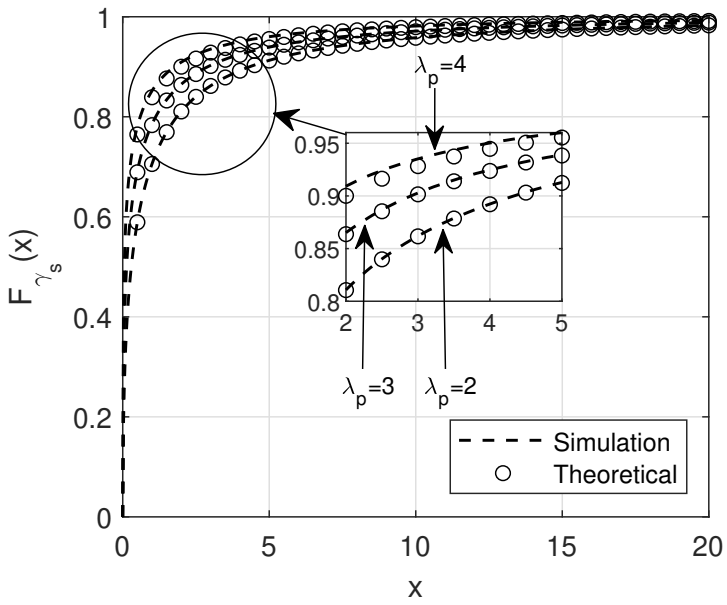

Figure 13: Simulation and theoretical outage probability in general power region of SU at $\lambda_p = 2, 3, 4$

.

This interesting phenomenon can be easily observed in Fig. 14 in which the simulation and theoretical result plots are compared with each other.

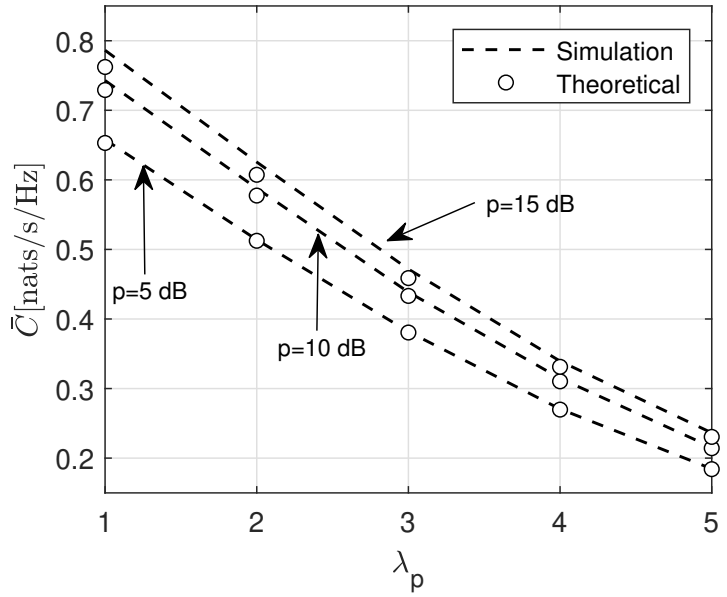

Figure 14: Simulation and theoretical mean capacity of SU at $p = 5, 10, 15$ dB, while varying the λ_p from 1 to 5.

In the next step, the peak power is varied from 5 to 10 dB and the mean capacity is evaluated at three different values of λ_p as $2, 3$ and 4. As expected, increasing peak power of SUs at relaxed dynamic IT (small λ_p) will increase the SU mean capacity more than at low SU peak power with high λ_p. This mechanism is due to the dynamic setting of IT, which is

governed by the PU capacity changes (capacity demand). Fig. 15 shows the resulting plots, where the network dynamics (traffic data demand) is reflected in the setting of dynamic IT and which in turn gets reflected in the mean capacity. The same is also inferred in the high power region for which the mean capacity expressions are evaluated numerically.

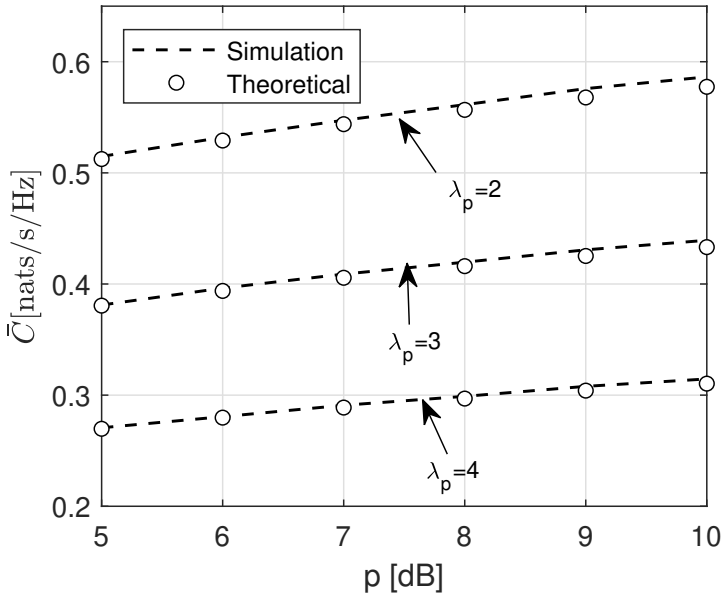

Figure 15: Simulation and theoretical mean capacity of SU at different values of $\lambda_p = 2, 3, 4$ while varying the peak power from 5 to 10 dB.

Fig. 16 and Fig. 17 show the corresponding mean capacity plots for SU in the high power region.

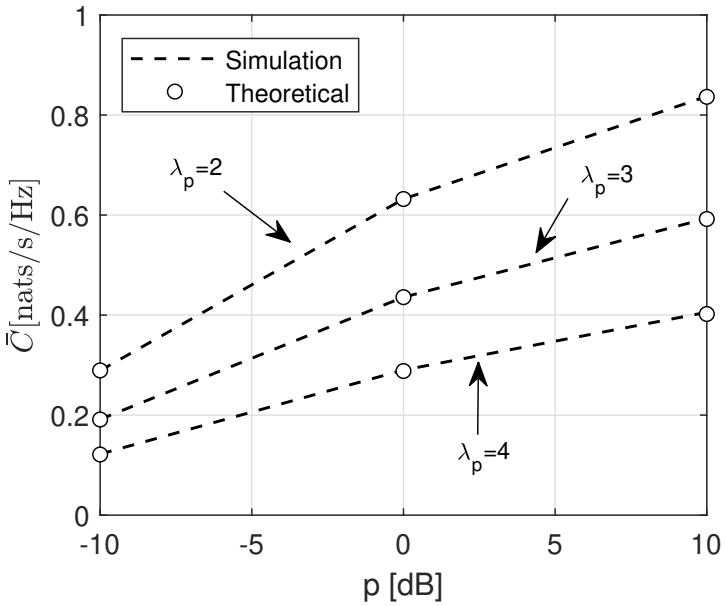

Figure 16: Simulation and theoretical mean capacity of SU at different values of $\lambda_p = 2, 3, 4$ while varying the peak power from -10 to 10 dB in high power region.

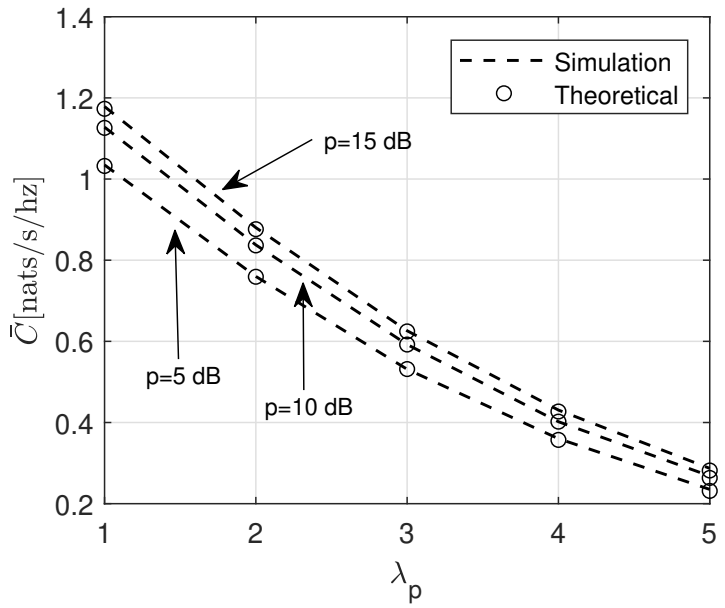

Figure 17: Simulation and theoretical mean capacity of SU at $p = 5, 10, 15$ dB, while varying λ_p from 1 to 5 in high power region.

Finally, we will simulate and compare the case of using dynamic IT with the fixed IT values set at -10 and -5 dB values for mean and instantaneous capacity performance, with outage probability. One important point to note here is that these set values for fixed IT are pre-chosen to be very tight, and represent the worst case scenario. In this case, the peak power is fixed at 10 dB, and λ_p is varied from 1 to 6 to generate the dynamic IT, and thereby the mean capacity.

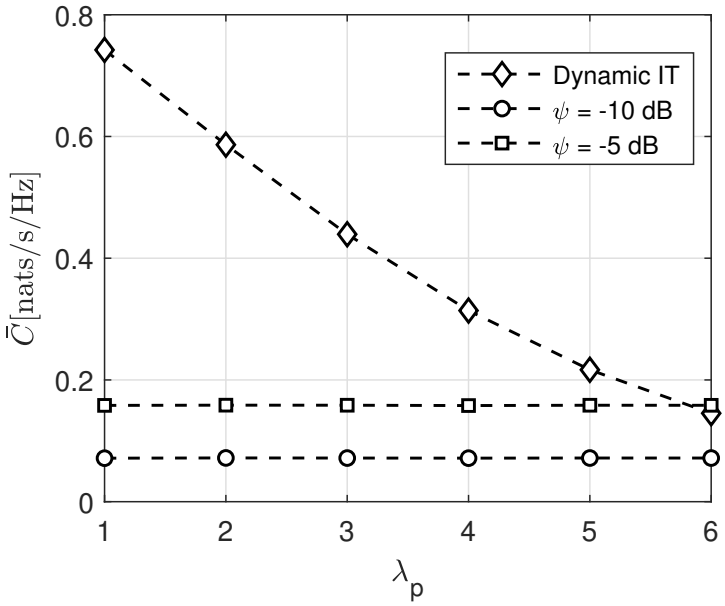

Figure 18: Comparison of mean capacity performance with dynamic IT and fixed IT of $\psi = -10$ and -5 dB.

Fig. 18 shows the resulting plot of such a case, and it can be observed that the mean capacity achieved by a SU with dynamic IT is higher than that with the fixed IT one as it takes care of the capacity variation of PU. In other words, a smaller value of λ_p will relax the IT, thereby allowing SU to have high transmit power and therefore, high mean capacity. On the other hand, a high value of λ_p will reflect a tight IT value for SU, thus limiting the SU transmit power which finally results in low mean capacity.

In the second case, we will compare the simulated instantaneous capacity performance with dynamic IT, and with the fixed IT values set at -10 and -5 dB. Fig. 19 shows the result for 30 time flops, and it can be clearly observed that setting dynamic IT leads to better instantaneous network capacity than the fixed IT case with the same reasoning as in the previous case. In the last case, we will compare the simulated outage probability of SU with respect to dynamic IT and fixed IT kept at -10 and -5 dB with λ_p set at 1. Please note that the effect of varying λ_p on outage probability is already shown in Fig. 13. As expected with the setting of dynamic IT, the outage probability would be less than the fixed IT case at any given SINR value, which can be easily observed from Fig. 20.

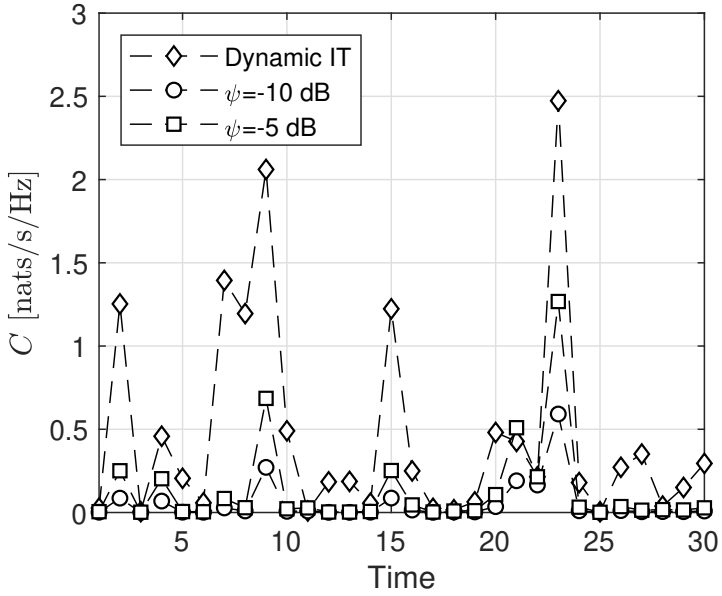

Figure 19: Comparison of instantaneous capacity performance with dynamic IT and fixed IT of $\psi = -10$ and -5 dB.

Also, one can observe that the outage probability in case of stricter IT, which is kept at -10 dB, is more than the case with fixed IT of -5 dB. Therefore, the positive effects of setting IT as a dynamic value can be easily seen on the outage probability, and on the mean and instantaneous capacity of SU. In the next section, we will dwell into the other part this chapter where we will analyze and examine the secondary user interference on PU network. This is very important in the sense that the IT is actually set by the PU and this dynamic IT discussed till now has to consider this interference to set that value accordingly.

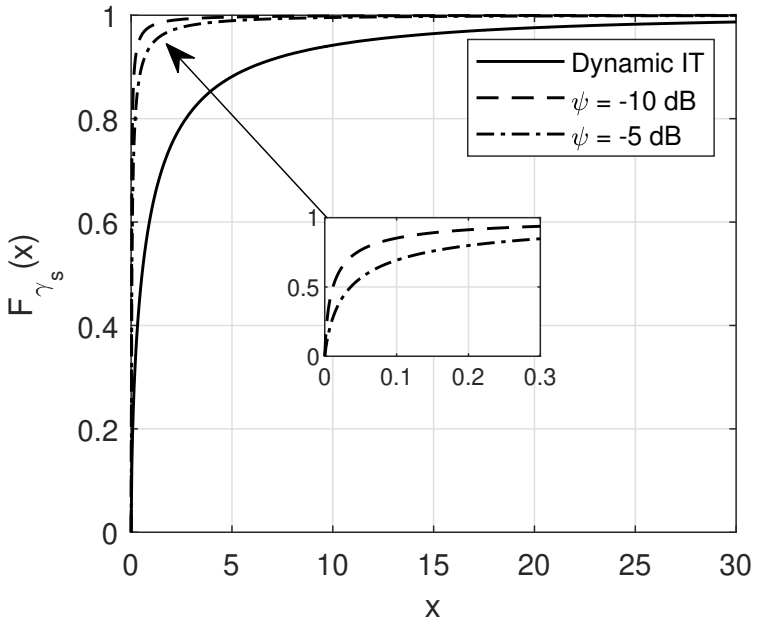

Figure 20: Comparison of outage probability with dynamic IT with fixed IT kept at $\psi = -10$ and -5 dB.

2.7 Impact of Secondary User Interference on Primary Network in Cognitive Radio Systems

The impact of SU interference on primary network is an important aspect to consider as it is the PU that sets the IT. Therefore, to asses the performance and other quality of service (QoS) parameters, closed form expression need to be derived and validated. In this section, we will focus on the mathematical foundation to derive these necessary performance expressions. This theoretical analysis is done by first considering interference from a single SU and then extended to the case of interference from multiple SUs on primary network. In short, in this section,

- PDF and CDF expressions for noise plus interference, signal to noise and interference ratio (SINR) will be derived for both cases of interference from a single SU and multiple SUs on PU network.
- Closed form mean SINR expression, mean capacity and outage probability expressions are derived.
- The expression generated above are validated with simulation results to show the accuracy of the theoretical expressions.

2.7.1 Theoretical Analysis

The considered cognitive radio network is shown in Fig. 21. It consists of n-SUs (SU network) and k-PUs with a secondary base station (SBS) and a primary base station (PBS). Since we are analyzing the effect of SU on PU network, channel gain between PU and SBS is not considered, and also we don't need to include the interference among PUs because

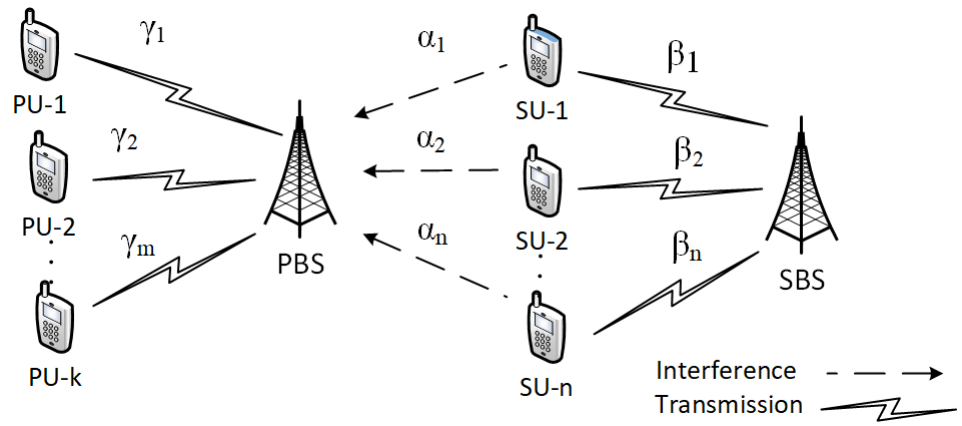

Figure 21: Underlay cognitive network with n-SUs sharing the spectrum with PU network of k-PUs. The channel power gain between any SU-i (i^{th} user) and PBS is denoted by α_i, between any SU-i (i^{th} user) and SBS by β_i and between i^{th}-PU and PBS by γ_i.

of assumed orthogonal resource allocation between them. In addition, since the channel fading is assumed to be Rayleigh distributed, the channel power gains follow an exponential distribution. We will consider the peak power adaptation as before for this scenario also [10, 11]. Therefore, the secondary transmit power as defined earlier is given by:

$$P^{tx} = \min\left\{p, \frac{q}{\alpha}\right\} \tag{2.7.1}$$

For theoretical analysis and tractability purpose, it is assumed that there are n-SUs that form the underlay cognitive network with primary user, where $n = \{1, 2, 3 \ldots, n\}$. Furthermore, the thermal additive white Gaussian noise (AWGN) in the network is assumed to have circularly symmetric complex Gaussian distribution with zero mean and variance as σ^2, i.e., $\mathcal{CN}(0, \sigma^2)$. Hence, the interference observed at primary receiver because of a single SU and multiple SUs with peak power adaptation will be given as:

$$\begin{aligned} I_{\text{single}} &= \alpha P_{sec} = \min\{\alpha p, q\}, \\ I_{\text{multi}} &= \min\left\{\sum_{i=1}^{n} \alpha_i p, q\right\}. \end{aligned} \tag{2.7.2}$$

Eq. (2.7.2) represents a minimum of a random variable and a constant[4]. From the theory of mixed random variables [77–79], a constant, c, can be modelled as a random variable with PDF equal to $\delta(x-c)$ and CDF equal to $H(x-c)$, where $H(x)$ is a Heaviside function and $\delta(x)$ is a Dirac Delta function. So with interference from a single SU, the CDF and PDF of minimum of two independent random variables is then given by:

$$\begin{aligned} F_I(x) &= F_{\alpha p_0}(x) + F_q(x) - F_{\alpha p_0}(x) F_q(x), \\ F_I(x) &= 1 - e^{-\frac{\lambda x}{p}}(1 - H(x-q)). \end{aligned} \tag{2.7.3}$$

[4]For illustration purposes, the value's of peak power p and interference temperature q are chosen to be in linear scale. However, the expressions derived in this paper hold for any value of p and q for any scale.

On including noise $\mathcal{CN}(0,\sigma^2)$, the CDF of noise plus interference will be then,

$$F_{IN}(x) = 1 - e^{-\frac{\lambda(x-\sigma^2)}{p}}(1 - H(x-\sigma^2-q)). \tag{2.7.4}$$

Correspondingly, the PDF of interference and noise is given by differentiating this CDF with respect to noise and interference variable x,

$$\begin{aligned} f_{IN}(x) = \frac{\lambda}{p}e^{-\frac{\lambda(x-\sigma^2)}{p}}\Big(1 - H(x-\sigma^2-q) \\ + \frac{p}{\lambda}\delta(x-\sigma^2-q)\Big), \ \ \forall\ \sigma^2 \le x \le \infty. \end{aligned} \tag{2.7.5}$$

For the case of interference from multiple SUs, the distribution of of interference given in Eq. (2.7.2) will follow Gamma distribution[5], $f_{\bar{\gamma}}(x,\kappa,\theta)$, where κ and θ represent the shape and rate parameter. The PDF and CDF of Gamma distribution is given as

$$\begin{aligned} f_{\bar{\gamma}}(x) &= \sum_{i=1}^{n}\alpha_i p = \bar{\gamma}\left(x, n, \frac{\lambda_2}{p}\right) = \bar{\gamma}\left(x, n, \bar{\lambda}\right), \\ &= \frac{\bar{\lambda}^n x^{n-1}}{\Gamma(n,0)}e^{-\bar{\lambda}x}, \ \forall\ \left\{x \ge 0, n > 0, \bar{\lambda} > 0\right\}, \\ F_{\bar{\gamma}}(x) &= 1 - \frac{\Gamma\left(n, \bar{\lambda}x\right)}{\Gamma(n,0)}, \ \forall\ \left\{x \ge 0, n > 0, \bar{\lambda} > 0\right\}, \end{aligned} \tag{2.7.6}$$

where n is the total number of SUs in the underlay network, $\bar{\lambda} = \lambda_2/p$ is the scaled rate parameter between SU and PBS and $\Gamma(a,x)$ is an incomplete gamma function defined as:

$$\Gamma(a,x) = \int_a^\infty t^{a-1}e^{-t}dt, \ \forall\ a > 0, x \ge 0.$$

Following the same mathematical approach that was used in single SU case, the distribution of noise plus interference in multiple SUs case is then derived as:

$$\begin{aligned} F_{NI}^m(x) &= 1 - \frac{\Gamma\left(n, \bar{\lambda}(x-\sigma^2)\right)}{\Gamma(n,0)} + H(x-\sigma^2-q)\frac{\Gamma\left(n, \bar{\lambda}(x-\sigma^2)\right)}{\Gamma(n,0)}, \\ f_{NI}^m(x) &= \frac{\Gamma\left(n, \bar{\lambda}(x-\sigma^2)\right)}{\Gamma(n,0)}\delta(x-\sigma^2-q) + \bar{\lambda}^n \\ &\quad \times \frac{(x-\sigma^2)^{n-1}}{\Gamma(n,0)}e^{-\bar{\lambda}(x-\sigma^2)}[1 - H(x-\sigma^2-q)], \end{aligned} \tag{2.7.7}$$

where σ^2 is the $\mathcal{CN}(0,\sigma^2)$. Fig. 22 and Fig. 23 plots the CDF and PDF for the theoretical expression (Eq. (2.7.7)) with the simulation result of $p > q$ and $q < p$ for different SU densities of $n = 1, 2, 3$.

[5] The distribution of sum of independent exponential random variables with the same rate parameters follows Gamma distribution. Also, to distinguish between the channel γ between PU and PBS, the Gamma distribution is denoted as $\bar{\gamma}$ in this study.

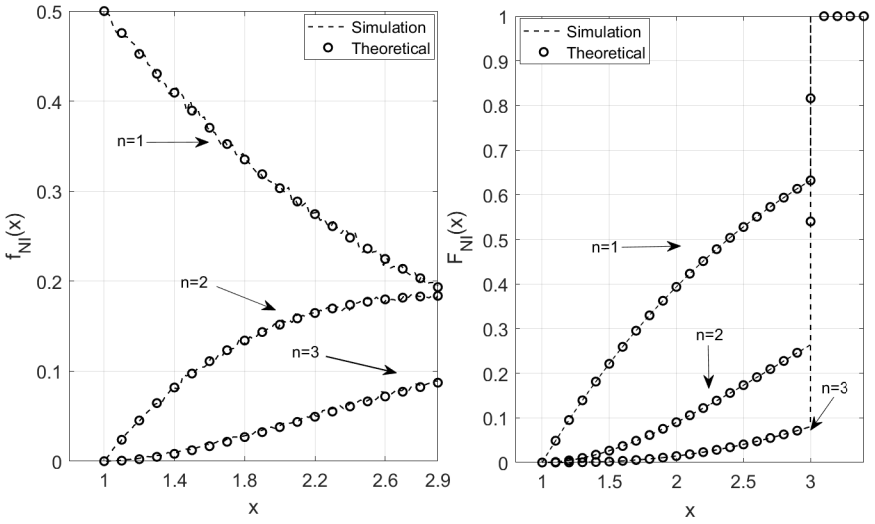

Figure 22: PDF and CDF of noise and interference for different number of SUs ($n = 1, 2, 3$), when $p > q$, where $p = 4$, $q = 2$ and $\sigma^2 = 1$ with support region from $\sigma^2 \leq x \leq \infty$.

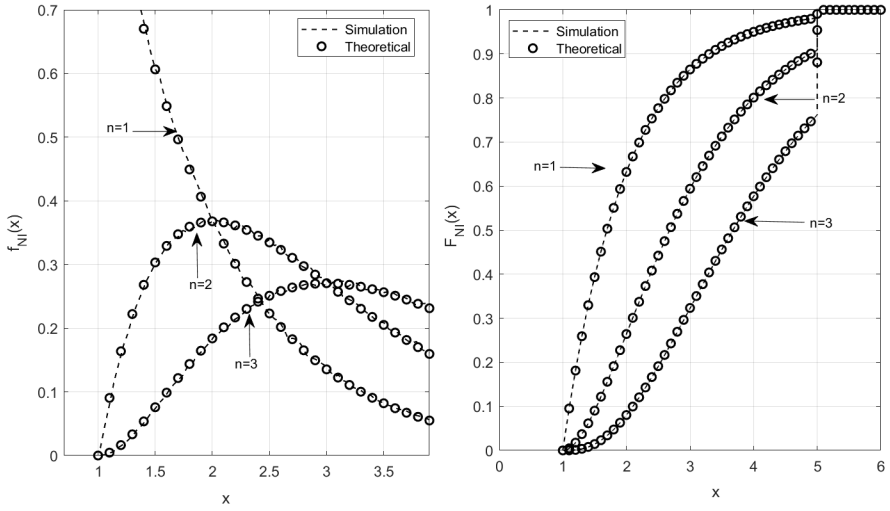

Figure 23: PDF and CDF of noise and interference for different number of SUs ($n = 1, 2, 3$) when $p < q$, where $p = 2$ $q = 4$ and $\sigma^2 = 1$ with support region from $\sigma^2 \leq x \leq \infty$.

2.7.2 Instantaneous SINR of PBS

The instantaneous SINR at PBS considering the system model (Fig. 21) is given by:

$$\text{SINR} = \frac{\gamma p}{\sigma^2 + I}, \tag{2.7.8}$$

where I is the interference from SUs given by Eq. (2.7.2). The distribution of numerator is a scaled exponential distribution and the distribution of denominator is already derived in the previous section (Eq. (2.7.5) and Eq. (2.7.7)). Therefore, the PDF of ratio of two independent random variables [86] i.e. $z = x/y$, where $x = \gamma p$ and $y = \sigma^2 + I$ will be given

as

$$f_z(z) = \int_{\sigma^2}^{\infty} y \cdot f_{x,y}(yz, y)dy = \int_{\sigma^2}^{\infty} y \cdot f_x(yz)f_y(y)dy, \ \forall \ y \geq 0. \tag{2.7.9}$$

For the interference from a single SU user, the SINR distribution will be as follows:

$$\begin{aligned} f_z(z) &= \int_{\sigma^2}^{\infty} y \cdot \frac{\lambda_1 e^{\frac{-\lambda_1 yz}{p}}}{p} \frac{\lambda_2}{p} e^{-\frac{\lambda_2(y-\sigma^2)}{p}} \Big\{1 - H(y - \sigma^2 - q) + \frac{p}{\lambda_2}\delta(y - \sigma^2 - q)\Big\}dy \\ &= \frac{\lambda_1\lambda_2}{p^2} e^{\frac{\lambda_2\sigma^2}{p}} \left\{ \int_{\sigma^2}^{\infty} y \cdot e^{\frac{-y(\lambda_1 z + \lambda_2)}{p}} dy - \int_{\sigma^2+q}^{\infty} y \, e^{\frac{-y(\lambda_1 z + \lambda_2)}{p}} dy \right. \\ &\qquad \left. + \frac{p}{\lambda_2}(\sigma^2 + q) e^{\frac{-(\sigma^2+q)(\lambda_1 z + \lambda_2)}{p}} \right\}. \end{aligned}$$

By using integration by parts and on further simplification, the PDF is reduced to:

$$f_z(z) = \frac{\lambda_1\lambda_2}{\Lambda p} \left\{ e^{\frac{-\sigma^2\lambda_1 z}{p}} \left(\sigma^2 + \frac{p}{\Lambda}\right) + \ e^{-\frac{\sigma^2\lambda_1 z + q\Lambda}{p}} \left(\frac{(\sigma^2 + q)\lambda_1 z}{\lambda_2} - \frac{p}{\Lambda}\right) \right\}, \tag{2.7.10}$$

where Λ is the scaled and shifted random variable version [6] of z given by $\Lambda = \lambda_1 + \lambda_2 z$. Under the scenario of $\lambda_1 = \lambda_2 = 1$, with AWGN as $\mathcal{CN}(0, \sigma^2 = 1)$, the PDF can be further simplified to

$$f_z(z) = \frac{1}{p(z+1)} \left\{ e^{\frac{-z}{p}} \left(1 + \frac{p}{z+1}\right) + e^{-\frac{z+q(z+1)}{p}} \left((1+q)z - \frac{p}{z+1}\right) \right\}. \tag{2.7.11}$$

Following the same analytical framework used for the single SU case, the distribution with interference from multiple SUs will be:

$$\begin{aligned} f_z^m(z) = \int_{\sigma^2}^{\infty} y\bar{\lambda_1} e^{-\bar{\lambda_1} yz} \Big\{ & f_{\bar{\gamma}}(y - \sigma^2, n, \bar{\lambda}) + \delta(y - \sigma^2 - q)(1 - F_{\bar{\gamma}}(y - \sigma^2, n, \bar{\lambda})) \\ & - f_{\bar{\gamma}}(y - \sigma^2, n, \bar{\lambda}) H(y - \sigma^2 - q) \Big\} dy. \end{aligned} \tag{2.7.12}$$

which on further evaluation and simplification reduces to

$$\begin{aligned} f_z^m(z) = \bar{\lambda_1}\bar{\lambda}^n e^{-\sigma^2\bar{\lambda_1} z} \Theta^{-1-n} & \left[n + \left(\sigma^2\Theta \left[1 - \frac{\Gamma(n, q\Theta)}{\Gamma(n, 0)} \right] \right) - \frac{\Gamma(n+1, q\Theta)}{\Gamma(n, 0)} \right] \\ & + \bar{\lambda_1}(\sigma^2 + q) \frac{\Gamma(n, q\bar{\lambda})}{\Gamma(n, 0)} e^{-\bar{\lambda_1}(\sigma^2+q)z}, \end{aligned} \tag{2.7.13}$$

where Θ is the scaled and shifted random variable version[7] of z given by $\Theta = \bar{\lambda} + \bar{\lambda_1} z$. Fig. 24 shows the plot of the derived theoretical expression with simulation data for the two cases of $p < q$ and $p > q$ with different SU densities ($n = 1, 2, 3$).

[6] λ_1 is the channel rate parameter between PU and PBS, whereas λ_2 is the channel rate parameter between SU and PBS.

[7] Here $\bar{\lambda} = \lambda_2/p$ is the scaled rate parameter of SUs and $\bar{\lambda_1} = \lambda_1/p$ is the scaled rate parameter for PU.

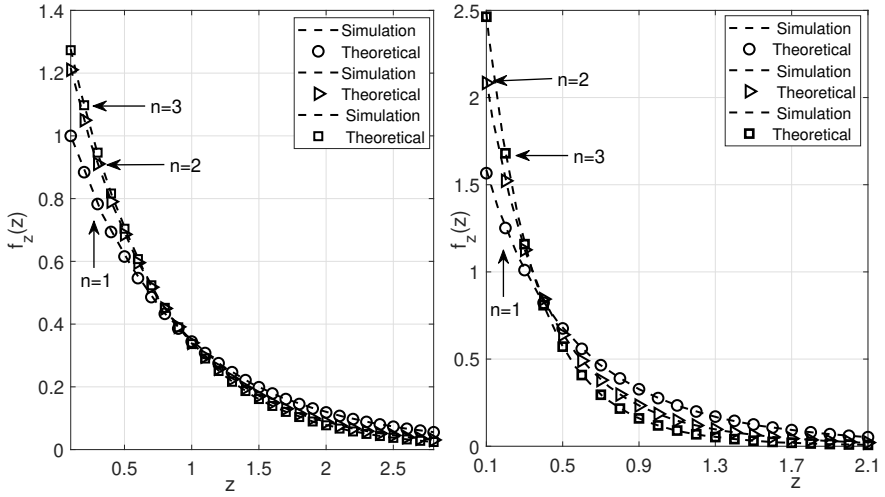

Figure 24: PDF of SINR for two cases of $p < q$ and $p > q$ for different number of SUs ($n = 1, 2, 3$).

In the following sections, we will look into the crucial performance metrics (outage probability and capacity) of underlay cognitive network. The mentioned approach can be extended to the case of interference from multiple SUs given that the important SINR expression Eq. (2.7.13) for multiple SUs is already been derived. However, given the space limitations, the derivations considering multiple SUs are not detailed herein in coming sections. Nonetheless, the fundamental case of interference from single SU case has been presented in detail.

2.7.3 Mean SINR of PBS

The mean SINR, therefore, is given as $\mu = \int_0^\infty z f_z(z) dz$ where the PDF of SINR $f_z(z)$ was derived in Eq. (2.7.11). Thus,

$$\begin{aligned}\mu &= \int_0^\infty z\Big\{\frac{1}{p(z+1)}\Big\{e^{\frac{-z}{p}}\left(1+\frac{p}{z+1}\right)+e^{-\left(\frac{z+q(z+1)}{p}\right)}\left((1+q)z-\frac{p}{z+1}\right)\Big\}dz,\\ &= \int_0^\infty \left(\frac{ze^{\frac{-z}{p}}}{p(z+1)}\right)dz+\int_0^\infty\left(\frac{ze^{\frac{-z}{p}}}{(z+1)^2}\right)dz+\int_0^\infty\left(\frac{z^2(1+q)e^{-\left(\frac{z+q(z+1)}{p}\right)}}{p(z+1)}\right)dz\\ &\qquad -\int_0^\infty\left(\frac{ze^{-\left(\frac{z+q(z+1)}{p}\right)}}{(z+1)^2}\right)dz.\end{aligned}$$

which on further simplification reduces to

$$\mu = e^{\frac{1}{p}}\left\{\Gamma\left(0,\frac{1}{p}\right)-\Gamma\left(0,\frac{1+q}{p}\right)\right\}+\frac{pe^{\frac{-q}{p}}}{1+q}. \tag{2.7.14}$$

Fig. 25 shows that the change in mean SINR while varying the interference temperature q for a constant peak transmit power p. The higher transmit power (for both PU and SU) with lower interference temperature gives better mean SINR than lower transmit power (for both PU and SU) with high IT constraint.

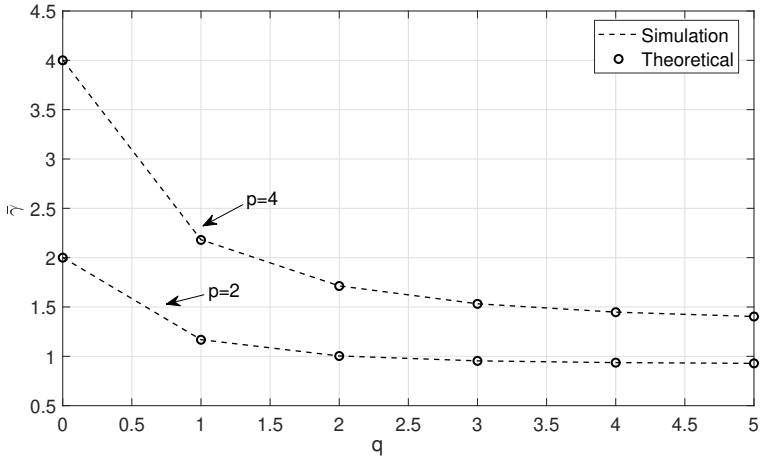

Figure 25: Mean SINR vs Interference Temperature, q, for $p = 2$ and $p = 4$.

2.7.4 Outage Probability of Primary Network

The outage probability as described earlier is the probability when the instantaneous SINR drops below a given threshold. Mathematically, this is given as: $Pr(\gamma \leq \psi) = F_z(\psi)$, which is nothing but the CDF of SINR. Therefore,

$$\begin{aligned} F_z(\psi) &= \int_0^{\psi} f_z(z)dz, \\ &= \int_0^{\psi} \left(\frac{e^{\frac{-z}{p}}}{p(z+1)} \right) dz + \int_0^{\psi} \left(\frac{e^{\frac{-z}{p}}}{(z+1)^2} \right) dz + \int_0^{\psi} \left(\frac{z(1+q)e^{-\left(\frac{z+q(z+1)}{p}\right)}}{p(z+1)} \right) dz \\ &\qquad - \int_0^{\psi} \left(\frac{e^{-\left(\frac{z+q(z+1)}{p}\right)}}{(z+1)^2} \right) dz. \end{aligned}$$

which on further integration and simplification reduces to

$$F_z(\psi) = 1 - \frac{e^{\frac{-\psi}{p}}}{\psi + 1} \left(1 + \psi e^{\frac{-q(\psi+1)}{p}} \right)$$

It can be directly inferred from Fig. 26 that if $q > p$, the outage probability is higher than in the case of $p > q$. In addition to this inference, it can be also observed that the theoretical expressions derived are in sync with the simulation results, i.e., increase the spectral efficiency of the network.

2.7.5 Instantaneous Capacity of Primary Network

The PDF of instantaneous capacity can be readily found from the PDF of instantaneous SINR by using transformation of random variables method [77, 78]. This can be obtained by using:

$$f_x(x) = f_z(z) \left| \frac{dz}{dx} \right|_{z=e^x-1},$$

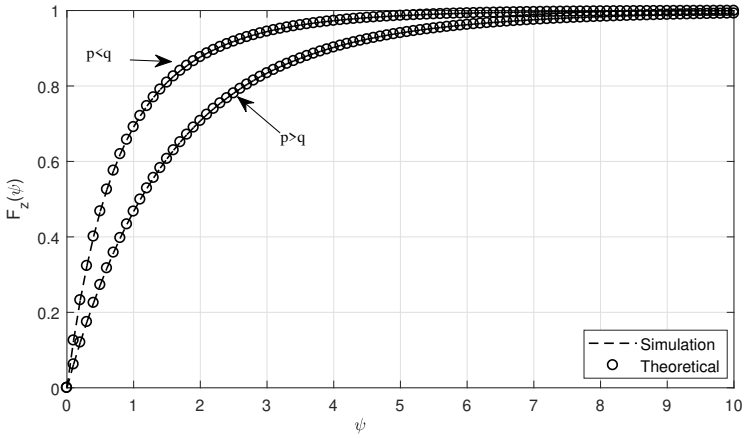

Figure 26: Outage probability of PU for $p < q$, where $p = 2$ and $q = 4$ and for $p > q$, where $p = 4$ and $q = 2$.

where $f_z(z)$ is derived in Eq. (2.7.11) for the case of interference from single SU on primary network. It can be seen from Fig. 27 that there is a point where the instantaneous capacity

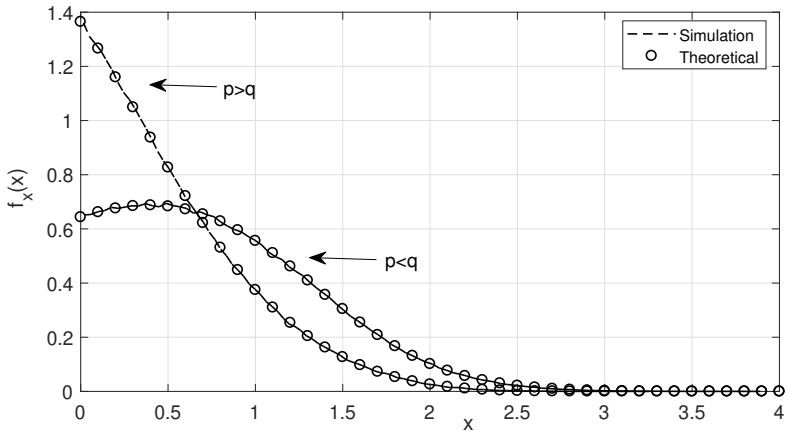

Figure 27: Instantaneous PDF of Capacity for $p < q$, where $p = 2$ and $q = 4$ and for $p > q$, where $p = 4$ and $q = 2$.

for $p < q$ goes below $p > q$. It proves the point that the interference temperature should not be kept constant rather should be dynamic in nature to exploit full potential of the network, which has been statistically modeled in the first port of this chapter.

2.7.6 Mean Capacity of Primary Network

The average capacity from the PDF of instantaneous SINR ($f_z(z)$) is given as:

$$\bar{C} = \int_0^\infty \log(1+z) f_z(z) dz.$$

Substituting Eq. (2.7.11) in the above expression and on further evaluation.

$$\bar{C} = \frac{e^{\frac{1}{p}}}{p}\left[\Gamma\left(0, \frac{z+1}{p}\right) - \Gamma\left(0, \frac{(q+1)(z+1)}{p}\right)(p+q+1)\right] - \\ \times \frac{e^{\frac{1-(q+1)(z+1)}{p}}}{z+1}\left\{e^{\frac{q(z+1)}{p}}\Big(1+\log(z+1)\Big) + z\log(z+1) - 1\right\}\Bigg|_0^\infty . \tag{2.7.15}$$

At $z = \infty$, $\Gamma(0, z) \to 0$ and also, $\frac{e^{\frac{1-(q+1)(z+1)}{p}}}{z+1} \to 0$.
Therefore, the final mean capacity expression will be evaluated at $z = 0$:

$$\bar{C} = 1 - e^{-\frac{q}{p}} + \frac{e^{\frac{1}{p}}}{p}\left[(p+q+1)\Gamma\left(0, \frac{q+1}{p}\right) - \Gamma\left(0, \frac{1}{p}\right)\right]$$

Fig. 28 shows the plot of this theoretical expression with simulation results for two cases of transmit power $p = 2$ and $p = 4$. Intuitively, high transmit power $p = 4$ will result in high capacity for the network than the low transmit power of $p = 2$ but when the interference temperature is relaxed, the interference caused due to secondary user on primary will also increase that in turn will reduce the overall capacity.

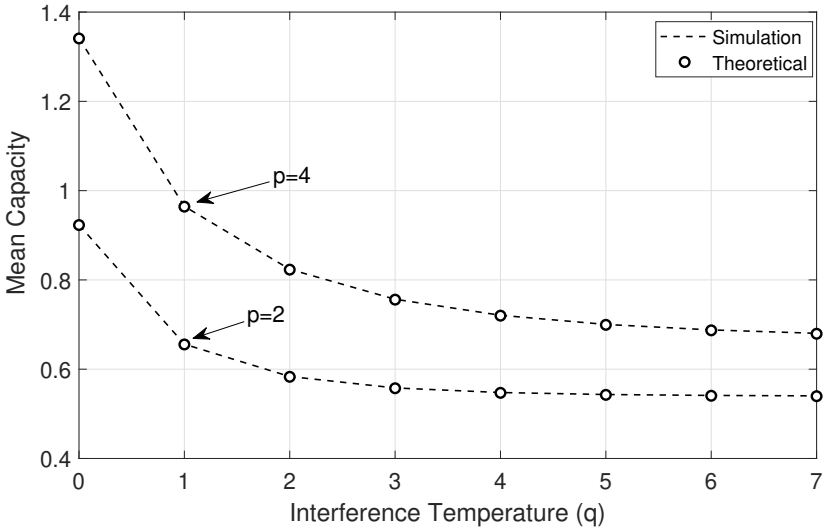

Figure 28: Theoretical and simulation result plots for capacity at $p = 2$ and $p = 4$ with varying interference temperature: q.

At this point, we have modeled the dynamic IT in CRN , and shown it's benefits and also shown the effect of SU interference on PU. Now, we will conclude this chapter on spectrum optimization with CRN in the next section.

2.8 Conclusions

The overall conclusions and contributions from this chapter of statistical modeling of interference temperature and its effect on network performance of a cognitive radio network are as follows,

1. The dynamic IT based CRN has better network performance in terms of high instantaneous and mean capacity, with low outage probability as compared to the CRN with a fixed IT.

2. Theoretical PDF and CDF expressions for SINR from variable Poisson distributed capacity demand of a PU is determined and validated with the simulation results.

3. Theoretical PDF and CDF of dynamic interference power threshold are derived and checked with simulations.

4. Theoretical derivations of outage probability and mean capacity of SU in general operating region, and in high power region are found and validated with simulations.

5. Performance analysis of primary user network considering interference from the SU network.

In the next chapter, we will step toward the high frequency in the radio spectrum and will discuss the utility of UAV in UAV-assisted next-generation wireless communication systems. In particular, in next chapter, an empirical study is ocnducted where the the UAV2W wireless channel at UWB is studied and modeled in an indoor warehouse type environment for different wireless channel characteristics.

CHAPTER III

UWB-UAV2W CHANNEL MODELING

3.1 Introduction

In the previous chapter, we looked into the case of efficient utilization of radio spectrum by setting the IT value as a dynamic variable that takes care of the network traffic in a cognitive radio networks. The results showed higher network capacity and lower outage probability as compared to a traditional network utilizing static IT. The optimization of a spectrum can work for some time but eventually, need to find higher bandwidth and higher frequency will supersede the results generated by optimization of spectrum resources. Therefore, in this chapter, we will examine such high bandwidth and high frequency next generation technology, that is ultra-wideband (UWB). In recent years, UWB technology has attracted a lot of attention not only from the academia but also from the industry as well. In UWB technology, the bandwidth is greater than or equal to 500 MHz and works between 3.1 GHz-10.6 GHz. The main reasons behind its popularity is the low-power consumption and high bandwidth with low probability of interception [36–39].

This low power consumption and short wavelength makes the UWB as a best possible candidate for the body-centric wireless network [40, 41] in health-care applications [37, 38]. The Federal Communication Commission's (FCC) power requirement of -41.3 dBm/MHz or 75 nanowatts/MHz classifies UWB as an unintentional radiators which allows it to lie below the noise floor for a narrowband receiver and thereby can easily coexist with current wireless technologies like WiFi with minimal or no interference. In summary, the main advantages of UWB can be listed as follows,

- Low power consumption with high data rate. The received power in UWB lies very close to the noise floor, [36–39, 42].
- Control over duty cycle makes the battery last longer.
- Low probability of detection as it is close to the noise floor and any attempt of jamming or eavesdropping will make the signal noisy, [43].
- Small wavelength with low power makes it a perfect fit for body-centric wireless network, [37, 38].

On the other hand, unmanned aerial vehicles (UAVs) are being now used for remote healthcare deliveries especially to far flung areas that lack connectivity. UAVs are also considered to be the next frontier in technology advancement especially in the retail, defense and health care sectors [87–89]. In retail, UAVs are being utilized to do warehouse operations

such as inventory management, stock counting by RF tagging or by using computer vision. The main advantage of utilizing UAVs for such operations is that it is far more time efficient than human and forklift trucks [90, 91]. Although the pick and drop of items capability is still limited but in future that would not be a limitation anymore given the advancements in UAV technology, internet of things (IoT), and machine learning (ML) over the years. In healthcare, UAVs are also being used for emergency medical deliveries where time is of utmost importance, such as during cardiac arrests, [87, 87–89, 92]. One of the upcoming themes for UAVs is to directly monitor the health of a patient by utilizing wearable patch devices, [42, 87, 92–94]. The study in this chapter explores the UWB technology with UAVs further for health monitoring applications. This type of set-up involving UAV and wearable antenna/antenna's is also known as unmanned aerial vehicle-to wearable (UAV2W) systems, [42].

Lately, in literature there are bundle of UWB radio channel characteristics campaigns for on-body and off-body scenarios. In [39, 95–100], on-body UWB radio channel characterization and modeling were investigated in detail. However, most of the research on off-body radio channel has a controlled environment, where antennas are placed in standalone position. In [101,102], UWB radio channel modeling for UAV is presented without a real human subject. The closest research to our work is presented in [36,37], where the off- and on-body channel characterization were performed. The main difference with these work is that we have considered the UWB radio channel between a UAV and a human subject in our work. Another application of UAV is is the remote health-care in crowded or far-flung areas with no accessibility [87], or in the case of emergency like cardiac arrest [92], where UAVs can be used to send life saving drugs. The other important application is the direct health care monitoring from a UAV to the wearable device that is attached to a patient body, such a system was shown in the introduction chapter. These type of system is referred as unmanned aerial vehicle-to-wearable (UAV2W) systems in this chapter [42]. The rest of the chapter is as follows, Section II discusses about the measurement setup and data acquisition part, Section III covers the radio channel characterization, Section IV looks at the statistical modeling part and finally, Section V presents the conclusion.

3.2 Measurement Setup and Data Acquisition

There are generally two methods to measure the channel response in a wireless communication, either time correlator based or frequency sweep based. In our work, we have utilized the later one. Fig. 29 shows the measurement setup, where the transmitter (Tx) antenna was patched on a UAV while the wearable receiver (Rx) antenna was patched on a human subject. Both Rx antenna and Tx antenna were connected to the vector network analyzer (VNA) on port 1 and port 2 respectively. The transmit power was set at -40 dB to make the UWB power exist near the noise floor at such frequencies. One important observation here is that the noise floor changes with the bandwidth and the relationship between noise floor and bandwidth is given as,

$$\text{Noise floor (dBm)} = 10\log_{10}(kT) + 10\log_{10}(B) + NF, \tag{3.2.1}$$

where k is the Boltzmann's constant, T is the temperature of receiver system in Kelvins, NF is the noise figure of receiver and B is the given bandwidth. Therefore, for this type

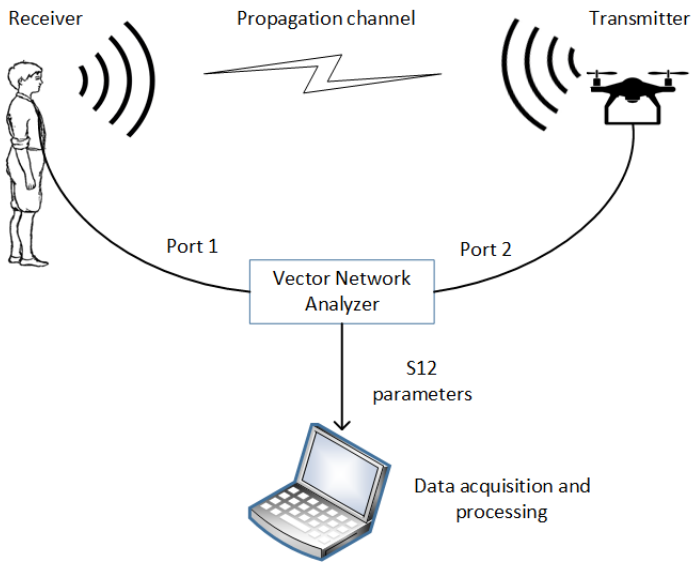

Figure 29: The UAV2W experiment setup with data acquisition and processing component

of setup, given the FCC regulations with the human subject involved, the transmit power of -40 dB was considered to be sufficient. Furthermore, no power amplifier was used in transmission path as is generally the case that does not involve human subject to take care of these regulations that include a human subject.

The VNA was further set up with the sweep time of 100 ms (milliseconds) to generate 1601 continuous wave tones that were uniformly distributed over the frequency range of 3.1-10.6 GHz; this frequency range is widely accepted for UWB related measurements. The VNA was then calibrated to remove the cable effects, which in indoor and small distances is manageable as compared to outdoor environment and over long distance in UWB. The measurement data or scattering data (S12 parameter) thus collected will be the channel transfer function in frequency domain. The S12 parameters were acquired and processed by Python and MATLAB scripts on a laptop. The data analysis was done on this recorded data set to find the UWB distance dependent and frequency dependent path loss factors and time dispersion parameters like root mean square time, maximum excess time that will be discussed in next section. The list of equipment with their individual specifications used in the measurement process are listed in Table 3.

Table 3: The measurement equipment with the specifications.

Equipment	Specifications
Vector Network Analyzer	Agilent 8722ES (50 MHz-40 GHz)
Calibration kit	Agilent 85032F
UAV	3 DR IRIS + Quadcopter
RF coaxial cables	Weight 2 lbs
2 Antenna sensors	OctaneBW-3000 (3 GHz-11 GHz)

The UWB antenna patch (Octane BW-3000-10000-EG [103]) used on a human subject is an Omni-directional wideband antenna with 5.5 dBi gain at 3 GHz, 8.2 dBi gain at 6

GHz and 6.3 dBi gain at 9 GHz. It is lightweight (2 ounces) and small in dimensions ($4.5'' \times 4.25'' \times 0.4''$) with voltage standing wave ratio (VSWR) less than 2:1. On the other hand, the UAV (IRIS+ quadcopter) has the maximum speed of 25 mph with 3 DR link communication [104]. The Octave antenna and IRIS+ quadcopter used in this study are shown in Fig. 30.

Figure 30: Octane antenna and IRIS+ quadcopter

On the human subject, 9 different body locations are selected for this measurement campaign. These 9 different body locations where the UWB antenna (Rx) was patched is shown in Fig. 31. On the other hand, the transmitter antenna was fixed on the UAV that was hovering at a fixed height from the ground. The human subject (receiver) moves 0.5 meter from one point to another on the ground (8 points in total) covering a diagonal range of 8.0 meter to 4.5 meters towards the UAV. The complete sketch plan with the 8 marked points on the ground, and with the farthest and nearest diagonal distance between an UAV and the human subject is shown in Fig. 32

At each distance point, a total of 10 snapshots of the data (S12) were recorded which were later on averaged to get a better redundant value. The time domain response from these frequency response measurements was computed by taking the Inverse Fast Fourier Transform (IFFT), which will then be discussed in detail in the next section. Fig. 33 shows the actual indoor warehouse environment where this measurement campaign was carried out. In the next section, we will dwell more into the data analysis part from the scattering data collection to characterize the UWB-UAV2W radio channel.

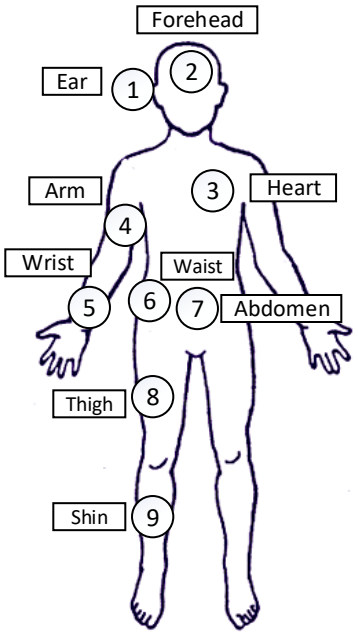

Figure 31: The UWB antenna patch locations on human body for line-of-sight (LOS) measurements in the indoor warehouse scenario

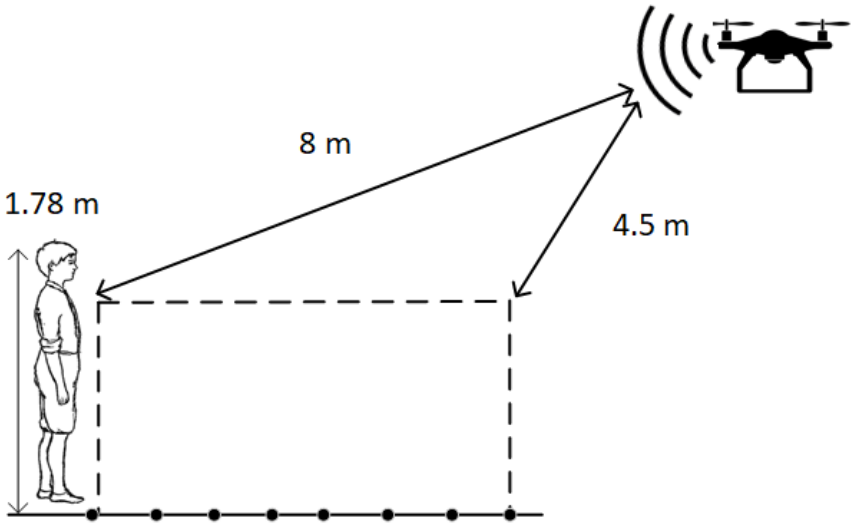

Figure 32: The sketch plan of the measurement setup for UWB off-body characterization with 8 points marked on the ground.

3.3 UWB-UAV2W Radio Channel Characterization

In this section, first analysis for the path gain modeling at different bandwidth corresponding to several frequency carriers will be done, and then the time dispersion analysis for UAV2W systems will be discussed in detail from the S12 data collected as mentioned in the previous section. In short, different bandwidth configurations corresponding to different carrier frequency will be analyzed for channel characterization.

Figure 33: Indoor warehouse environment for the campaign

3.3.1 Path Gain Analysis

Path gain analysis generally finds the rate of change in path gain with distance. However, at UWB frequencies, the path gain is not only dependent on distance but also on the frequency [105, 106]. The detailed path gain calculation for a UWB system is provided in these exceptional work of [105–107]. The distance dependent path gain[1] is well known to follow a log-distance model. Linear curve fitting will yield the path loss exponent or rate at which the path gain changes with log-distance. However, as mentioned earlier, at the UWB frequencies, the path loss is not just distance dependent but also frequency dependent. So, both frequency dependent as well as distance dependent path loss exponent need to be determined at UWB frequencies.

The total path gain as a function of distance and frequency, $\mathrm{PG}(f, d)$, assuming that the distance dependent path gain and frequency dependent path gain are independent [106–108] is given as,

$$\mathrm{PG}(f, d) = \mathrm{PG}(f) \cdot \mathrm{PG}(d). \tag{3.3.1}$$

The distance dependent path gain, $\mathrm{PG}(d)$ is modeled with the power law relationship while the frequency dependent path gain, $\mathrm{PG}(f)$ is modelled as, $\mathrm{PG}(f) \propto f^{-k}$, where k denotes the frequency dependent path loss factor. Therefore the total path gain is given as [105],

$$\mathrm{PG}_{dB}(f, d) = \overline{\mathrm{PG}}_{dB}(f_c, d_0) - 10n \log_{10}\left(\frac{d}{d_0}\right) - 20k \log_{10}\left(\frac{f}{f_c}\right) + X_\sigma(d), \tag{3.3.2}$$

where d is the distance between Tx and Rx, f is the carrier frequency under consideration, $\mathrm{PG}_{dB}(f_c, d_0)$ is the mean of $\overline{\mathrm{PG}}_{dB}(f_c, d_0)$ at a reference distance $d_0 = 1\ m$, and at the reference frequency $f_c = 1$ GHz. Also, n is the distance dependent path loss exponent, k is

[1]Path gain is described as the ratio of received power to the transmitted power while path loss is is the inverse of path gain that is (PL_{dB}=-PG_{dB}).

the frequency dependent exponent and $X_\sigma(d)$ is the shadowing factor which is assumed to be Gaussian distributed with zero mean (in dB) and a variance of σ^2 (in dB).

Moreover, in order to analyze the distance dependent and frequency dependent path loss exponent over different frequency bands, the UWB spectrum (3.1-10.6 GHz) can be divided into different bandwidths with different set of frequency carriers associated with it [107]. Table 4 shows the different frequency carrier set with the different bandwidths of 0.75, 1.5, 3.0, 3.75, 7.5 GHz.

Table 4: Frequency bandwidth with different carrier frequency.

BW (GHz)	Carrier frequency (f_c) GHz
0.75	3.47, 4.22, 4.97, 5.72, 6.47, 7.22, 7.97, 8.72, 9.47
1.5	3.85, 5.35, 6.85, 8.35, 9.85
3	4.60, 6.85, 9.10
3.75	4.97, 8.72
7.5	6.85

Thus, for each bandwidth, there will be different path loss exponent corresponding to the various frequency carriers at that bandwidth, for example at 3.0 GHz bandwidth there will be three path loss exponents corresponding to the three carrier frequencies of 4.6, 6.85 and 9.1 GHz. Now, to calculate the distance dependent S12 parameter, we need to average it over all the frequency tones, and similarly to determine the frequency dependent S12 parameter, we need to average it over all the distances. Using mean square error method, the S12 at a distance d and f is given as:

$$\begin{aligned} \mathrm{S12}_{dB}(d) &= 10\log_{10}\left(\frac{1}{M}\sum_{j=1}^{M}\frac{1}{N}\left[\sum_{i=1}^{N}|H(t_i,f_j,d)|^2\right]\right), \\ \mathrm{S12}_{dB}(f) &= 20\log_{10}\left(\frac{1}{L}\sum_{p=1}^{L}\frac{1}{N}\left[\sum_{i=1}^{N}|H(t_i,f,d_p)|^2\right]\right), \end{aligned} \tag{3.3.3}$$

where $N = 10$ are the 10 snapshots at each frequency tone, $M = 1601$ are the 1601 frequency tones (frequency sweep points from 3.1 GHz to 10.6 GHz), L are the 8 distance points, and $H(t_i, f_j, d_p)$ is the channel transfer function at a certain frequency tone, distance, and a time snapshot. For analytical simplicity, the total distance dependent path loss exponent and frequency dependent path loss exponent for a human body is found by averaging the path loss factor (distance and frequency dependent) between the 9 individual body position and the UAV. Fig. 34 shows one such case of estimating distance dependent path loss exponent by linear regression for UWB radio channel between forehead and the UAV.

The distance dependent path loss factor n and frequency dependent path loss factor k thus determined for different carrier frequency corresponding to different bandwidths is listed in Table 5. The average value of n varied from 0.1 to 1.1. The general notion for the value of n is that it should be around 2 but since the indoor warehouse environment has metallic surface all around it that thus making the environment perfect for the coherent addition of multipath components at receiver. This in turn results in a small path loss factor values. Similar findings have also been reported in the previous research studies [107, 109].

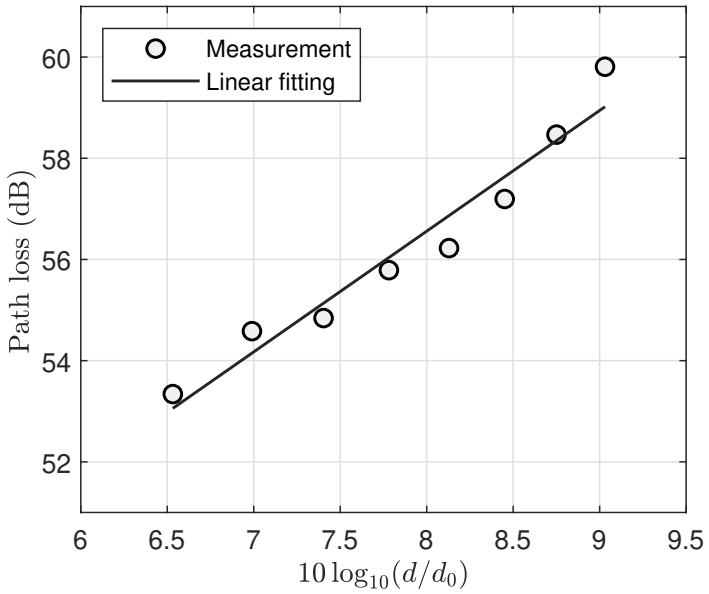

Figure 34: Linear fitting to determine the distance dependent path loss factor (n) between Forehead location of the human subject and UAV.

Table 5: Distance dependent path loss factor (n) and frequency path loss factor (k) for different bandwidths corresponding to various carrier frequencies (f_c) for UAV2W systems.

Factor	BW (GHz)	Carrier frequency (f_c)									
n	7.5	0.71									
	3.75	0.66	0.64								
	3	0.71	0.80	0.53							
	1.5	0.48	0.82	0.45	0.85	0.22					
	0.75	0.94	0.17	0.66	0.88	0.10	0.86	1.1	0.59	0.29	0.16
k	7.5	0.79									
	3.75	0.26	0.28								
	3	-0.2	1.71	-0.13							
	1.5	-1.3	1.90	1.82	0.59	-0.06					
	0.75	0.19	-1.92	2.35	0.05	3.25	0.87	1.98	-0.48	0	1.74

In contrast, the frequency dependent path loss component has a maximum value of 3.25 and minimum value of -1.92. This shows the frequency dependence of the UWB channel which separates it from the other normal channel models. One may question over the negative k value but on careful observation of Fig. 35 that plots the path gain over the entire spectrum of the UWB channel between Forehead and UAV. It can be observed that the overall trend for the value of k is positive, but for select bandwidths in the spectrum, the value will be negative as shown in the zoomed part of the figure. This is due to the antenna effects such as VSWR, which is frequency dependent (see [103] for detailed antenna specifications). Figs. 36 and 37 show such two cases of positive and negative k at different carrier frequencies corresponding to a given bandwidth in more detail.

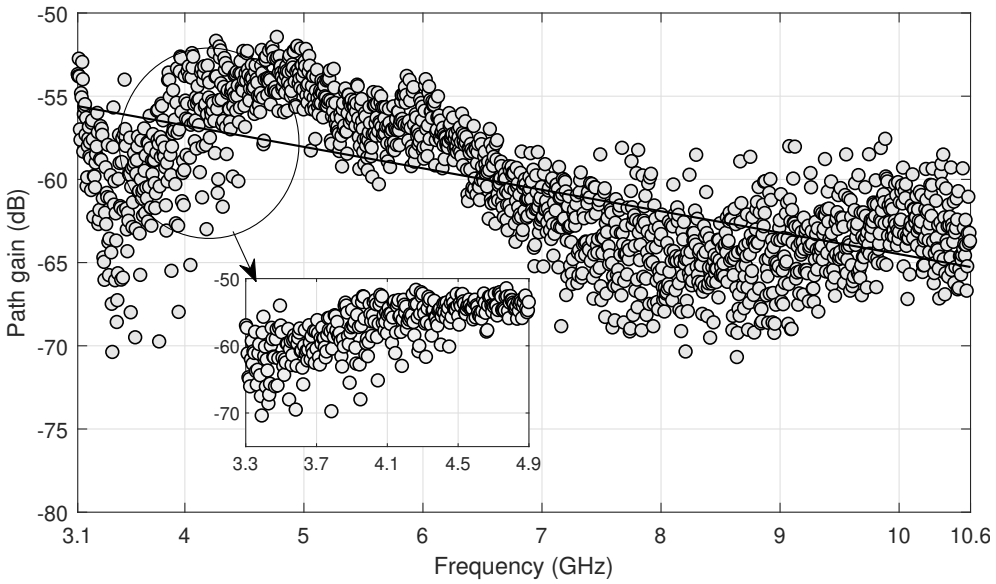

Figure 35: Frequency dependent path gain between Forehead and UAV.

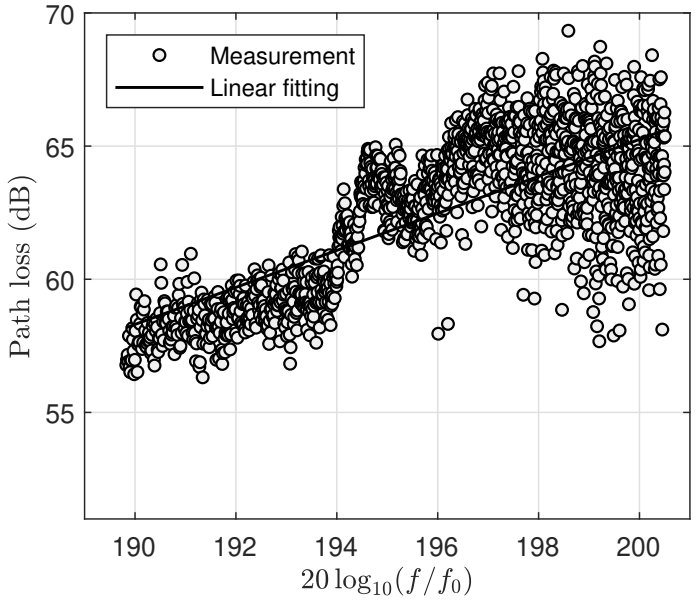

Figure 36: Linear fitting to determine k between Waist and UAV at bandwidth of 7.5 GHz and carrier frequency of 6.85 GHz.

Therefore, in UWB systems, not only the distance dependent path loss factor but also the frequency dependent path loss factor play a very important role in channel modeling that intrinsically depends on the selected bandwidth and the corresponding carrier frequency. This is a very crucial property to be considered while designing UAV2W systems or UWB systems in general. Now, in the next part, we will look into the time dispersion properties of UAV2W systems.

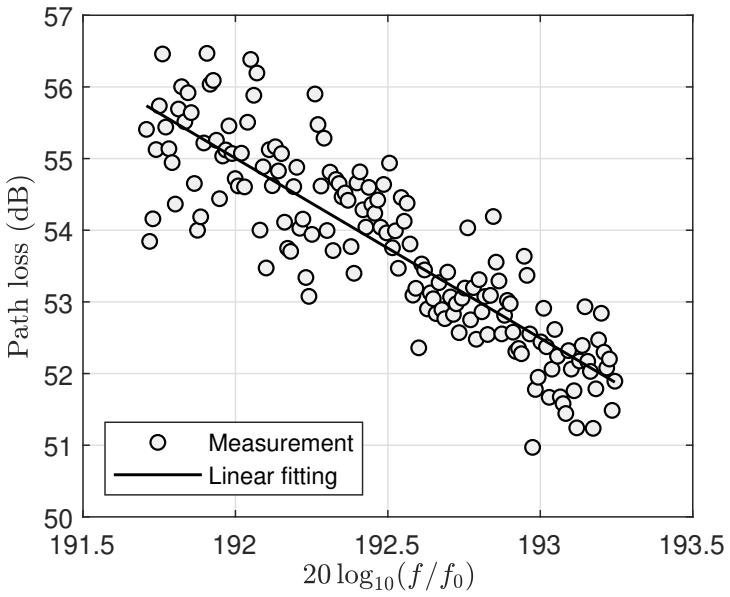

Figure 37: Linear fitting to determine k between Waist and UAV at bandwidth of 0.75 GHz and carrier frequency of 4.22 GHz.

3.3.2 Time Dispersion Analysis

Time dispersion parameters using the VNA method can be found using discrete time impulse responses. In this method, the multipath delay axis is described by bins that are equally spaced and the resolution of these time bins are determined by the measurement bandwidth. In our setup, the bandwidth was 7.5 GHz (3.1-10.6 GHz), therefore the bin width is 133.3 ps. All the multipath components within a bin are represented by a single multipath component delay. The relative delay between the first arriving path to the maximum resolvable path is known as maximum excess delay. The maximum resolvable path is given by $N\Delta\tau$, where $N = 1601$ is the maximum resolvable path and $\Delta\tau$ is the bin width. Hence, the maximum excess delay in our scenario is 213.47 ns, which can be easily seen in Fig. 38.

The measured channel modelled as a time-invariant channel impulse response [105, 107] is given as,

$$h(\tau) = \sum_{i=0}^{N-1} \alpha_i(\tau) e^{j\phi(\tau)} \delta(\tau - \tau_i), \tag{3.3.4}$$

where $\alpha_i(\tau)$, $\phi(\tau)$, τ_i are the amplitude, phase and excess delay of the i-th multipath component. From the recorded frequency domain VNA channel response, $H(f_i, d_l)$, the time domain response can be found by performing inverse Fourier transform (IFFT) which will yield $h(\tau, d_l)$. Therefore, the power delay profile (PDP) after the IFFT operation is given as,

$$P(\tau, d_l) = |h(\tau, d_l)|^2. \tag{3.3.5}$$

The time dispersion parameters such as root mean square delay, mean excess delay, and maximum excess delay depend on this PDP whose threshold in our analysis was set at -15

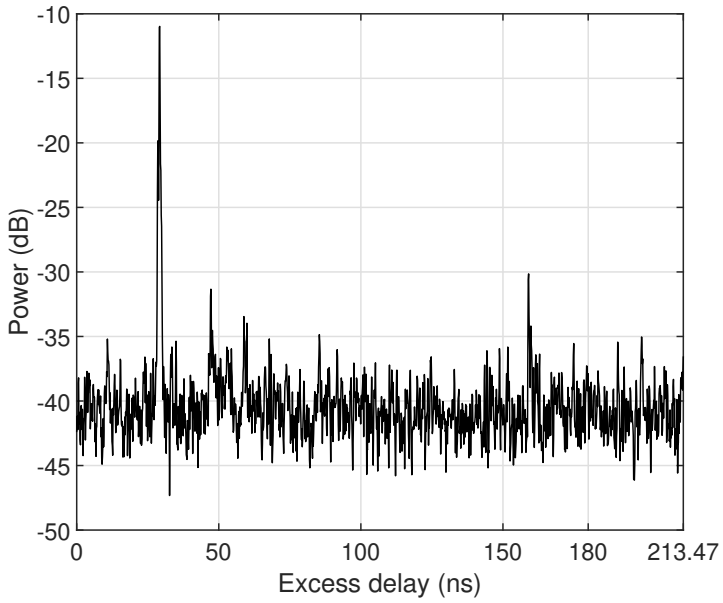

Figure 38: PDP at the distance of 8 m between Forehead and UAV.

dB. The mean excess delay is the first moment of power delay profile and is given as,

$$\bar{\tau} = \frac{\sum_{i=0}^{N-1} \tau_i P(\tau_i)}{\sum_{i=0}^{N-1} P(\tau_i)}. \tag{3.3.6}$$

Whereas the root mean square (RMS) delay spread is the second moment of PDP,

$$\sigma_t = \sqrt{(\tau^2 - \bar{\tau}^2)}, \tag{3.3.7}$$

where τ^2 is computed as,

$$\tau^2 = \frac{\sum_{i=0}^{N-1} \tau^2 P(\tau_i)}{\sum_{i=0}^{N-1} P(\tau_i)}. \tag{3.3.8}$$

Table 6 presents the average value for time dispersion parameters in the LOS warehouse environment[2]. The average value of RMS, mean excess delay and maximum excess delay for our measurement campaign was 55.37 ns, 57.50 ns and 41.07 ns. Although the typical values ranges from 20 ns to 40 ns but it highly depends on the measurement environment, and the set PDP threshold [107]. In our analysis, this threshold was kept at -15 dB. Fig. 39 shows the comparison of maximum excess, mean excess and RMS delay in the case of LOS scenario for the case of Forehead. It can be intuitively observed that as the distance between Tx and Rx increase, so does the RMS, maximum excess and mean excess delays. Till now, we examined the path gain and time dispersion properties for UAV2W systems at UWB frequency. The other part is to model the fading in such systems at UWB frequency. In the next section, we will examine this fading and statistically model the fading for UAV2W systems at UWB frequencies.

[2]Note that no non-LOS measurements has been considered in this study.

Table 6: Delay analysis for 9 body locations in case of LOS scenario.

Position	RMS delay (ns)	Mean excess delay (ns)	Maximum excess delay (ns)
Ear	52.82	50.60	23.13
Forehead	46.26	42.77	22.80
Chest	57.17	59.19	27.05
Right Arm	58.83	63.05	24.75
Right Wrist	57.07	62.83	55.63
Waist	60.67	71.1	111.25
Right Thigh	55.31	55.64	39.56
Right Lower Shin	56.37	58.45	40.54
Abdomen	53.83	53.85	24.95
Average	**55.37**	**57.50**	**41.07**

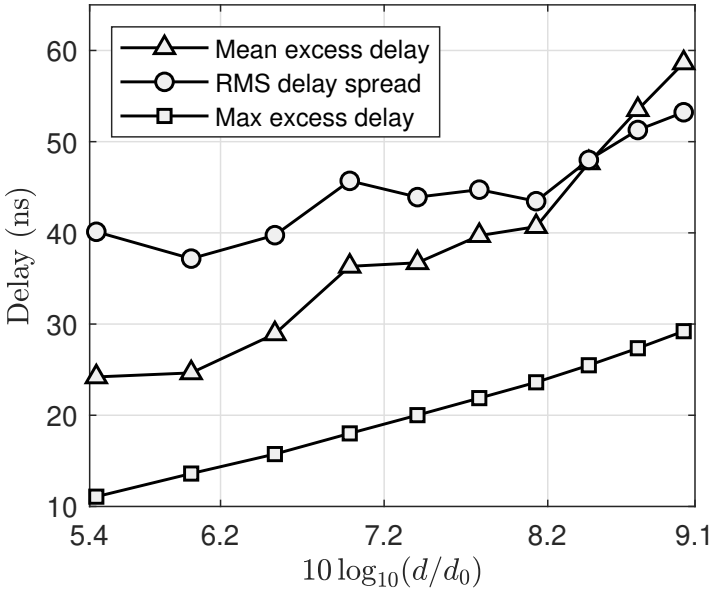

Figure 39: Mean excess, maximum excess and RMS delay comparisons with different log distances for antenna located at forehead and PDP threshold set at -15 dB.

3.3.3 Statistical Modeling of Channel Fading

There has been lot of UWB measurement campaigns, where the large scale fading statistics are categorized into one of the fading distributions such as, Rayleigh, Weibull or Log-normal etc. In our study, as a commonly used model selection test, second order Akaike information criterion (AIC) is used to determine the best fit distribution among these popular distributions [110, 111]. The reason that the second order was chosen is to take care of the different number of parameters in these distributions. For instance, Rayleigh and Exponential are single parameter (rate) distributions, while Weibull has two parameters (shape and scale). Mathematically, this second order AIC is given as [37],

$$\mathrm{AIC}_c = -2\ln L + 2k + \frac{2k(k+1)}{n-k-1}, \tag{3.3.9}$$

where L is the maximized likelihood, k is the number of parameters estimated for that distribution, and n is the number of samples of the experiment. The relative corrected AIC is given as [37],

$$\Delta = \mathrm{AIC}_c - \min(\mathrm{AIC}_c), \tag{3.3.10}$$

which implies that zero value will indicate the best fit.

The goodness of fit is compared for Normal, Weibull, Log-normal, Rayleigh, Nakagami, Rician, Gamma, and Exponential distributions to find the best fit as shown in Table 7.

Table 7: Comparison of different distributions adopting AIC for nine off-body positions in the indoor environment.

Position	Normal	Weibull	Log-normal	Rayleigh	Nakagami	Rician	Gamma	Exponential
Forehead	10.67	225.97	0.43	5730.87	5.73	10.66	2.47	7935.29
Heart	0.24	46.42	11.34	4501.36	0.91	0.23	5.31	6687.54
Right Wrist	53.22	0.60	104.91	4601.43	67.53	53.31	85.14	6789.21
Abdomen	37.37	4.07	78.53	4732.99	48.44	37.42	62.56	6923.94
Right Thigh	12.58	92.02	35.52	5147.59	18.03	12.60	25.83	7345.34
Right Arm	13.21	38.85	44.98	5838.16	22.32	13.24	32.89	8043.56
Right Shin	15.94	12.95	49.43	4859.50	24.64	15.98	36.16	7052.96
Waist	12.50	163.40	18.84	6019.61	13.29	12.51	15.51	8225.92
Ear	7.61	172.47	16.67	5692.66	9.01	7.61	12.06	7896.93

Based on the results listed in Table 7, and plots from Fig. 40, the minimum values correspond to Log-normal distribution. Thus, the Log-normal distribution can be easily concluded to be the best fit distribution. It is also important to note that these distributions can be easily transformed to other distributions.

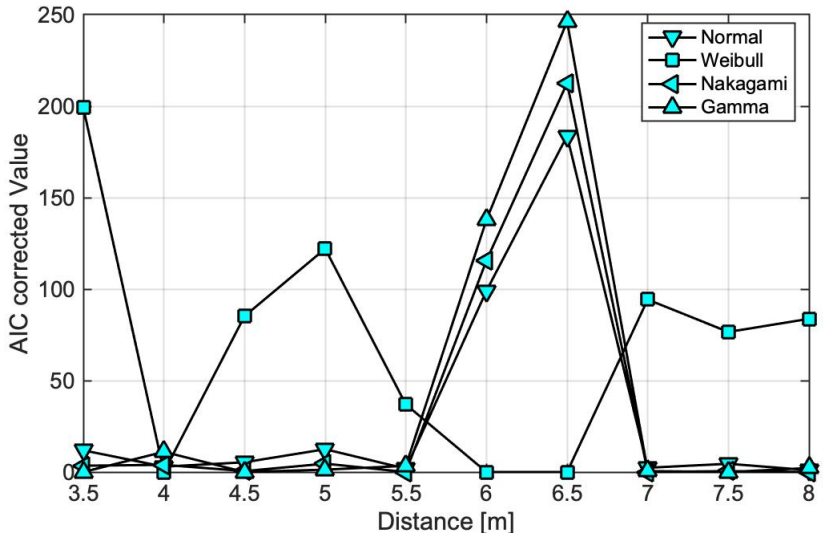

Figure 40: AIC test for goodness of fit with different distributions at different distances between the UAV and Forehead position of the human subject.

The PDF and CDF of a Log-normal distribution is given as,

$$f_X(x) = \frac{1}{\sqrt{2\pi}x\sigma} e^{-\frac{(\ln(x)-\mu)^2}{2\sigma^2}},$$
$$F_X(x) = \frac{1}{2}\text{erfc}\left(-\frac{\ln(x)-\mu}{\sqrt{2}\sigma}\right), \tag{3.3.11}$$

where μ and σ are the mean and standard deviation of the Log-normal of a random variable x and erfc(z) is a complementary error function. Using the estimated Log-normal distribution, the cumulative distribution functions (CDF) at two distances of 5 and 7.5 m are compared with the empirical CDFs (Fig. 41), which shows the close matches with each other. Similar results can be seen at other distances in our study. This confirms the hypothesis that the channel fading statistics for UAV2W systems at UWB frequencies is given by a Log-normal distribution. Similar conclusions were also drawn in [98, 99].

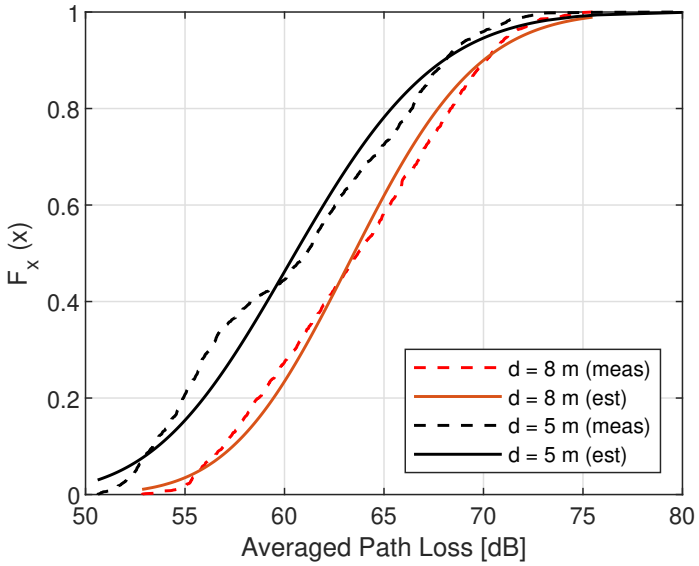

Figure 41: Measured and estimated CDF for Forehead off-body radio channel in an indoor environment with the distance between human subject and UAV at 5 and 8 m.

3.4 Conclusions

In this chapter, we examined the UAV2W systems at UWB frequencies, and characterized the channel in terms of path-gain, time dispersion, and fading statistics. The overall conclusion and contribution of this chapter can be enumerated as,

1. This measurement study is one of the first studies to characterize UAV2W channels considering on-body measurements at UWB frequencies.

2. Distance dependent and frequency dependent path loss factor for different bandwidth with corresponding carrier frequency is studied, and determined in detail.

3. Time dispersion properties such as root mean square delay, mean excess delay and maximum excess delay in UAV2W systems is evaluated and found for different body locations.

4. Statistical analysis of channel fading shows that the Log-normal distribution is the best fit distribution for large scale fading statistics. This was confirmed by Akaike Information Criterion.

In the next chapter, we will look into another high frequency technology, known as millimeter wave (mmWave). The frequency range at mmWave is in the range of 28 GHz- 77 GHz. We will characterize and statistically analyze this millimeter wave channel for UAV-assisted communications in the next chapter, and present a novel emulation set-up at 28 GHz. This will be again an empirical study but based on a novel emulation technique.

CHAPTER IV

MILLIMETER WAVE CHANNEL MODELING IN UAV-ASSISTED COMMUNICATION SYSTEMS

4.1 Introduction

This chapter will focus on a higher frequency spectrum than the UWB discussed in the previous chapter, this spectrum is also known as mmWave spectrum. Until now, we saw the case of spectrum optimization by exploiting interference threshold in spectrum sharing networks or cognitive radio networks, and moved to a higher frequency spectrum of ultra-wide band in the last chapter. The main reason behind this move towards high frequency in the spectrum rather than just optimizing the available sub 6 GHz spectrum is that the demand continues to outpace the available resource in the frequency spectrum. Also, the rapid proliferation of the smart devices/users below 6 GHz create massive amount of data traffic, and thereby burden the already congested frequency spectrum. To overcome this spectrum crunch, technologies such as cognitive radios [112], multiple-input and multiple-output (MIMO) [113], and non-orthogonal multiple access (NOMA) [114] etc. were proposed but not much can be done to cater this every rising demand for high data rates. In 2015, the Federal Communications Commission (FCC) released mmWave frequencies for licensed and unlicensed use. The newly licensed frequencies are 28 GHz, 37 GHz, and 39 GHz, while the unlicensed bands are, 64$\sim$71 GHz [44]. At these high frequencies with high bandwidth, not only multi-gigabit wireless communication is possible but also small antenna size, and circuits (millimeter wavelengths) makes it very promising.

On the other hand, UAVs have seen a lot of interest from academia, industry, and from the general public at large over the past decade. The main reasons behind this large scale popularity are the ease of operability (remote or autonomous), easy deployment, higher maneuverability, and lower operating and maintenance costs of UAVs. UAVs are now extensively used in smart farming, disaster responses, military, smart logistics, and recreation (filming) [23, 115–118]. Advancements in UAV technology are also fuelling the interest of its application in wireless communication technology. UAVs are capable of providing a highly reliable and cost effective mode of technology [23–27], and can also be easily deployed as a flying base station (BS) to provide ubiquitous wireless communication access. They also provide an alternative support for 5G and B5G cellular mobile communication. Furthermore, UAVs can be used as mobile relays to provide wireless connectivity among partitioned user equipment (UE) that lack any direct line of sight (LOS) communication between the BS and UE. Apart from using as a flying BS and/or relaying node, UAVs have also found application in areas such as aerial data collectors, aerial caching, and aerial power source etc. Multiple UAVs can also coordinate, and self organise to form different network architectures, such

as flying adhoc networks (FANETs), internet of drones etc. All these applications of UAV-assisted wireless communication have been studied assuming Wi-Fi, or at fourth generation (4G) cellular communication frequencies. Lately, mmWave communication with UAVs have been a topic of great interest [23, 49, 119].

Recent studies [23, 42, 45, 49, 119, 120] suggest that the successful deployment of UAV-assisted mmWave wireless communication hinges on accurate and realistic propagation channel modeling. While considerable research on terrestrial propagation channels has been conducted for the last few decades, propagation channel modeling for UAVs has not been extensively studied [49]. Existing channel modeling studies mainly use 1) analytical modeling, e.g., two-ray model, or 2) ray-tracing simulations, or 3) empirical modeling using channel sounding methods. The first two methods are deterministic, cost-effective and require less effort, but they are fundamentally sub-optimal approaches given the complexity and dynamicity of the wireless channels. On the other hand, empirical modeling that uses the channel sounding method could provide more realistic channel models but requires a large amount of field data that needs to be collected from multiple channel observations, and numerous measurement campaigns. Moreover, microwave measurements to validate such models are inadequate because of fundamental differences between mmWave and microwave channels (e.g., propagation loss, directivity, sensitivity to blockage).

Besides that the UAV operation in itself introduces many unique atmospheric and terrain challenges [49]. Due to UAV restrictions (e.g., pointing, payload, power, equipment-cost constraints) and the requirement of advanced channel-sounding equipment; to our knowledge no studies have been reported that conduct empirical modeling for UAV-assisted mmWave channels. It is also important to note that the propagation channel models determined or utilized for higher altitude aeronautical communications generally cannot be generalized directly for low altitude (small) UAV-assisted mmWave communications [49]. There are distinct structural and flight characteristics that needs to be considered for low lying UAVs, such as different airframe shadowing characteristics , and potentially sharper pitch, roll, and yaw rates of change during flight. Empirical data is therefore required to determine accurate analytic and stochastic models of mmWave wireless channels.

Utilization of a robotic arm to emulate UAV motion can help overcome these challenges by, 1) efficiently emulating the motion of UAV in different environments/scenarios, and 2) enabling rapid collection of channel measurements by using channel sounding method to create a database for UAV-assisted mmWave channel models. In this chapter, a novel way to incorporate UAV motion to study UAV-assisted mmWave communication is presented by a robotic arm that emulates the actual UAV in an anechoic chamber. This method, as compared to other studies captures the real UAV dynamics and the atmospheric conditions for the UAV. This is a very important first step in realizing a real mmWave communication system for UAVs in the near future. Designing a channel emulator by using vector network analyzer (VNA) based channel sounder with real UAV motion emulated by a robotic arm is a first-of-its-kind, experimental, wireless channel emulator for such UAV-assisted mmWave communications that can produce accurate and realistic propagation channel models for a wide range of environments and scenarios. Using the robotic arm to produce atmospheric turbulence effects on UAV position and stability, we can produce the first empirical mmWave channel models that account for path loss, and Doppler spread due to UAV motion.

Before, moving on to the measurement setup in the next section, it is very impor-

tant to understand the different challenges associated with the mmWave communication. mmWave communication suffers extensively from the propagation attenuation, shadowing effect (blocking), beam misalignment, and Doppler shift [45–48] because of its small wavelength, which is in the order of millimeters. Doppler spread effect is the most critical one, especially when there is a motion attributed to the movement of transmitter (Tx) or receiver (Rx) or both. In addition to that, with the wind gusts in the atmosphere for UAVs, Doppler effects become more aggravated. It is also well known that in a given mobile and multipath environment, each multipath component (MPC) will experience a different Doppler shift according to the motion. This leads to the spectral broadening at the receiver that causes erroneous signal reception or communication failure. Therefore, modeling physical UAV motion as close to actual UAV motion is very crucial in understanding the design constraints, and performance of a mmWave based UAV communication system. Techniques to analyze and combat the Doppler effects have been studied earlier but as mentioned previously, almost all of them are based on simulations that ignore the actual UAV motion dynamics and the wind gust conditions in the atmosphere [23, 26, 49]. Therefore, in this chapter, the focus will be to analyze and study the Doppler and path loss characteristics of mmWave channel by emulating the real UAV motion under wind gusts in an anechoic chamber, and in the later part of the chapter, we will examine the effect of propeller on these UAV-assisted mmWave communication systems. These propeller effects are studied with an actual UAV (hexcopter) in an outdoor environment. In short, the scope of this chapter is,

- to analyze Doppler spread of mmWave communication system by emulating UAV motion under the Dryden wind conditions in an anechoic chamber.
- to examine the phase change effects caused by motion artifacts in VNA based measurements, and de-embed the phase variations caused by the cable movement from collected data.
- to determine the path loss exponent value under these anechoic chamber settings [1].
- to study and validate the propeller effects on mmWave communication system with actual UAV.

This chapter is organized as follows, Section 4.2 discusses the measurement setup and in Section 4.3, details of the UAV motion emulation is discussed. Analysis of Doppler spread and path loss modeling are presented in Section 4.6, and propeller effects are studied and examined in Section 4.7 . Finally, conclusions are drawn in Section 4.8.

4.2 Measurement Setup

The successful deployment of wireless communication systems requires a solid understanding and accurate modeling of wireless channel conditions (propagation characteristics) between the transmitter (Tx) and receiver (Rx). Channel sounding is a measurement technique used to gain that understanding. The channel sounding measurement method used in this study is

[1] It is important to note that these results cannot be generalized as such for any indoor or outdoor environments, and will require extensive data measurement campaigns in that regards.

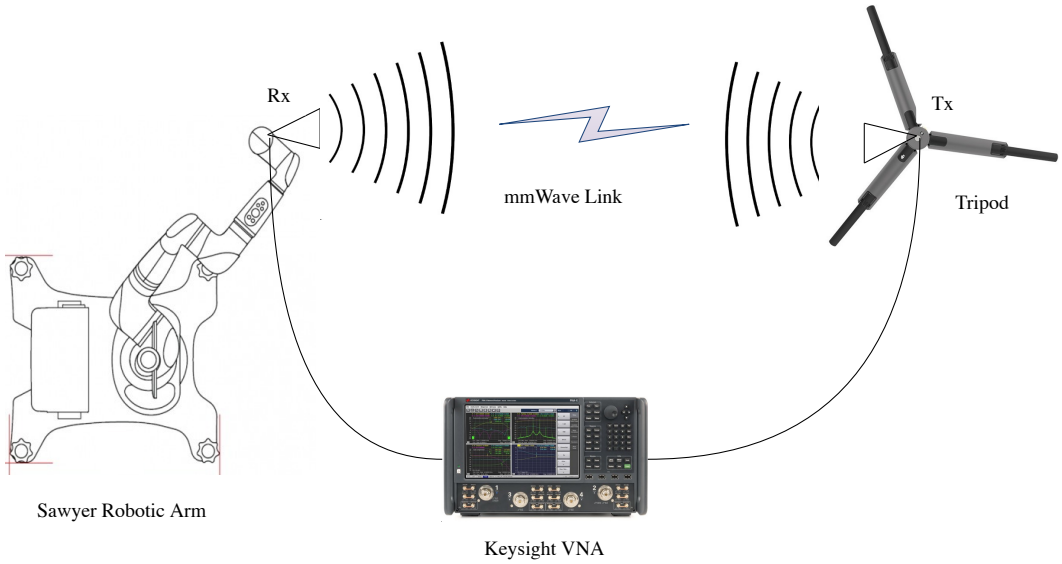

Figure 42: Top view of the measurement setup. The receiver is placed on the robotic arm and connected to VNA by a phase stable short cable, while the transmitter is hooked on the tripod with a long cable.

based on continuous wave (CW) mode of VNA [121,122]. In this mode, instead of a frequency sweep, only one frequency tone is set and the sweep is done in time domain by setting the number of points in the time sweep domain. The frequency tone in our experiment is set at 28 GHz, and 4096 points are selected for time sweep with an intermediate frequency set at 300 Hz. The Rx is hooked up on the robotic arm, while the Tx is placed on a tripod. The Tx is positioned at different distances from the Rx (3.5 ft to 23.5 ft) in increments of 2 feet for this measurements plan. The Tx is connected at port-1 of the VNA, while the Rx is connected at port-2. At each distance point (11 points in total, three samples of S21 parameters are recorded on the VNA. These multiple samples of S21 parameters are recorded to get a better redundant value for the Doppler spectrum, and for the channel path loss modeling. The measurement setup is shown in the Fig. 42 with the details of all the measurement equipment is listed in Table 8.

Table 8: The measurement equipment with the specifications.

Equipment	**Specifications**
Vector Network Analyzer	Keysight PNA-X (N5247A), 10 MHz to 67 GHz
Antenna (horn type)	Cernexwave (CRA28264015), 26.5 GHz-40 GHz, Gain: 15 dBi, HPBW:18°
Waveguide transition	Cernexwave (CWK28264003F), WR-28, Brass/Copper
Cables	Fairview microwave (50 feet), Mini-Circuits (5 feet)
Robotic arm	Rethink Robotics (Sawyer), Software: Intera, 1 arm x 7 degree of freedom

This IF frequency of 300 Hz is selected to accommodate the expected Doppler frequency

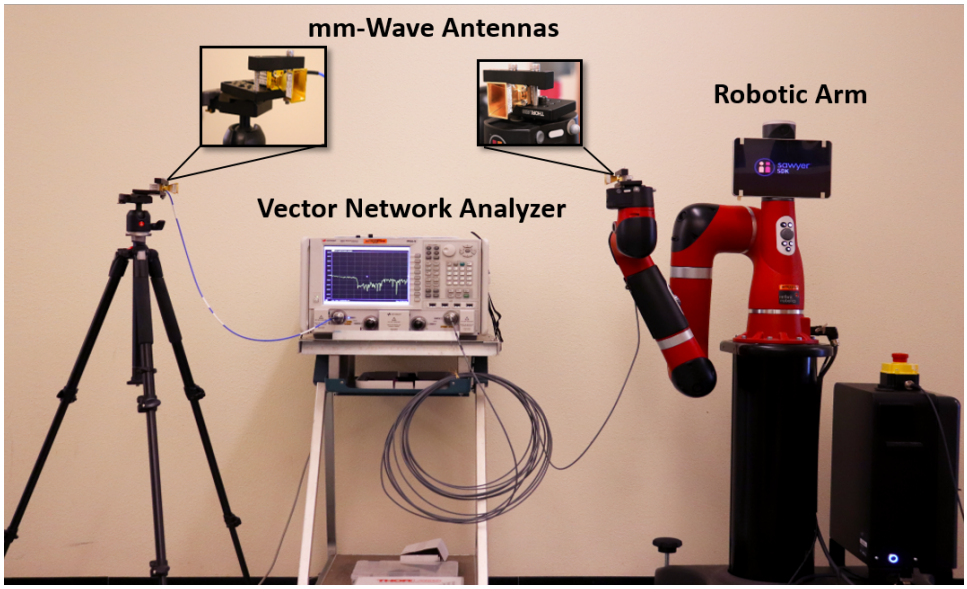

Figure 43: Equipment used in the measurement setup .

within the frequency range on the VNA. It is also important to mention that increasing the

Figure 44: The actual setup in an anechoic chamber.

IF bandwidth will definitely decrease the time required to capture the data, however, the scattering parameter data will suffer from higher noise as the noise floor level is linearly proportional to the IF bandwidth. Therefore, taking multiple readings with moderate IF bandwidth is recommended in this measurement scenario. With the 4096 sample points, the sampling time is, $Ts = 4.4$ ms.Thus, the Doppler range that could be captured with these settings will be in the range of $-fs/2 = -114.49$ Hz to $+fs/2 = +114.49$ Hz. Fig. 43 and Fig. 44 shows the equipment's, and the actual measurement set-up in an anechoic chamber.

The Tx is initially at a height of 4 feet 4 inches (at the beginning point) on a tripod, while the Rx is at the height of 4 feet 6 inches on the robotic arm. The robotic arm is connected to a computer that executes a Python script to emulate the UAV motion with the

wind turbulence model discussed in detail in later subsections. The corresponding scattering parameter data generated under such motion is captured on the VNA, and analyzed on a workstation later on. In the next section, we will dwell more into the details on the UAV motion emulation part with the robotic arm.

4.3 UAV Motion and Its Emulation

In UAVs or in fact, in any flying plane, the stability and control is very complex as compared to cars, buses or boats. The cars and buses can move in two dimension whereas the UAV/planes can move in three dimensions of roll, yaw and pitch. The rotation around the front to back is known as roll and rotation around side-by-side is called pitch. On the other hand, rotation around the vertical is known as yaw. The complexity arises because any change in one of these dimension affects the other two dimensions. Thus, in a UAV with mmWave antenna on it, any displacement across one axis will affect the other two. As it is well known that the UAVs are affected by the wind gusts in the atmosphere that can change their rotation along any of these axis. The pitch and yaw will cause orientation changes in the antenna in addition to beam pointing displacement. These orientation changes may result in polarization effects, that will affect the received power and Doppler consequently.

To create such kind of a scenario and to study or analyze the wireless channel characteristics, such as Doppler and path loss with an actual UAV is not only infeasible but also impractical with any present day channel sounding technique. Emulation can be a viable option to study the mmWave channel characteristics in a UAV-assisted wireless communication system while considering these effects. Therefore, to emulate such a real UAV motion under wind turbulence is a very challenging but also an interesting problem. This problem can be solved by using methods from robotics area, where the actual UAV motion with the wind turbulence can be easily emulated by a robotic arm. The motion of this robotic arm is controlled by robotic operating system (ROS) from a computer and to create the turbulence experienced by UAVs in atmosphere, a wind generation model is used. The UAV motion is first simulated in MATLAB® using a stochastic wind gust model (Dryden wind model) and a 6 degree-of-freedom (DOF) quadcopter dynamic model together with closed-loop controllers are used for hovering motion models. Then, the positions and altitude of the quadcopter generated from the simulations are emulated by the end-effector (end point) of the robotic arm. The simulation framework and the arm control is discussed in the following subsections.

4.3.1 Simulation of Quadcopter Motion with Wind

In this subsection, we will look into the case of simulating Quadcopter in generic atmospheric conditions. To consider such scenario, Dryden wind turbulence model [123, 124], which is commonly used for aircraft designs and in building simulation applications is used. This popular Dryden model has been extensively used for mall fixed-wing UAVs (see e.g., [125]. This model is based on a stochastic formulation that incorporates knowledge of the energy spectrum of turbulence [126] and assumes a homogeneous frozen spatial turbulence. Therefore, we model the wind as a combination of a 3D mean wind $(\bar{u}, \bar{v}, \bar{w})^\top$ and a 3D turbulence wind $(u, v, w)^\top$. The mean wind is specified in the north-east-down (NED) coordinates, while

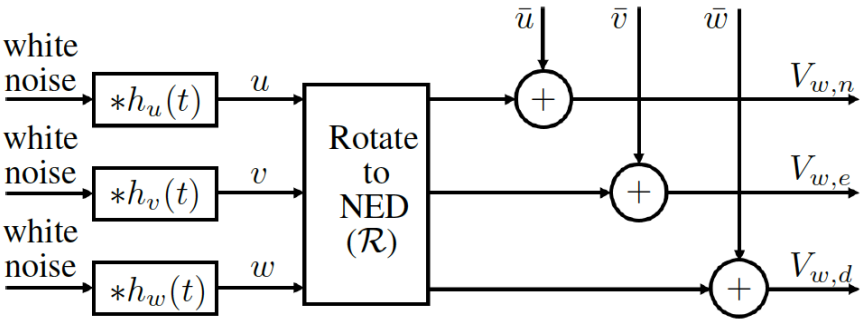

Figure 45: The Dryden wind is generated by combining the mean wind $(\bar{u}, \bar{v}, \bar{w})^\top$ and the turbulence wind $(u, v, w)^\top$. $*h_\star(t)$ denotes the convolution with the impulse response of $H_\star(s)$ in (4.3.1)–(4.3.3), where $\star = u, v, w$.

the turbulence wind is specified in another different frame (discussed later). The Dryden turbulence model is implemented through filtering operations on white noise signals.

Let the 3D turbulence velocity be $(u, v, w)^\top \in \mathbb{R}^3$. The u component is aligned with the direction of the horizontal mean wind, i.e., $(\bar{u}, \bar{v}, 0)$, the w component is aligned with the vertical (down) direction, and the v component is aligned with the direction that completes a right-handed coordinate frame with the v and w directions. As shown in Fig. 45, the 3D velocities u, v, and w in time domain are obtained by passing three independent white noise signals through three filters described by the following transfer functions [125, Section 4.4].

$$H_u(s) = \sigma_u \sqrt{\frac{2V_{a0}}{L_u}} \frac{1}{(s + \frac{V_{a0}}{L_u})}, \tag{4.3.1}$$

$$H_v(s) = \sigma_v \sqrt{\frac{3V_{a0}}{L_v}} \frac{(s + \frac{V_{a0}}{\sqrt{3}L_v})}{(s + \frac{V_{a0}}{L_v})^2}, \tag{4.3.2}$$

$$H_w(s) = \sigma_w \sqrt{\frac{3V_{a0}}{L_w}} \frac{(s + \frac{V_{a0}}{\sqrt{3}L_w})}{(s + \frac{V_{a0}}{L_w})^2}, \tag{4.3.3}$$

respectively, where $(\sigma_u^2, \sigma_v^2, \sigma_w^2)$ are the variances of the turbulence, V_{a0} is an estimate of the quadrotor's airspeed, and (L_u, L_v, L_w) are the turbulence length scales. In our experiments, we focus on horizontal, low turbulence effects and set $\sigma_u^2 = 0.53$, $\sigma_v^2 = 0.53$, and $\sigma_w^2 = 0$. For low altitude, L_w is set to the altitude in feet.

In our experiments, we set (L_u, L_v, L_w) to be $(200, 200, 50)$ ft. Since the quadcopter is controlled in the hover mode, we set V_{a0} to be the mean wind speed, i.e., $\sqrt{\bar{u}^2 + \bar{v}^2 + \bar{w}^2}$, where $\bar{u} = 2$ m/s, $\bar{v} = -1$ m/s, and $\bar{w} = 0$ m/s. The output of the three filters is a time-series representation of the turbulence, which is further combined with the non-zero mean wind $(\bar{u}, \bar{v}, \bar{w})^\top \in \mathbb{R}^3$. The resulting 3D wind in the NED frame is given by

$$V_w(t) = (\bar{u}, \bar{v}, \bar{w})^\top + \mathcal{R}(u(t), v(t), w(t))^\top, \tag{4.3.4}$$

where $\mathcal{R} \in \mathbb{R}^{3\times3}$ is a 3D rotational matrix that converts $(u(t), v(t), w(t))^\top$ to the NED frame. The process of generating the Dryden wind is shown in Fig. 45.

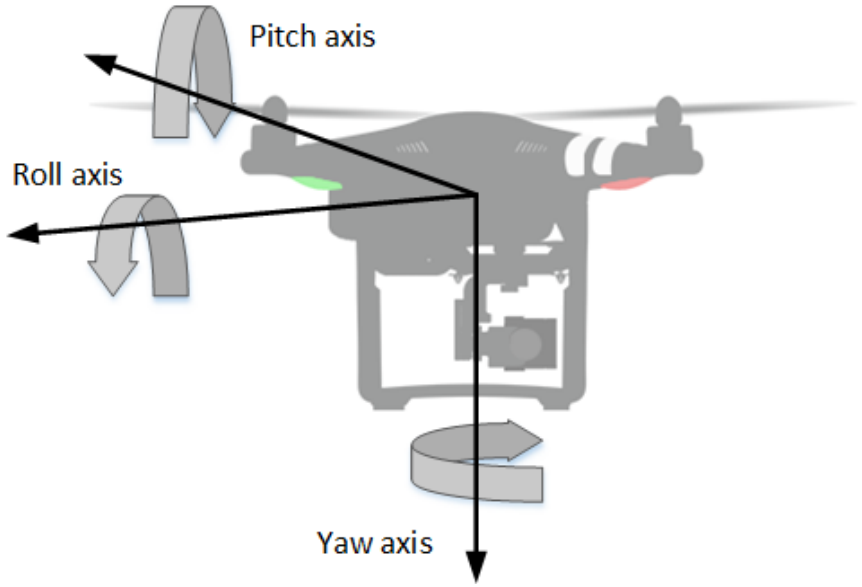

Figure 46: Pitch, roll and yaw axis of a UAV.

Standard formulation of the quadcopter dynamics [127], with the addition of a nonlinear drag term $f_d \in \mathbb{R}^3$ is used to model the wind effect. The dynamics of the quadcopter is given by,

$$\begin{bmatrix} \ddot{p}_n \\ \ddot{p}_e \\ \ddot{p}_d \\ \dot{\phi} \\ \dot{\theta} \\ \dot{\psi} \\ \dot{\omega}_p \\ \dot{\omega}_q \\ \dot{\omega}_r \end{bmatrix} = \begin{bmatrix} (-\cos\phi\sin\theta\cos\psi - \sin\phi\sin\psi)\frac{F}{m} + \frac{f_{d,n}}{m} \\ (-\cos\phi\sin\theta\sin\psi + \sin\phi\cos\psi)\frac{F}{m} + \frac{f_{d,e}}{m} \\ g - (\cos\phi\cos\theta)\frac{F}{m} + \frac{f_{d,d}}{m} \\ \omega_p + \sin\phi\tan\theta\,\omega_q + \cos\phi\tan\theta\,\omega_r \\ \cos\phi\,\omega_q - \sin\phi\,\omega_r \\ \frac{\sin\phi}{\cos\theta}\,\omega_q + \frac{\cos\phi}{\cos\theta}\,\omega_r \\ \frac{J_y - J_z}{J_x}\omega_q\omega_r + \frac{1}{J_x}\tau_\phi \\ \frac{J_z - J_x}{J_y}\omega_p\omega_r\dot{\psi} + \frac{1}{J_y}\tau_\theta \\ \frac{J_x - J_y}{J_z}\omega_p\omega_q + \frac{1}{J_z}\tau_\psi \end{bmatrix}, \tag{4.3.5}$$

where m and (J_x, J_y, J_z) are the mass and the moment of inertia of the quadcopter, respectively, (p_n, p_e, p_d) are the north, east, and down positions in the inertial frame, (ϕ, θ, ψ) are the roll, pitch, and yaw angles, respectively, $(\omega_p, \omega_q, \omega_r)$ is the angular velocity in the body frame, $(F, \tau_\phi, \tau_\theta, \tau_\psi)$ are the force and the moments in the designated directions, and $f_d = (f_{d,n}, f_{d,e}, f_{d,d})^T$ is the drag force in the north, east and down directions. The pitch, roll, and yaw axis for this quadcopter are also shown in Fig. 46. The drag force f_d is modeled in a quadratic form as $f_d = C_d(V_w - \dot{p})|V_w - \dot{p}|$, where $\dot{p}$ is the ground velocity of the quadcopter equal to $(\dot{p}_n, \dot{p}_e, \dot{p}_d)$ and C_d is a drag coefficient matrix. In the quadcopter dynamics used in this chapter, motor dynamics and several secondary aerodynamic effects, such as blade flapping and air-relative velocity effects are included. Closed-loop PID

(Proportional-Integral-Derivative) Controllers are designed to achieve tracking of a given waypoint. Interested readers are referred to [128, 129] for more details on the quadcopter dynamics and the controller design.

4.3.2 Emulation of Quadcopter Motion using the Sawyer Robotic Arm

The MATLAB simulator generates NED positions, and the yaw, pitch, roll (YPR) orientations, as well as their time derivatives, at a rate of 10 Hz. These state variables are formatted and dumped to a raw text file. A Python program reads these NED and YPR coordinates and uses them to generate a series of time-dependent waypoints for the Sawyer robotic arm. The Intera software development kit (SDK) is used as an interface between the desired waypoints and the ROS messages needed to command the Sawyer robotic arm. For this application, the Intera Motion Controller Interface is implemented in a joint control mode. This mode generates trajectories based on a series of joint commands, and the native inverse kinematics solver is used to convert waypoints from the end-effector frame to a given set of joint positions.

4.3.3 Emulation of Linear Motion using the Sawyer Robotic Arm

The MATLAB software is used to generate the waypoints from the Dryden motion generation profile. In order to precisely control the velocity, the Joint Velocity Control mode was implemented in the Intera SDK. This contol mode accepts velocity commands in the joint frames, not the end-effector frame, and as such the Jacobian matrix $J(\theta_1, \theta_2, ..., \theta_7)$ is needed to translate commanded velocities between frames. Specifically, the psuedo-inverse Jacobian matrix is needed to convert velocities from the end-effector frame to the joint frames as follows,

$$J(\theta_1, \theta_2, ..., \theta_7) = \begin{bmatrix} \frac{\partial x}{\partial \theta_1} & \frac{\partial x}{\partial \theta_2} & \cdots & \frac{\partial x}{\partial \theta_7} \\ \frac{\partial y}{\partial \theta_1} & \frac{\partial y}{\partial \theta_2} & \cdots & \frac{\partial y}{\partial \theta_7} \\ \frac{\partial z}{\partial \theta_1} & \frac{\partial z}{\partial \theta_2} & \cdots & \frac{\partial z}{\partial \theta_7} \\ \frac{\partial \phi}{\partial \theta_1} & \frac{\partial \phi}{\partial \theta_2} & \cdots & \frac{\partial \phi}{\partial \theta_7} \\ \frac{\partial \theta}{\partial \theta_1} & \frac{\partial \theta}{\partial \theta_2} & \cdots & \frac{\partial \theta}{\partial \theta_7} \\ \frac{\partial \psi}{\partial \theta_1} & \frac{\partial \psi}{\partial \theta_2} & \cdots & \frac{\partial \psi}{\partial \theta_7} \end{bmatrix}, \tag{4.3.6}$$

$$Q = J^{-1}V, \tag{4.3.7}$$

where J^{-1} is a 7×6 matrix representing the psuedo-inverse of the Jacobian, V is a 6×1 matrix representing the linear and angular velocities of the end-effector, and Q is a 7×1 matrix representing the joint velocities.

This method provides precise control of the arm's velocity at speeds under 0.5 m/s. However, drift was introduced in the x-axis as the arm reached higher speeds and the end-effector reached its outer boundaries. As such, a P (proportional) controller was used to minimize

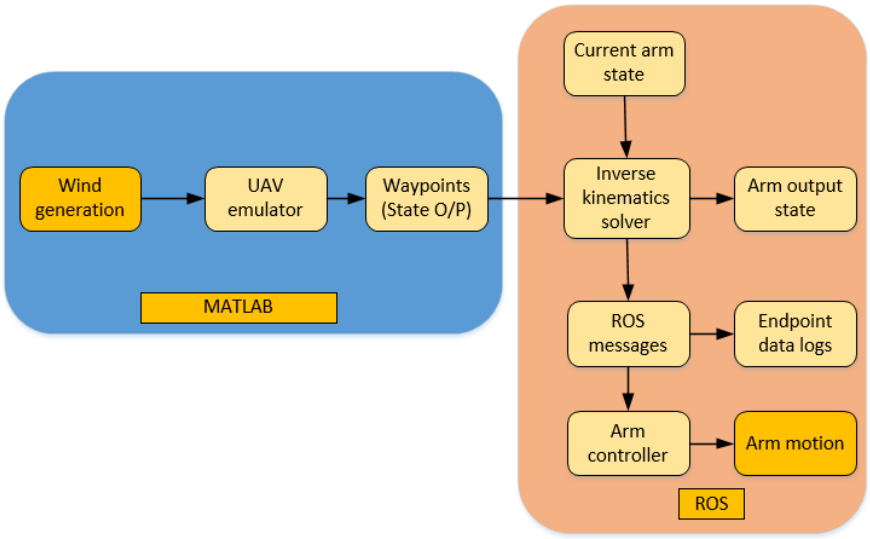

Figure 47: Arm motion dynamics.

the drift along the x-axis. This whole UAV motion emulation dynamics[2] is summarized in Fig. 47. An actual snapshot of the UAV motion can also be visualized in this GitHub repository[3]. Once the robotic arm is emulating the real UAV motion under turbulence, the next step is to measure scattering parameters from the VNA to characterize the mmWave channel in UAv assited communication setup.

4.3.4 Challenges with VNA Based Measurements

At this point, the robotic arm is programmed to emulate the UAV motion, and for the setup, the antenna is mounted on the arm, with IF cable connecting it to the VNA at port-1. On the other end, second IF cable connects the other antenna to VNA. During the measurement, the cable connected to the arm will experience displacements as the robotic arm moves while emulating the UAV motion, thus creating phase changes in the measured scattering parameter data. This will result in wrong Doppler results as Doppler depends on the phase change over time. One such example is shown in Fig. 48 which shows the phase changes at port-2 of VNA during one sample measurement conducted in an indoor environment. Once can see the deviation of 273° in phase with minimum at -153.01° and maximum of 120.14° with mean staying at 65.5°.

To take care of these motion artifacts at high frequency measurements, de-embedding method is used to isolate the measurements of channel from the cables. This method is usually implied in frequency sweep domain where adapter connection effects are de-embedded from the device under test (DUT). In our scenario, the de-embedding has to be done in continuous time mode to remove any motion artifacts. The other important point to notice is that since the cable connected to the other antenna does not move, these phase changes are negligible in that scenario. Fig. 49 shows the phase change of S11 parameter in this

[2]Note that this motion does not include the propeller motion which causes amplitude modulation in the received signal.

[3]`https://github.com/amitkac/uavSim`

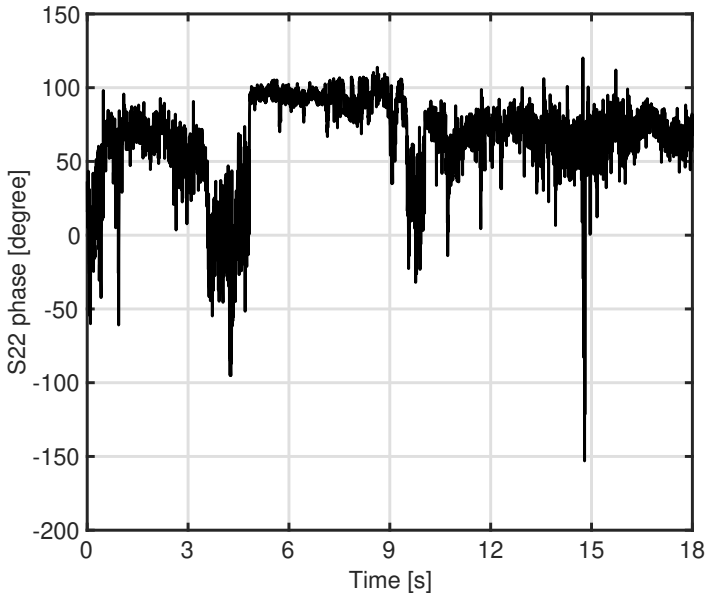

Figure 48: Phase changes in S22 with arm motion when the distance between Tx and Rx is at 5.5 feet.

case.

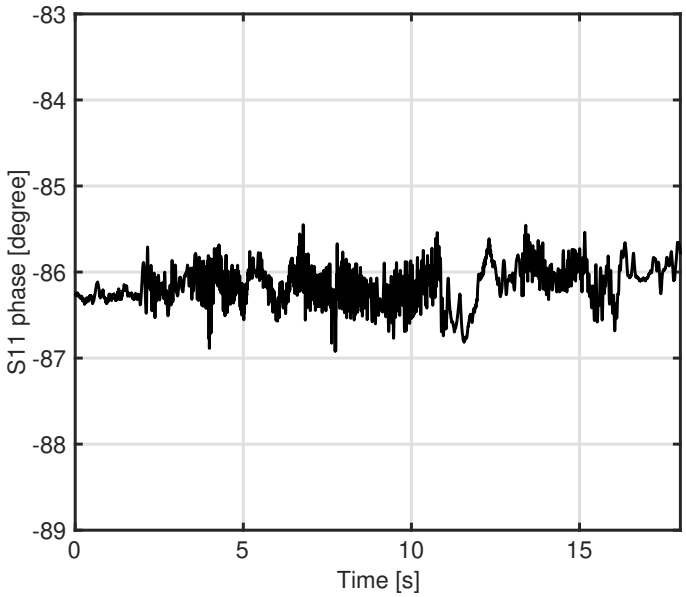

Figure 49: Phase changes in S11 with arm motion when the distance between Tx and Rx is at 5.5 feet.

The maximum deviation between minimum phase change (-86.92°) and the maximum phase change (-85.45°) is around 1.47°, which is acceptable for Doppler measurements. Therefore, the effect of this cable can be ignored in the final de-embedding equation but

the other cable can't be ignored.

4.4 De-embedding the Phase Changes Caused by Cable Movement

The de-embedding [130, 131] of phase during the measurements can be performed by first determining the two-port S-parameters of the cable from the collected S-parameter data with short, open, and load (SOL) standards. The robotic arm has to perform the same motion during data collection with each of these three standards. The process is similar to "Adapter Characterization" function within Keysight VNAs [131], which involves Short-Open-Load calibrations at two different reference planes. The only difference is that this process is performed over time-swept data rather than frequency-swept data.

With a known standard at output (SOL), the measured reflection coefficient would be given as,

$$\Gamma_m = S_{11} + (S_{12} \cdot S_{21})\Gamma_a/(1 - S_{11} \cdot \Gamma_a) \tag{4.4.1}$$

where Γ_m is the measured reflection coefficient with motion, Γ_a is the actual ideal reflection coefficient (no-motion) and $S11, S12, S21, S22$ are the scattering parameters. This can be easily deduced from the signal flow graph in Fig. 50.

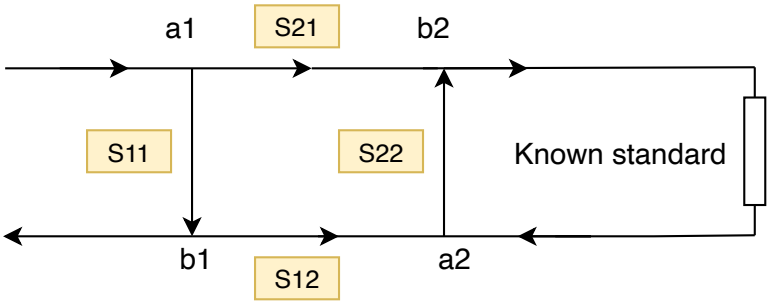

Figure 50: Signal flow graph.

With the data collected with three standards (ideal no-motion), and data from measurements (with motion), we can then have 3 equations to determine the 3 unknown scattering parameters ($S_{12} = S_{21}$ of the cable. Let,

$$\begin{aligned} a &= S_{21}S_{12} - S_{11}S_{22} \\ b &= S_{11} \\ c &= -S_{22} \end{aligned} \tag{4.4.2}$$

Now, with three known standards (Γ_s,Γ_o,Γ_l) and three measured values with motion ($\Gamma_1, \Gamma_2, \Gamma_3$), the three linear equations can be written as,

$$\begin{aligned} \Gamma_1 &= \Gamma_s \cdot a + b - \Gamma_s \cdot \Gamma_1 \cdot c \\ \Gamma_2 &= \Gamma_o \cdot a + b - \Gamma_o \cdot \Gamma_2 \cdot c \\ \Gamma_3 &= \Gamma_l \cdot a + b - \Gamma_l \cdot \Gamma_3 \cdot c \end{aligned} \tag{4.4.3}$$

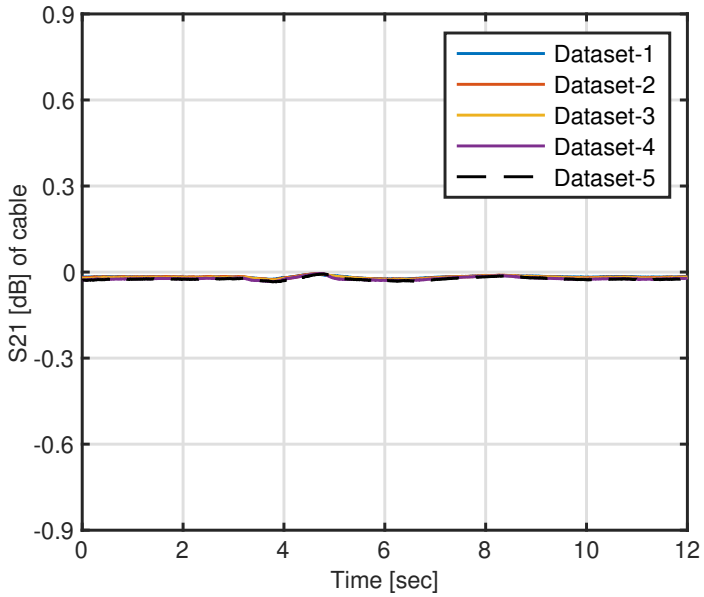

Figure 51: Magnitude variations of S21 data collected in the repeatablity test. The S21 magnitude of all these 5 datasets lay on top of each other.

Which in matrix form can be written as,

$$\begin{bmatrix} \Gamma_s & 1 & -\Gamma_s\Gamma_1 \\ \Gamma_o & 1 & -\Gamma_o\Gamma_2 \\ \Gamma_l & 1 & -\Gamma_l\Gamma_3 \end{bmatrix} \begin{bmatrix} a \\ b \\ c \end{bmatrix} = \begin{bmatrix} \Gamma_1 \\ \Gamma_2 \\ \Gamma_3 \end{bmatrix} \tag{4.4.4}$$

Therefore,

$$\begin{bmatrix} a \\ b \\ c \end{bmatrix} = \begin{bmatrix} \Gamma_s & 1 & -\Gamma_s\Gamma_1 \\ \Gamma_o & 1 & -\Gamma_o\Gamma_2 \\ \Gamma_l & 1 & -\Gamma_l\Gamma_3 \end{bmatrix}^{-1} \begin{bmatrix} \Gamma_1 \\ \Gamma_2 \\ \Gamma_3 \end{bmatrix} \tag{4.4.5}$$

Substituting these a, b, c values, the S-parameters can be determined from (4.4.2). We repeat all of this for 5 times to see the variations in the S-parameters (magnitude as well as phase) for the cable under motion. In our case, it was found that the phase variation (min-max) after de-embedding ranged from -4° to +0.6° , while the magnitude variation (min-max) ranged from -0.033 dB to -0.007 dB for the phase stable cable in an anechoic chamber. Fig. 51 and Fig. 52 show these variations in our scenario. Later on, offset calibration was also done by removing S21 of the cable from the measured data.

Later on, offset calibration was also done by removing S_{21} of the cable from the measured data. To de-embed the cable phase changes and get the channel response, we can transform the S-matrix of cable and measurements into its corresponding T-matrix as follows,

$$\begin{bmatrix} T_{11} & T_{12} \\ T_{21} & T_{22} \end{bmatrix} = \begin{bmatrix} S_{21} - S_{11}S_{22}/S_{12} & S_{22}/S_{12} \\ -S_{11}/S_{12} & 1/S_{12} \end{bmatrix} \tag{4.4.6}$$

The T-matrix treats the port-2 as output and port-1 as input, which makes it easy to

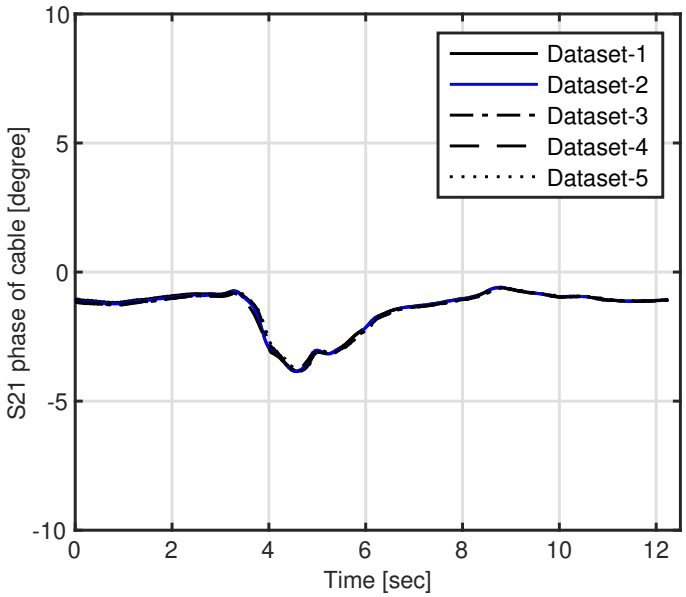

Figure 52: Phase variations of the S21 data collected in the repeatablity test. The S21 phase of all these 5 datasets lay on top of each other.

use in cascaded systems. Finally, the channel T-matrix can be found as,

$$\begin{aligned} T_{meas.} &= T_{cable} T_{channel} \\ T_{channel} &= T_{meas.}/T_{cable} \end{aligned} \tag{4.4.7}$$

This T-matrix of channel then can be transformed back to S-matrix as follows,

$$\begin{bmatrix} S_{11} & S_{12} \\ S_{21} & S_{22} \end{bmatrix} = \begin{bmatrix} T_{21}/T_{22} & 1/T_{22} \\ T_{11} - T_{12}T_{21}/T_{22} & T_{12}/T_{11} \end{bmatrix} \tag{4.4.8}$$

Now, with this we will have the channel S-paramaters where the cable effects are removed. Before moving on to the Doppler analysis and path loss modeling, another important statistical factor needs to be considered, which is the wide sense stationary with uncorrelated scattering (WSSUS) conditions that will be discussed in the next subsection.

4.5 WSSUS Conditions

One other important characteristic of wireless channel to check when there is a mobility in it is its stationary conditions, especially WSSUS. It is well known that UAV or vehicular communication does not follow wide sense stationary conditions with uncorrelated scattering. To examine stationary conditions, autocorrelation function is used and characterised. The channel autocorrelation function as a function of time t, and delay τ is written as,

$$R_{xx}(t_1, t_2; \tau_1, \tau_2) = E[h(t_1, \tau_1) h^*(t_2, \tau_2)], \tag{4.5.1}$$

where $h(t_1, \tau_1)$ is the channel impulse response at time t_1 and with delay τ_1, and $h^*(t_2, \tau_2)$ is the complex conjugate of the channel impulse response at another time t_2 and with delay τ_2. There are two important parts to be considered for WSSUS conditions,

WSS Conditions

A wireless channel is assumed to be WSS, if its mean is constant over time and if its channel response is independent of time t. In terms of autocorrelation, $R_{xx}(t_1, t_2; \tau_1, \tau_2)$, should be independent of time instant t, and must depend on time difference Δt. These two conditions can be written as,

$$\begin{aligned} \mu_x(t) &= \mu_x, \forall\ t \in \mathbb{R}, \\ R_{xx}(\Delta t; \tau_1, \tau_2) &= E[h(t, \tau_1) h^*(t + \Delta\tau, \tau_2)]. \end{aligned} \tag{4.5.2}$$

US Conditions

For a wireless channel to assume uncorrelated scattering, the individual scattering components that arrive at the receiver should be uncorrrelated. In terms of autocorrelation function,

$$R_{xx}(t_1, t_2; \tau_1, \tau_2) = R_{xx}(t_1, t_2; \tau_1)\delta(\tau_1 - \tau_2) \tag{4.5.3}$$

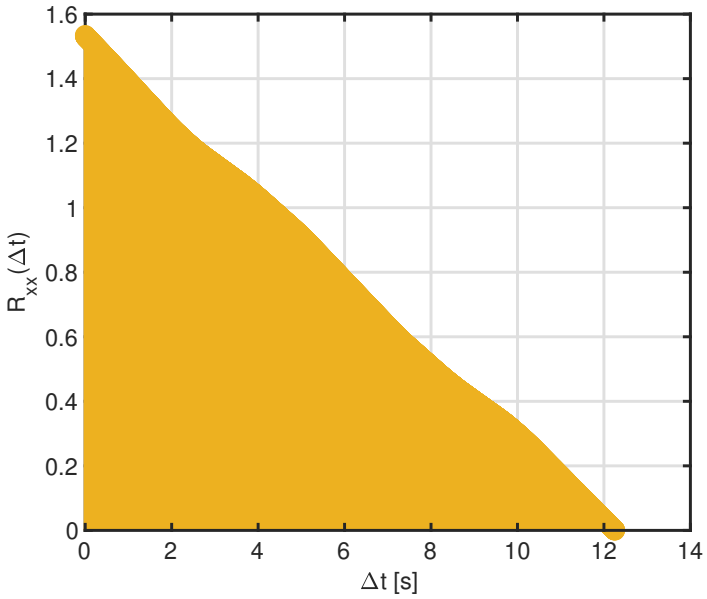

Figure 53: One sided autocorrelation of S21 data at 3.5 feet over delay in anechoic chamber.

Therefore, for WSSUS conditions to be true, the mean should be constant and the autocorrelation function should be independent of the time. Looking at the autocorrelation function plot over time for anechoic chamber in Fig. 53 and a sample measurement of indoor

environment in Fig. 54, it can be intuitively inferred that the WSSUS conditions can be assumed true for anechoic chamber but not for the indoor environments.

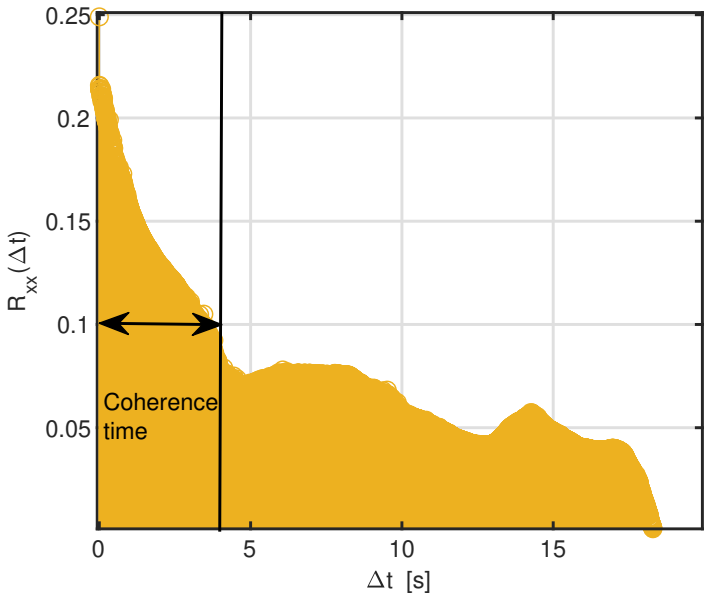

Figure 54: One sided autocorrelation of a sample S21 data at 3.5 feet over delay in an indoor environment.

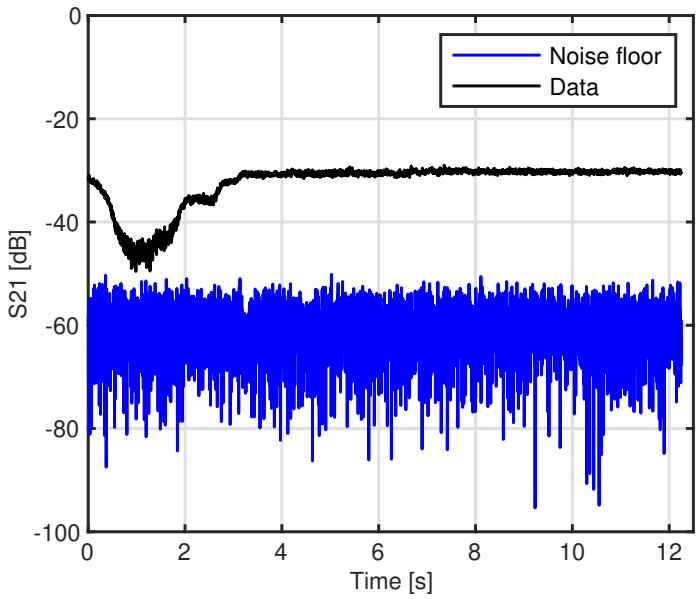

Figure 55: Measurement data with noise floor at 3.5 feet over time in an anechoic chamber.

Also, looking at Fig. 55, one can observe that the mean in our anechoic chamber set-up remains constant most of the time. The figure also shows the noise floor for our measurement campaign. In real scenario of outdoor or indoor environment, the WSSUS conditions

may not be true and thus will require extensive measurement campaigns to validate before generalization. By now, we have have performed the de-embedding to take care of phase changes because of cable motion, and also examined the WSSUS conditions. Now, in the next section, we will delve more into the Doppler spread analysis and path loss modeling.

4.6 Analysis of Doppler Spread and Path Loss

In this section, first the data processing of the pre-processed (de-embedded and offset-calibrated) VNA data (S-parameters), and its correlation with the motion profile extracted from the ROS logs will be analyzed, and then the analysis of Doppler spread and path loss characteristics will be discussed in detail. Let the transmitted signal, $x(t) = \Re\{b(t)e^{j2\pi f_c t}\}$, where $b(t) = x_I(t) + jx_Q(t)$ is a complex baseband signal with in-phase and quadrature components as $x_I(t)$ and $x_Q(t)$, and f_c is the carrier frequency. The signal $b(t)$ is also known as the complex signal envelope or an equivalent low pass signal of $x(t)$. Ignoring the noise in the system, the corresponding received signal with the line of sight (LOS), and all resolvable multipath is given as [67],

$$y(t) = \Re\left\{\sum_{n=0}^{N(t)} \alpha_n(t) b(t - \tau_n(t)) e^{j2\pi[f_c(t-\tau_n(t))+\phi_{d_n}+\phi_0]}\right\}, \tag{4.6.1}$$

$$y(t) = \Re\left\{\left[\sum_{n=0}^{N(t)} \alpha_n(t) b(t - \tau_n(t)) e^{-j(2\pi f_c \tau_n(t)+\phi_{d_n}+\phi_0)}\right] \times e^{j2\pi f_c(t)}\right\}. \tag{4.6.2}$$

which can be further written as,

$$y(t) = \Re\left\{\left[\int_{-\infty}^{+\infty} h(t,\tau) b(t-\tau) d\tau\right] e^{j2\pi f_c(t)}\right\}, \tag{4.6.3}$$

where $h(t,\tau)$ is the channel impulse response given as,

$$h(t,\tau) = \sum_{n=0}^{N(t)} \alpha_n(t) e^{-j(2\pi f_c \tau_n(t)+\phi_{d_n}+\phi_0)} \delta(\tau - \tau_n), \tag{4.6.4}$$

where $\alpha_n(t)$ is a function of path loss and shadowing, $N(t)$ is the N-th resolvable multipath, τ_n is the N-th path delay, ϕ_0 is the phase offset, and ϕ_{d_n} is the Doppler phase shift of this N-th path. Now, when the Tx or Rx is moving, the change in the distance over a short time interval Δt will cause the phase to change as $\phi_{d_n} \approx 2\pi(v/\lambda)\Delta t \cos\theta$, where θ is the arrival angle of the received signal relative to the direction of motion, and v is the velocity of receiver towards transmitter in the direction of motion. Therefore, the corresponding Doppler frequency will then be given as,

$$f_D = \frac{1}{2\pi}\frac{\phi_{d_n}}{\Delta t} = \frac{v}{\lambda}\cos\theta, \tag{4.6.5}$$

where λ is the wavelength of the signal. The data collected at VNA during the measurement campaign are the S-parameters, also known as scattering parameters, over time (CW mode).

Since the Tx is connected at port-1 and Rx at port-2, therefore, the S21 parameter will represent the channel transfer function (channel power). These S-parameters depend on time, distance and frequency. Thus, S21 parameter as a channel transfer function of time, distance, and frequency can be written as [42, 132],

$$\mathrm{S21}_{dB}(t, f, d) = 20 \log_{10}(|H(t, f, d)|) \tag{4.6.6}$$

As the VNA is set in CW time mode with frequency kept fixed at 28 GHz, the only variable in (4.6.6) would be the discrete time points at a given distance. Therefore, at a given distance d, (4.6.6) can be rewritten as,

$$\mathrm{S21}_{dB}(t, f, d) = \mathrm{S21}_{dB}(t) \tag{4.6.7}$$

These discrete points of S21 parameter can be written in a complex vector form as, $x[n] = \mathrm{S21}_{dB}(t)\delta(t - t_i)$, where t_i is the discrete time point, $\delta(\cdot)$ is the delta function, and the index i goes from 0 to 4095. Because the S21 parameters are complex numbers, therefore, the frequency response after taking the fast Fourier transform (FFT) would also be complex in nature. Therefore,

$$X[k] = \frac{1}{N} \sum_{n=0}^{N-1} x[n] e^{-j2\pi kn/N}, \tag{4.6.8}$$

where k is the point in the frequency domain, n is the point in time domain, and $x[n]$ is the discrete time domain input (vector of all 4096 points). Fig . 55 shows a sample S21 data with noise floor collected at 3.5 feet.

4.6.1 Doppler Spread

As mentioned previously, in our set up, 4096 points were set in the CW time mode, this number was chosen so that the Discrete Fourier transform (DFT) can be efficiently calculated by using the FFT algorithm as the data points will be in the form of 2^n. As N=4096, (4.6.8) can be rewritten as follows,

$$X[k] = \frac{1}{4096} \sum_{n=0}^{4095} x[n] e^{-j2\pi kn/4096}, \tag{4.6.9}$$

where $k = 0, 1, \ldots 4095$. Doppler spectrum after taking the FFT of S21 parameters at a distance of 5.5 feet is shown in Fig. 56. To demonstrate the accuracy of the collected data for the Doppler analysis, we reprogrammed the robotic arm to do a controlled motion (to and from) with a pre-defined linear speed in an anechoic chamber. The robotic operating system, also known as ROS, captures various fields of the end point (velocity and displacements) of the arm in the system logs in *.bag* format. These files are later converted to *.csv* format to process with the MATLAB software.

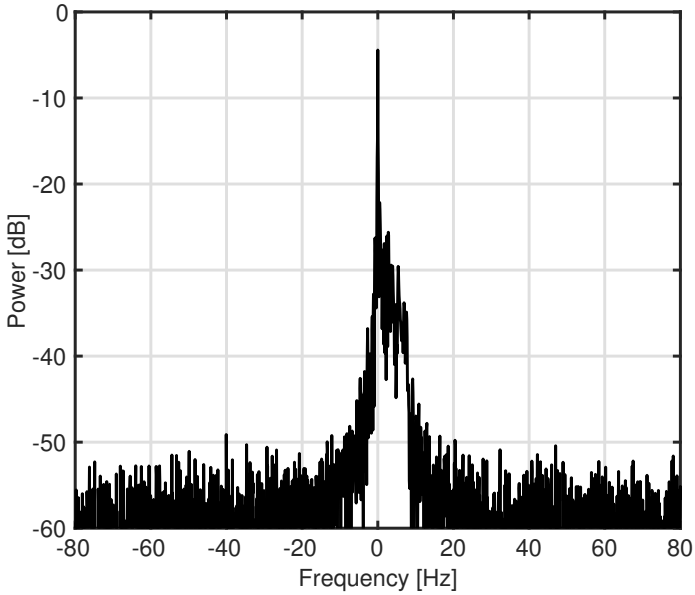

Figure 56: Doppler spectrum at 5.5 feet.

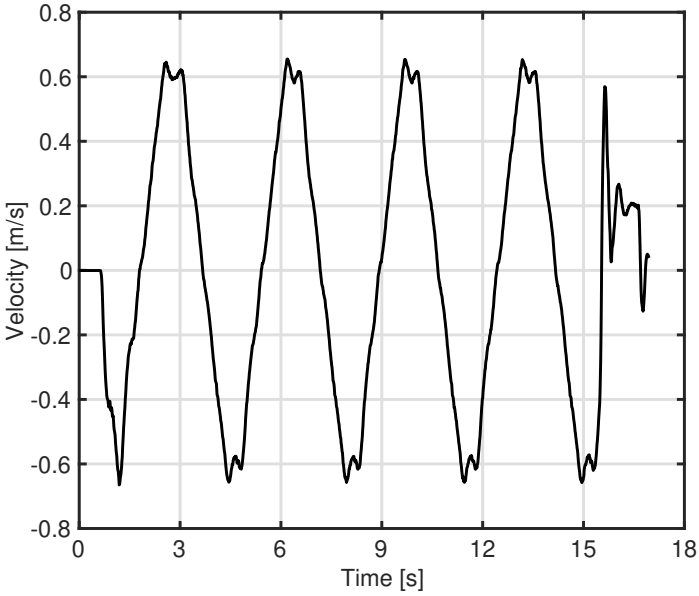

Figure 57: Controlled linear change of the arm speed in an anechoic chamber.

On close analysis, it can be observed that the velocity of this control system will go from 0 m/s to 0.58-0.63 m/s and will stay there at this peak for some time in one direction and will do the same while going back (0 m/s to -0.58 to -0.61 m/s). The corresponding probability density function (pdf) of velocity change over time (Fig. 57) is shown in Fig. 58. Intuitively, since velocity is proportional to the ideal Doppler observed, the frequency corresponding to the peaks in the velocity pdf will also be seen in the Doppler spectrum. For example, speed at the peak of 0.59 m/s to 0.64 m/s will correspond to a theoretical Doppler of 55.1 Hz to

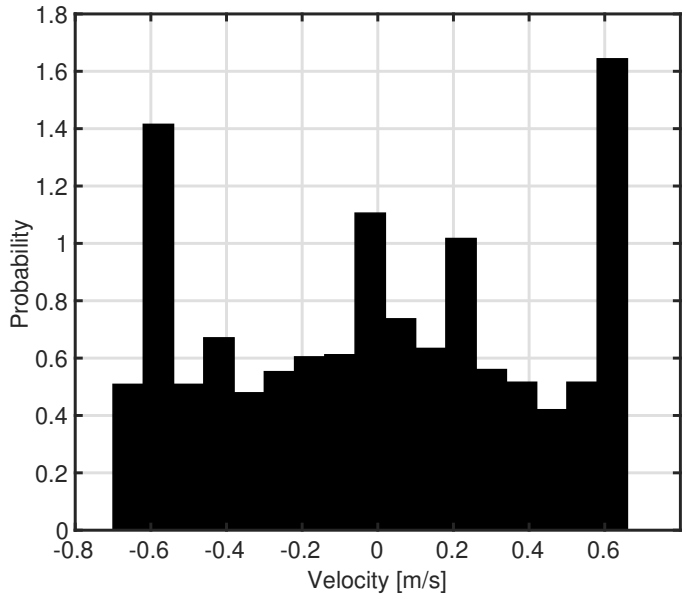

Figure 58: Velocity distribution over time.

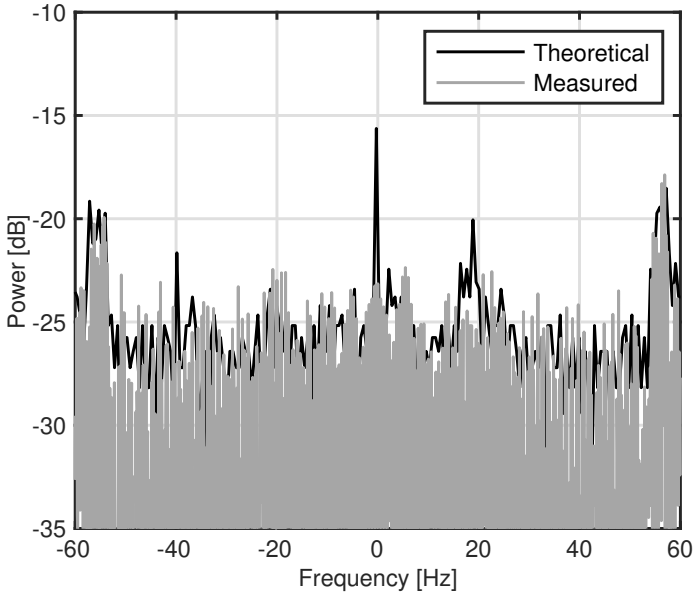

Figure 59: Theoretical Doppler with Measured Doppler at 5.5 feet.

59.7 Hz, while the speed of -0.58 m/s to -0.64 m/s will correspond to Doppler of -54.17 Hz and -59.7 Hz, which can be seen in the Doppler spectrum[4] as shown in Fig. 59.

The resulting maximum positive Doppler spread (motion towards the receiver) and negative Doppler spread (motion away from the receiver) at each distance in an Anechoic chamber is shown in Table 9 with respect to the noise floor of -60 dB. The average Doppler spread in

[4]The theoretical Doppler power is offset by 4 dB to fit the measured Doppler spectrum plot.

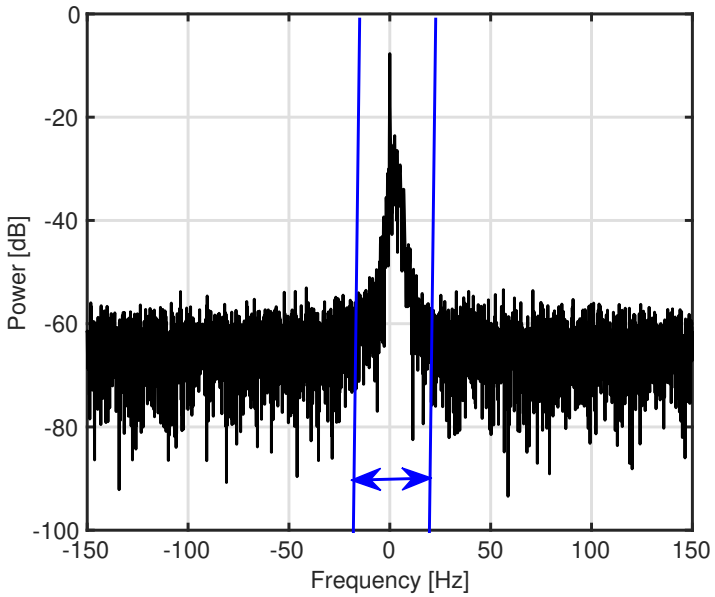

Figure 60: Doppler spread at 11.5 feet in the Anechoic chamber environment.

the Anechoic chamber was found to be around +20 Hz to -20 Hz. Fig. 60 shows an example of the Doppler spectrum at 11.5 feet. It is very important to point out that the data used to capture Doppler is pre-processed to de-embed the phase changes caused by cable motion. These Doppler spread parameters are paramount in designing the symbol duration in a wireless communication system. Specifically, the coherence time depends on this Doppler spread, and if not properly designed for it, will result in frequency selective fading.

4.6.2 Path Loss Modelling

The next part is to statistically model the path loss characteristics of the wireless channel[5]. As mentioned in an earlier section, at each distance point, 3 samples of scattering data were recorded. An example of such 3 samples of 4096 data points appended with each other is shown in Fig. 61. The first initial points (highlighted in Fig. 61) in these S21 power samples represent no-motion or idle motion of UAV. These points can be filtered from the appended samples for each distance, and therefore, can be utilized to determine the distance dependent path loss exponent value in an anechoic environment.

The path gain as a function of distance can be modelled as [42, 67],

$$\mathrm{PG}_{dB}(d) = \mathrm{PG}_{dB}(d_0) - 10n \log_{10}\left(\frac{d}{d_0}\right) + X_\sigma(d), \tag{4.6.10}$$

where $\mathrm{PG}_{dB}(d_0)$ is the path gain at a reference distance d_0, which is 1 meter in our scenario. d is the distance between transmitter and receiver, n is the distance dependent path loss exponent, and $X_\sigma(d)$ is the Gaussian distributed shadowing factor with zero mean in dB, and a variance of σ^2 in dB. The path gain as a function of distance is plotted in Fig.

[5]Note that the effect of variation of elevation, and elevation angle on the Doppler is not considered.

Table 9: Maximum Doppler spread with distance in Anechoic chamber.

Noise floor	Distance [feet]	-ve freq. [Hz]	+ve freq.[Hz]
-60 dB	3.5	-25.3844	24.9763
	5.5	-20.5687	20.3328
	7.5	-18.5282	21.14
	9.5	-26.0374	19.9157
	11.5	-16.4876	22.446
	13.5	-20.3238	20.6503
	15.5	-20.079	20.5687
	17.7	-18.5282	19.5076
	19.5	-16.0795	17.5487
	21.5	-17.4671	20.6503
	23.5	-20.6503	20.4871
Average Doppler [Hz]		-19.4750	20.3204

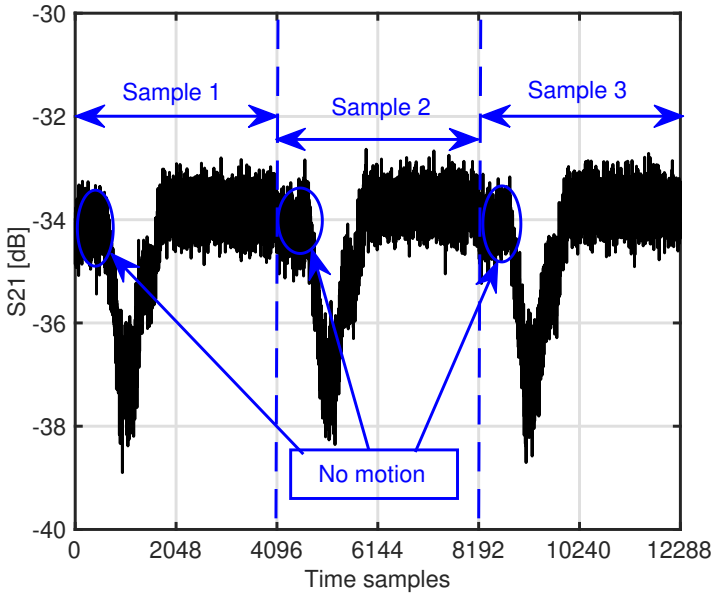

Figure 61: No motion portion in the appended data at 3.5 feet.

62. A linear fitting model is used to find the slope of the plot which is nothing but the path loss factor n. The path loss factor in our anechoic scenario using this linear fitting model was found to be 1.843. Similar close values have been reported in different indoor environments [133–135]. This path loss modeling shows the applicability of such a novel platform for mmWave channel characterizations. Moreover, the path loss factor derived in this work is specific to the measured data in this work and will again require an extensive set of measurements to be generalized for any environment as such. Now, in the following section, we will look in detail at the second part of this chapter, which is the propeller effect in UAV-assisted mmWave communication systems.

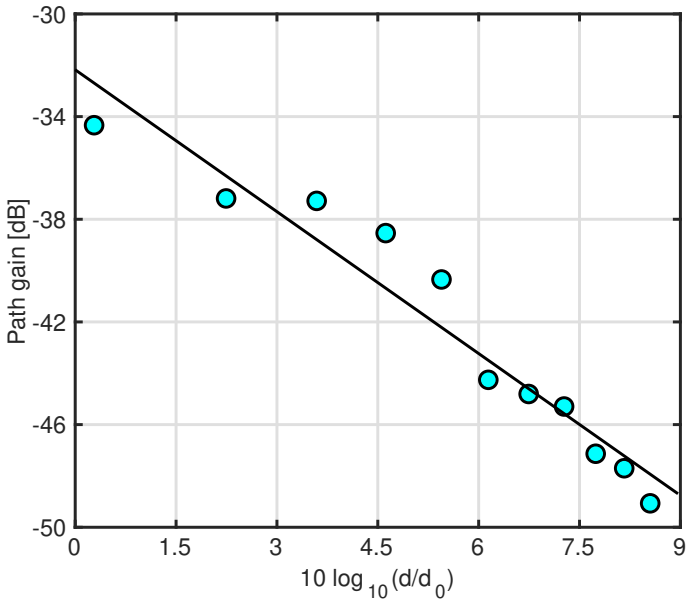

Figure 62: Linear fitting to determine distance dependent path loss.

4.7 Propeller Effects on mmWave communication

With UAVs, there is another important factor that interferes with the communication, which is the signal propagation through propeller or scattering caused by it. The propeller motion is known to induce periodic frequency responses in the received signal, often known as propeller modulation in literature [136–138]. The main cause of the propeller modulation is the periodic motion or revolutions of propeller that makes the received signal to be amplitude modulated. This effect has been well studied at low frequencies with UAVs, aircrafts and helicopters, but has not been studied or validated at higher frequencies such as mmWave. As an example, consider that the frequency of the signal is 2.4 kHz as shown in Fig. 63.

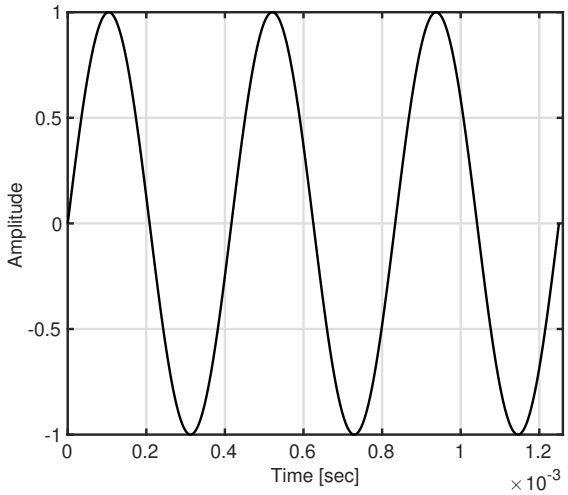

Figure 63: Signal with frequency of 2.4 KHz.

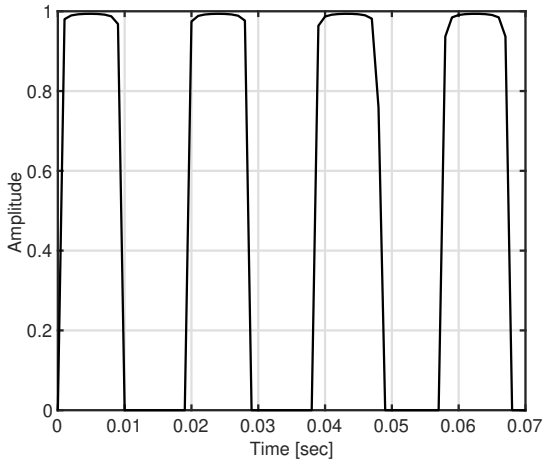

Figure 64: Signal with frequency of 52 Hz caused by propeller.

Once the carrier signal passes through the propellers which are rotating, it will be blocked for a period when there is a propeller between the Tx and Rx, and pass completely when there is no propeller between the Tx and Rx. This will create a waveform with a certain periodic frequency, assumed to be 52 Hz in this example (see Fig. 64). Therefore, the output signal or the received signal after passing though a propeller will look like as shown in Fig. 65, which is nothing but an amplitude modulated waveform.

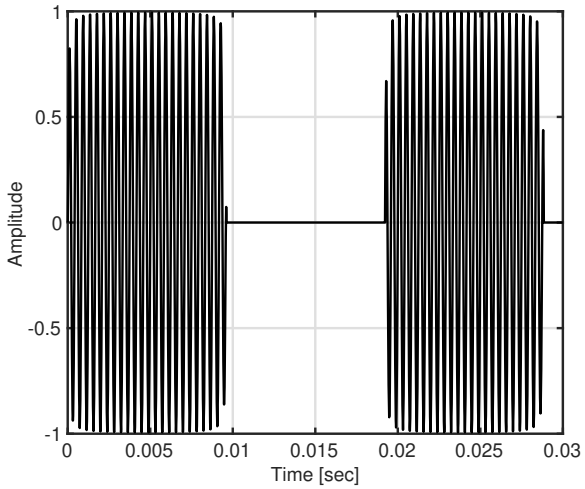

Figure 65: Received amplitude modulated signal at the receiver.

This effect is more interesting to study in a UAV-to-UAV communication scenario at different height configurations, with different mmWave antenna top-bottom permutations or configurations on UAV. Different UAV speed modes (idle/high) can also be considered in these cases. Fig. 66 shows the different antenna set-up configurations considered in this Chapter 4. It is also worth noting that the configurations 2) and 4) are the same. In this chapter, we will study this propeller effect with a real hexcopter. In next sub-section, we will discuss the measurement setup and thereafter, we will delve into the results and discussion

on propeller modulation.

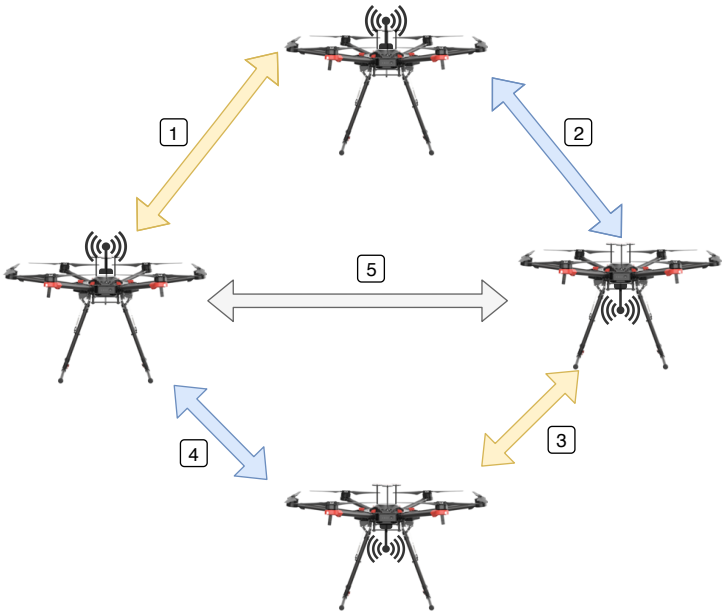

Figure 66: Different antenna configurations considered in the measurement setup, 1) Antenna on top of one UAV-antenna on top of the other, 2) Antenna on top of one UAV-antenna on bottom of other, 3) Antenna on bottom of one UAV-antenna on bottom of other, 4) Antenna on bottom of one UAV-antenna on top of other UAV, and 5) UAVs at same height with antenna on top of one UAV-antenna on bottom of other UAV.

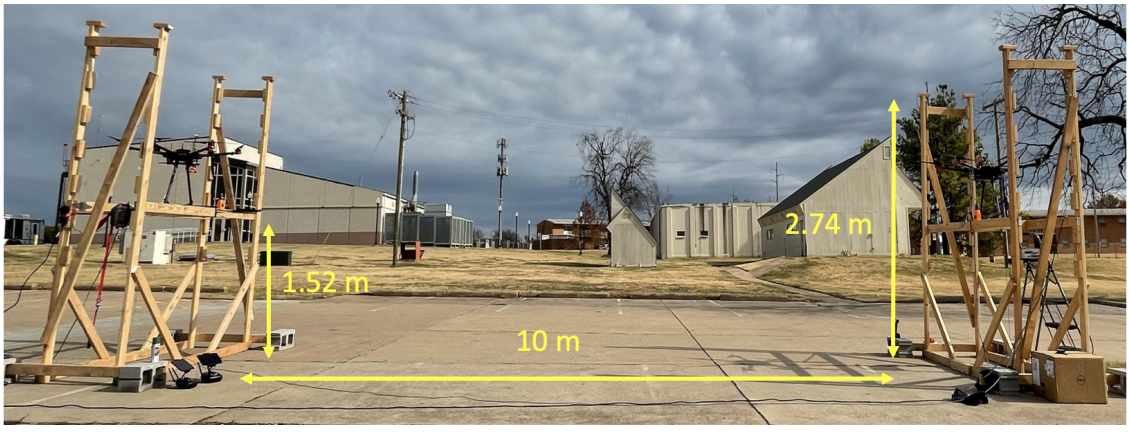

Figure 67: Measurement layout with the two custom wooden ladders with wooden platforms to hold the Hexcopter.

4.7.1 Measurement Setup

In this section, the measurement set-up to examine the effect of propeller on mmWave signal will be discussed in detail. To avoid scattering from walls or roof, these measurements were conducted outdoors in a parking lot area. A custom platform with two wooden ladders

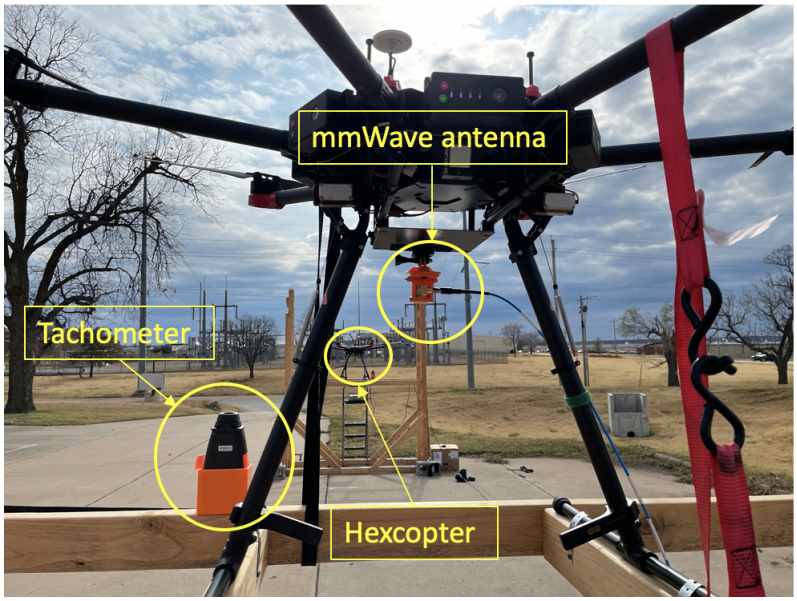

Figure 68: Measurement set-up with mmWave antenna mounted on bottom of one hexcopter with the other hexcopter in plain sight.

with a movable wooden base platform between them was constructed that could be moved from 5 feet (1.52 meter) to 9 feet (2.74 meter) maximum (on top)[6]. Two such custom platforms were used for the two hexcopters in this measurement campaign. The distance between the two custom platforms was kept at 10 meters. Fig. 67 shows the actual layout of our measurement set-up, with the custom wooden platform built for this measurement campaign. On this custom wooden platform, to hold the hexcopter, its legs were strapped firmly with a metallic band onto the movable wooden base with screws. Also, the base is weighted with concrete blocks to secure them in position. Fig. 68 shows the hexcopters with the mmWave antenna, and laser based tachometer. The tachometer is used to capture the actual revolutions per minute (rpm). The complete measurement equipment details are given in Table 10.

To overcome the propagation loss between two UAVs, a low noise amplifier is inserted between the Rx antenna and spectrum analyzer. The spectrum analyzer functionality was used in the VNA to capture the propeller modulation effect. The transmit power was kept at -10 dBm and the VNA was set to work in continuous wave mode at 28 GHz. In the spectrum analyzer setting, the center frequency was set at 28 GHz, with a frequency span of 1 kHz to capture the propeller modulation in idle speed and 2 kHz for high speed mode. The residual bandwidth was set at 7.5 Hz and 401 points were selected for the entire frequency span. The hexcopter has two modes of operation, 1) idle speed and 2) high speed. In our scenario, for a particular antenna configuration, and a given hexcopter mode, we take 4 sets of measurements, a) without propeller motion, b) with only one propeller-on at Tx, c) With only one propeller-on at Rx and d) with both propeller-on. This way we will have 4 configurations for a given antenna configuration, and with these total of 4 antenna

[6]The height is the platform height or height till the bottom of the hexcopter, the hexcopter height is 14 inches.

Table 10: The measurement equipment with specifications.

Equipment	Specifications
Signal generator + Spectrum analyser	Keysight Fieldfox N9951A,300 KHz to 44 GHz
Antenna (rectangular horn type)	Cernexwave (CRA28264015), 26.5 GHz-40 GHz, Gain: 15 dBi, HPBW:18°
Waveguide transition	Cernexwave (CWK28264003F), WR-28, Brass/Copper
Low noise amplifier	Cernexwave (CBL26403030), 26.5 GHz-40 GHz, V/mA: 12/150, NF(dB) Max: 3, Gain (dB) 30 min
Cables	Fairview microwave (50 feet), Mini-Circuits (5 feet)
Hexcopter	DJI Matrice 600, max. altitude: 2500 m, Carbon fiber propellers, maximum speed: 18 m/s
Tachometer	Neiko, 20713A digital tachometer, Accuracy: +/- 0.05%, range:2-20 inches

configurations, there will be 16 cases in total. Since we consider bottom-top and top-bottom antenna configuration as one, there would be only 12 such cases. These 4 sets of antenna configurations are shown in Fig. 66. This is considering fixed height of both Tx and Rx, both Hexcopter at 5 feet from the ground. To include the effect of both propellers in the picture, the same set of measurements is conducted with a hexcopter at different heights (one at 9 feet and the other at 5 feet). In addition to that, with two speed modes of idle and high, the overall cases will then be 48.

During the measurements, we also confirmed that there will be no modulation tones when the propellers are off, and thus these cases of both propeller-off are removed from the final measurements. This reduces the overall case scenarios to 36 cases. To correlate the theoretical frequency of the propeller modulation with the measured value, a laser based tachometer is used that gives the actual revolutions per minute (rpm) readings with 0.05% accuracy. Duct tape is used on the propeller for this laser-based sensing scenario. In the next section, we will look into the results and subsequent discussion on the observed propeller effect in detail.

4.7.2 Results and Discussion

In this section, we will first look at the expected theoretical component of the tone generated by propeller modulation, and then validate it with the measurement results captured on the spectrum analyzer. Given the signal propagation through the propeller, the signal will get scattered/partially blocked by the propeller while it's turned-on, causing the signal to behave as an amplitude modulated dual sideband signal with a certain frequency that depends on the propeller speed. Let r be the revolutions per minute (rpm) of the propeller, and n be the number of blades of the propeller. The frequency spectrum of the output signal will have

the original frequency component with an additional periodic frequency tone given by,

$$f_b = \frac{n \times r}{60} \tag{4.7.1}$$

This frequency component appears next to the central frequency of 28 GHz as $28 \pm mf_b$ GHz, where $m = 1, 2, 4, \ldots, 2x$ or even harmonics. As mentioned earlier, the hexcopter works in two different speed modes-idle speed and high speed. At idle speed, the rpm remains constant most of the time and at the high speed the rpms increase over time to reach the highest possible rpm. In our scenario, the rpm at idle speed was measured to be 1580,

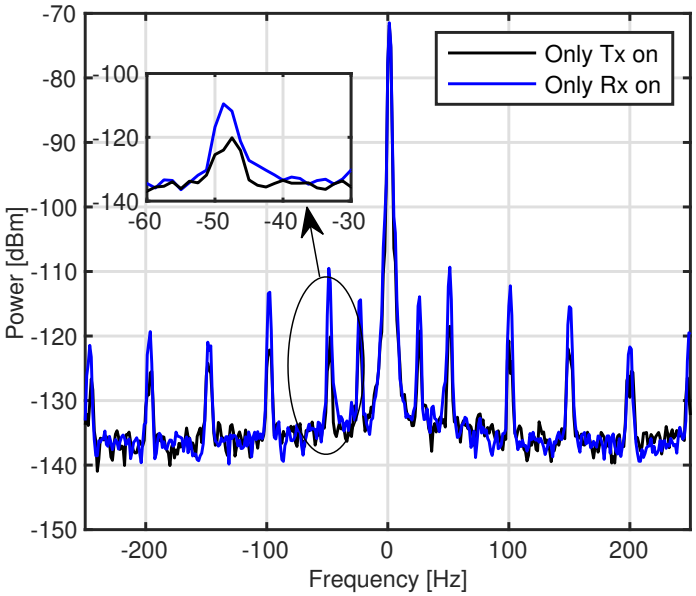

Figure 69: Spectrum when only one propeller is on for the case when antennas are on top of both hexcopters.

with two propellers, the fundamental frequency comes to be, 52.97 Hz. This fundamental frequency can be seen in all the antenna configurations, even at different heights but only at the idle speeds. Fig. 69, and Fig. 70 shows two such cases.

In Fig. 69, the case of one propeller being turned-on, while the other is turned-off is shown and in Fig. 70, the case of both propellers turned-on and -off is shown. The fundamental frequency that occurs in even harmonics is at 51.25 Hz at idle speed, while we also observe 26.25 Hz (half of the fundamental frequency) in spectrum, which will be examined shortly. In the case of high speed, the fundamental frequency comes at around 125 Hz with the measured rpm of 3750. The same inferences are made when the hexcopter is kept at different heights (5 feet and 9 feet) with different antenna configuration. One such example is given in Fig. 71

To examine the presence of 26 Hz of tone in the case of idle speed, one may think that the cause of this may be the vibration from the frame, motor or may be because of scattering effect[7]. To rule out the effect of motor, we removed the propeller and kept the motors on.

[7]It is important to note that this is related to this measurement set-up and may or may not be present in actual UAV flying in the air.

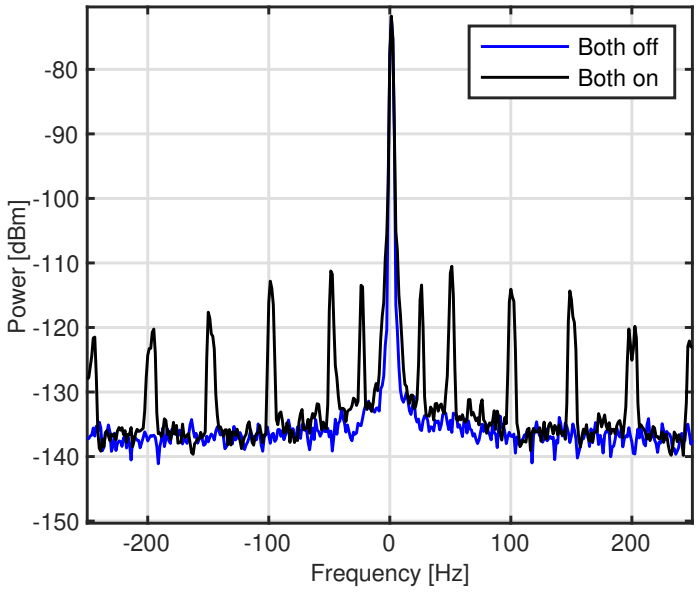

Figure 70: Spectrum when both propellers are on and off for the case when both antennas are on Top of hexcopter.

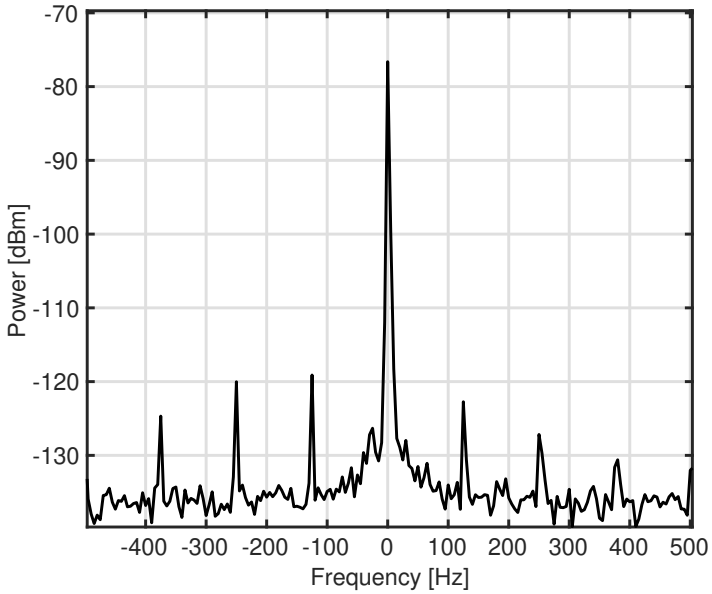

Figure 71: Spectrum when the Tx is on top of one hexcopter and the Rx is on bottom of the other and they are operated in high speed mode.

In this situation, the 26 Hz component or any fundamental frequency was not observed. Now, to rule out the effect of body frame vibration, we placed the antenna just below the hexcopter on a stable wooden platform, and turned-on the propellers. In this situation, we did observe the 26 Hz and other fundamental frequencies. Therefore the main cause of this frequency has to do with the propeller not with the body frame vibrations. To probe further,

Table 11: Propeller modulation with different combinations of height, speed, antenna configuration (bottom (B) or top (T)) and with propellers turned-on or -off.

Height	Speed mode	Antenna config.	Propeller on	Main tone [Hz]	Periodic (yes/no)
Same	Idle	B-B B-T T-T	Tx. only Rx. only Both	52	yes
	High	B-B B-T T-T	Tx. only Rx. only Both	125	yes
Different	Idle	B-B B-T T-T	Tx. only Rx. only Both	52	yes
	High	B-B B-T T-T	Tx. only Rx. only Both	125	yes

we let the six propellers (hexcopter) to run in different combinations-first 2 front propellers, then 4 propellers and then all the propellers. In all these experiments, the antenna is fixed on the stable wooden platform/ or in another case on the hexcopter, we do see the 26 Hz frequency in all these cases with the fundamental harmonic frequency.

On careful observation, we observed that the propeller arm that connects the propeller to the main body wobbles at idle speed, and this actually behaves like a single blade propeller. This explains the frequency of this tone, which exists exactly at the half of the main fundamental frequency of 52 Hz. Furthermore, to cement this conclusion, one of the propeller arms was purposefully imbalanced with duck-tape to create extra wobble and in this case also, we observed the 26 Hz frequency. However, in high-speed mode the speed increases linearly to high-speed and therefore the wobble of the propeller arm does not exhibit any such frequency component. In fact, one can observe that spread in Fig. 71 between 0 ± 100 Hz frequency[8]. All the results obtained in this measurement campaign are listed in Table 11. The propeller effects in addition to Doppler and path loss are very important to efficiently design and build UAV-assisted next generation 5G and B5G communication systems.

[8]It is very important to know that this frequency is because of the measurement setup and not because of the UAV itself, and therefore may not be present in actual flying UAVs.

4.8 Conclusions

In this chapter, we studied and examined the mmWave communication systems for UAVs in detail. First, we looked into a novel emulation framework for such mmWave communication systems to determine channel charactersists such as Doppler spread and path loss. In the later part, we looked into the case of propeller effects on mmWave. For the later study, we used a real hexcopter and conducted the field measurements in a parking lot, and subsequently validated the presence of propeller modulation at mmWave frequencies in different height, speed and antenna configurations. In short, the main conclusions of this chapter are as follows,

1. Doppler spread analysis and path loss characterization using a novel emulation method is presented in which the actual UAV motion under Dryden wind conditions was mimicked by a robotic arm in an anechoic chamber environment.

2. The path loss exponent value under these anechoic settings was found to be 1.843.

3. Study of WSSUS conditions in an anechoic environment and its applicability to other environments was also examined.

4. Study of propeller effect at different height, different antenna configuration and with different speed modes with actual hexcopter was conducted and its relationship with propeller motion was validated.

These results in this chapter will help propel the development of mmWave based UAV communication systems in the near future. In the next chapter, overall conclusions and future work of this thesis will be discussed in detail.

CHAPTER V

CONCLUSIONS AND FUTURE WORK

5.1 Conclusions

In this thesis, we looked at the solutions to the problem of spectrum crunch at sub-6 GHz, which is getting more crowded day by day. There are two ways to address this challenge, one is to look into the optimization of the radio resources in the available spectrum for efficient utilization, and the other way is to migrate to a higher frequency (UWB and mmWave) that offers higher bandwidths, which can take care of higher data traffic. To that end, we first studied cognitive radio networks in Chapter II from the spectrum optimization perspective. The CRN was assumed to be in an underlay configuration, where it is concurrently accessed by licensed and unlicensed users provided that the power from SUs or unlicensed users does not degrade the transmission of primary PUs or licensed users. The PU controls this by setting a transmit power threshold for SUs, known as IT. The traditional approach is to keep the IT fixed, while this may work but it is very restrictive and inefficient as it does not consider the variation of traffic demand over time. In brief, we statistically modeled the IT or interference power threshold from the variable capacity demand of PU as a dynamic quantity. By using the random variable transformations, the distribution of IT was determined from PU capacity demand. The PU capacity demand variation over the time was assumed to follow Poisson distribution, and consequently, using statistical transformations of random variables, the distribution of SINR, and finally IT distribution was determined. This expression was validated and verified with simulations. Theoretical expressions for outage probability and mean capacity for SU in the general power region, and in the high power region were also derived and verified with simulation results. Finally, we analyzed the effect of utilizing a dynamic interference power threshold on the mean and instantaneous capacity, and on the outage probability. It was shown that the dynamic IT substantially improves the network performance as compared to a fixed IT based cognitive radio system.

In the later part of Chapter II, we also examined the effect of SU interference on PU network. This is a very important aspect to consider before setting the IT dynamically as it is the PU which dictates the setting of IT. Performance metrics for PU network are derived and validated with simulations to show the accuracy of the derived expressions. Although we are now migrating towards the high frequency with 5G and B5G communication, the optimization of present or radio resource at these high frequencies will remain a very important research area that will keep gaining momentum over time. The contributions and general problem solved in this chapter can be visualized in Fig. 72, which also enlists the publications.

Secondly, in Chapter III, we looked into the first high frequency part of the spectrum, that

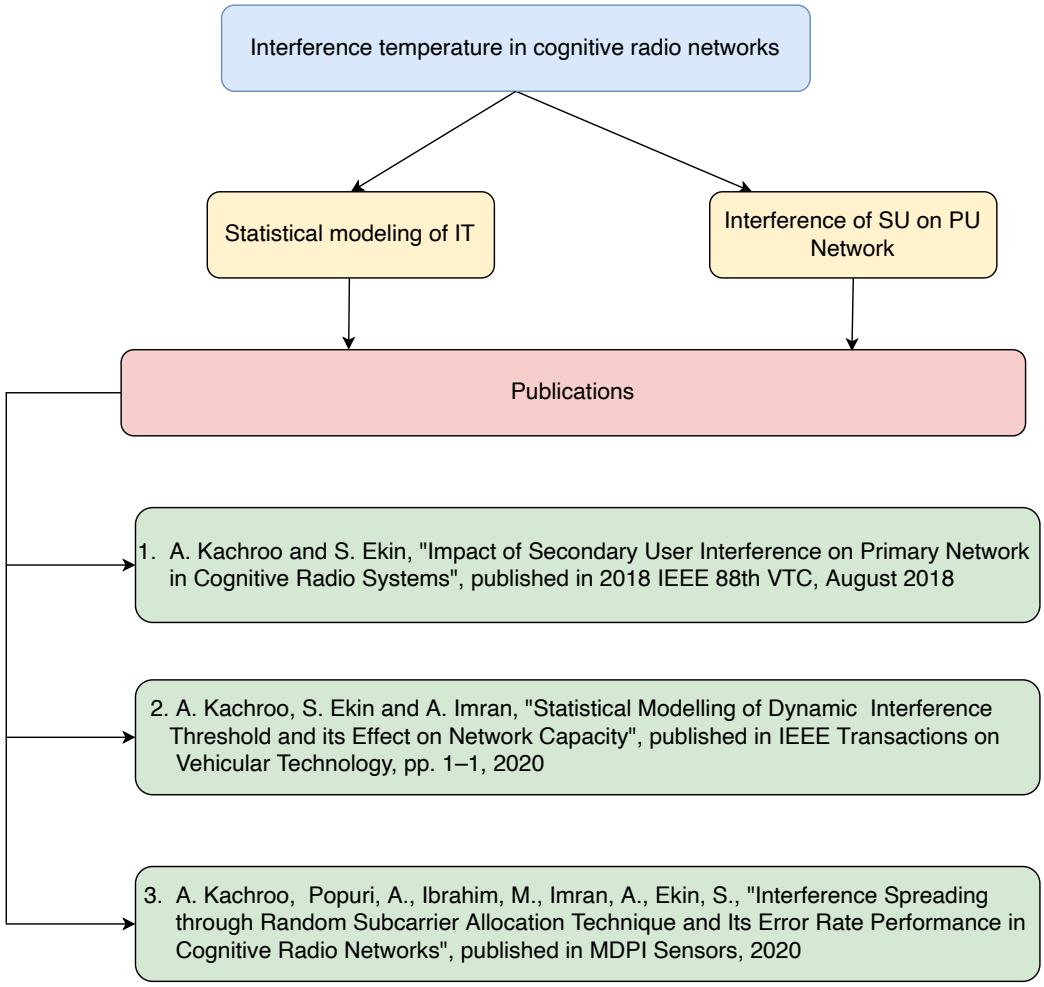

Figure 72: Cognitive radio networks- ideas with contribution.

is ultra-wideband (UWB) where the bandwidth ranges from 3.1-10.6 GHz. The application of UAVs in wireless communication network is a very active research topic, and in this chapter, we use a UAV at UWB frequency to study and analyze the channel between wearable antennas and a UAV. The different distance dependent and frequency dependent path loss factors were studied and determined in an indoor warehouse environment. Also, the time dispersion characteristics, such as root mean square, mean excess delay and maximum excess delay were studied and evaluated accordingly. Utilizing second-order Akakai Information Criteria as best fit distribution test, it was concluded that the fading statistics at ultra-wide band frequencies can be modelled as a Log-normal distribution. This preliminary study of UAV2W is one of the first to consider a human subject, and will help system designers in link budget calculations for applications of unmanned aerial vehicles in warehouse environment or in health care domain. Fig. 73 shows the problem/idea with the contributions to this UAV-assisted UAV2W-UWB communication system.

Finally, in Chapter IV, we moved to another high frequency part of the spectrum, 28 GHz or millimeter waves in UAV-assisted wireless communication systems. Apart from many challenges with UAV-assisted communications at high frequencies, a realistic channel

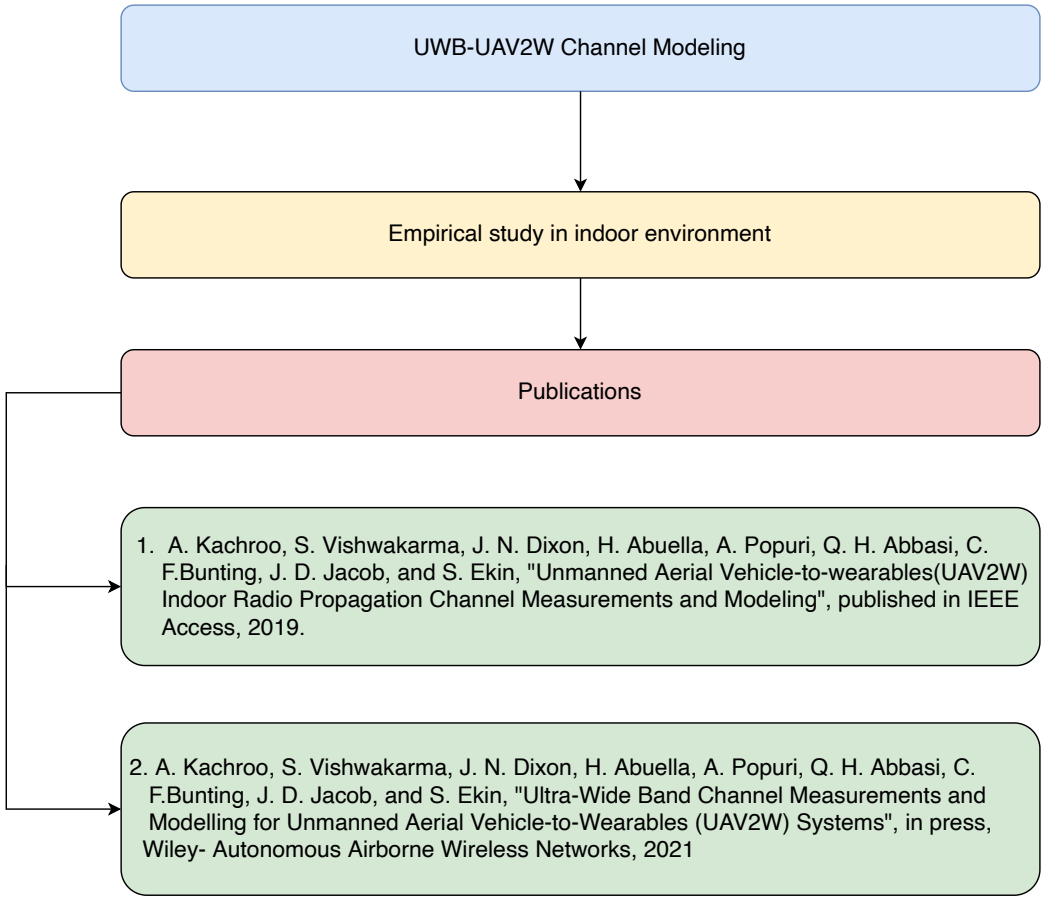

Figure 73: UAV2W-UWB communication systems- ideas and contribution.

model based on field data that considers UAV dynamics is missing. We closed this gap by proposing, and using a novel emulation framework with the help of robotics to generate close to field data by emulation. A robotic arm is used to emulate the actual UAV motion under wind gusts in an anechoic chamber environment. This method is very close to actual field data and does not rely on simulations that are mainly based on ray tracing software which neglect the UAV dynamics.

The wind gusts in this case are modelled by the famous Dryden wind model. In addition to that, to take care of the motion artifacts induced by the cable motion during the experiments, de-embedding method was used in time domain measurements for the first time in such a scenario. The S-parameters of cable (moving) was determined and it was removed from the measured data to have only the channel related measurement data. The method and the corresponding details are mentioned in detail in Chapter IV. Doppler measurements were conducted at the noise floor of -60 dB, and it was found that the Doppler spread is around ± 20 Hz in our case. The wide-sense stationary with uncorrelated scattering (WSSUS) conditions were found to be true in the anechoic chamber setting, but it was also determined that this can't be generalized to any other environment by examining a sample indoor measurement that showed that these WSSUS conditions are not true.

No-motion data points were then selected to determine the path loss exponent in this anechoic chamber environment, which in our scenario came out to be 1.843. In the later

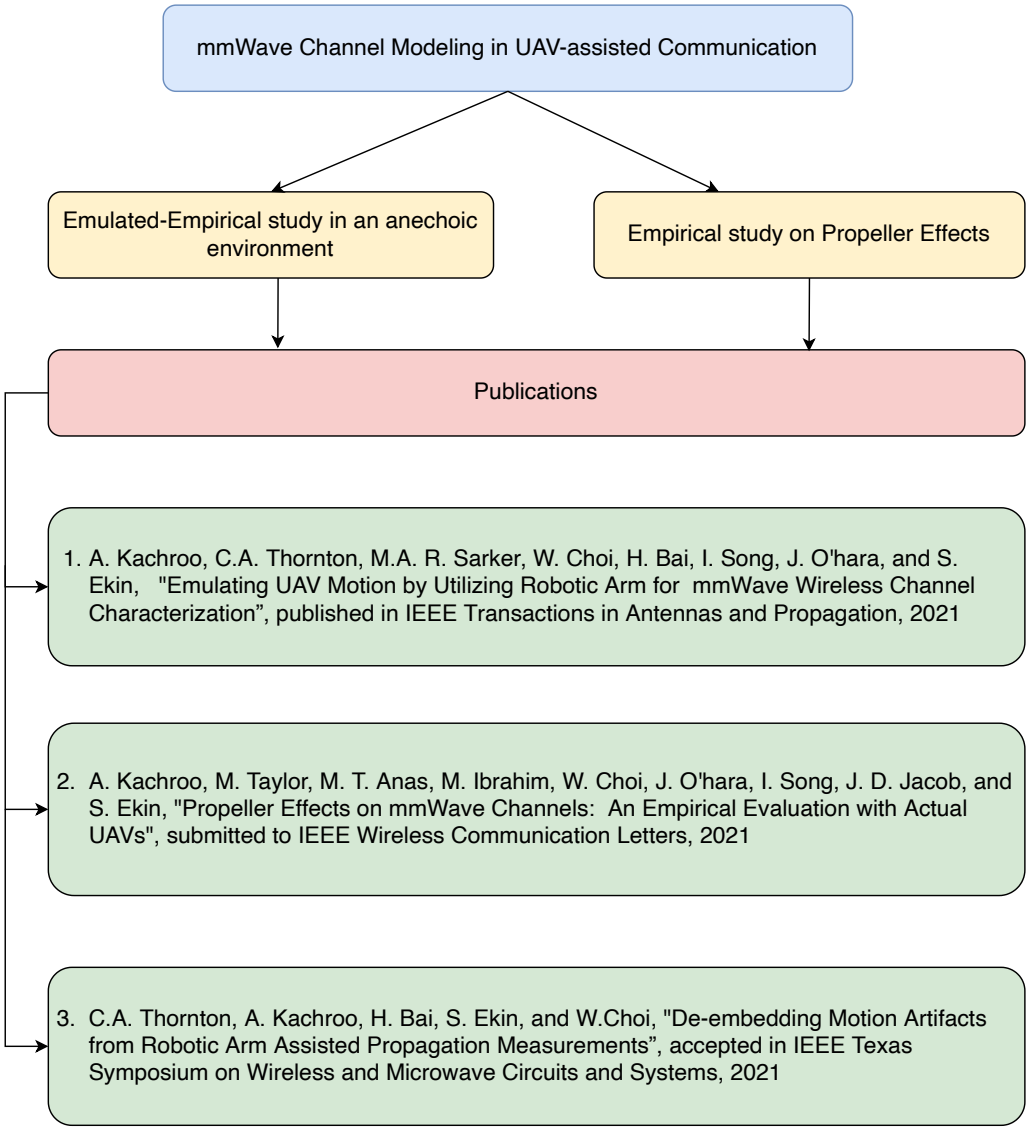

Figure 74: UAV-assisted mmWave communication systems- ideas and contribution.

part of this chapter, propeller effects were studied empirically in an outdoor environment with an actual UAV (hexcopter). A test setup with different height configurations, antenna configurations and with different UAV speed modes was planned and executed. As expected, the well known propeller modulation was observed in the spectrum in these cases which is periodic in nature. The fundamental frequency in our case was found to be at 52 Hz at idle speed mode, and at 125 Hz at high speed mode irrespective of different heights and antenna configuration. Another frequency component was also observed at idle speed which was later on attributed to the measurement setup itself, which is also examined in detail in Chapter IV. These results in Chapter IV are the very first steps towards realizing and developing a mmWave based UAV communication system in the near future. Fig. 74 shows a top view of the problem/idea with the contributions to this UAV-assisted mmWave communication system.

However, statistical analysis and channel modeling in next generation wireless systems

is a very involved and complex subject in its own right. Firstly, the statistical modelling of dynamic interference temperature in cognitive radio networks involves a lot of complex statistical transformations, and statistical modeling techniques that can be very challenging and the knowledge of stochastic processes is a must. In the second case of modeling of the UAV2W channel at UWB frequency, a lot of measurement data, knowledge of statistical and stochastic methods and process is very much desired to characterize channel models. However, any change in the wireless environment afterwards will not factor in the channel modelling part. The same is the case with the mmWave channel modeling. Also, apart from the hectic measurement campaign, deep knowledge of signal processing concepts and statistical modeling is very important. On the other hand, with the advancement of machine learning (ML) techniques and artificial intelligence, a high accuracy classification or prediction based on channel modeling can be achieved with online or offline learning. These are data driven models and are easy to implement as compared to the conventional statistical models. Furthermore, ML techniques have already been proposed and used in UAV-assisted mmWave communication systems. These techniques for wireless channel modeling should be studied in-depth and must be considered for the future work.

5.2 Future Work

In this section, we will delve into the details of ML concepts for wireless communication. Before introducing ML algorithms for wireless communication, it is very important to understand the difference between conventional modeling (classical programming) method and ML method. In conventional modeling, the system inputs rules (program) and data are to be processed (statistically modeled) according to these rules or assumptions, and the output is as per the rules. However, in ML, data with outputs (answers) is fed to the system, and rules are generated at the output [139]. In short, a ML system is trained to learn the rules with data and answers not programmed with rules. In detail, a ML system is fed data over many iterations, in which it tries to find statistical structure, and eventually comes up with rules. Technically, ML searches for useful representation of input data, within a constrained space, under guidance from a feedback signal. This feedback signal mechanism is implemented by backpropagation method. ML is classified into various categories, such as unsupervised learning, supervised learning, semi-supervised learning, and reinforcement learning (RL).

The advantage offered by the ML framework in the wireless networks operation is that it will enable network elements to monitor, learn, and predict various communication-related parameters, such as wireless channel behavior, traffic patterns, user context, and devices locations [140]. For the future work, ML techniques for the physical layer communication should be one of the prime focuses. At the physical layer, there are three broad areas where machine learning can be used, first is the wireless channel modeling part, second is the interference management and the last one is the spectrum allocation [140]. For the future work, interference modeling and mitigation in cognitive radio networks, channel modeling at UWB and mmWave frequencies using ML techniques is an interesting area. Recently, many research teams in academia as well as in industry have been working on this theme.

In particular, predicting wireless channel behaviour in a mobile dynamic environment can be one of the very interesting problems to solve in the future, especially in these UAV-assisted next generation wireless communication systems. Building an appropriate stochastic

channel model may not be as reliable as building a dynamic and evolving channel model in these dynamic settings. In that regards, ML can be the best available solution. Various ML techniques have been already proposed in prediction/estimation of the channel behaviour and in determining received signal strength (RSS) in UAV-assisted communications. In [140–142], authors used artificial neural networks (ANNs) and ensemble methods to predict the RSS in UAV-assisted systems. Measurements for LTE communication between UAV and BS were captured at different UAV height. The authors proposed to use a success-history-based adaptive algorithm for ANN training. This algorithm self-adapts the control parameters and performs linear population size reduction. In [142], the authors build upon their previous work on [141] and used ensemble methods to predict the RSS in UAV-assisted LTE communication.

In [143], unsupervised learning for real-time three-dimensional wireless channel modeling for air to ground was proposed. The biggest advantage of this approach was that the changes in the communication environment were integrated in the model itself, thereby, increasing the overall accuracy. However, it does not consider the shadowing part. There are other works that consider the simulation based approach to do channel modeling using machine learning techniques, but they are very unrealistic in nature and exclude the dynamic environment part. In the future work, measurement campaign data collected during the research experiments in Chapter III and IV with simulation data from network simulator can be used together to create a realistic training and testing data set for ML to predict/estimate dynamic channels. Transfer learning from the previous mentioned work with the recent advanced ML algorithms can also be implemented and compared in terms of performance. It is expected that since channel modeling is highly time or sequence dependent, a hybrid approach of using ANN with recurrent neural networks (RNN) such as long short term memory (LSTM) may outperform the present ML algorithms for channel modeling/estimation.

5.3 List of Publications

The detailed list of publications out of this thesis work is listed as follows,

1. A. Kachroo, C.A. Thornton, M.A. R. Sarker, W. Choi, H. Bai, I. Song, J. O'hara, and S. Ekin, "Emulating UAV Motion by Utilizing Robotic Arm for mmWave Wireless Channel Characterization", accepted in *IEEE Transactions on Antenna and Propagation*, 2021.

2. A. Kachroo, S. Vishwakarma, J. N. Dixon, H. Abuella, A. Popuri, Q. H. Abbasi, C. F.Bunting, J. D. Jacob, and S. Ekin, "Ultra-Wide Band Channel Measurements and Modelling for Unmanned Aerial Vehicle-to-Wearables (UAV2W) Systems," published as a book chapter in *Wiley- Autonomous Airborne Wireless Networks* , 2021.

3. A. Kachroo, M. Taylor, M. T. Anas, M. Ibrahim, W. Choi, J. O'hara, I. Song, J. D. Jacob, and S. Ekin, "Propeller Effects on mmWave Channels: An Empirical Evaluation with Actual UAVs", submitted to *IEEE Wireless Communication Letters*, 2021.

4. C.A. Thornton, A. Kachroo, H. Bai, S. Ekin, and W.Choi, "De-embedding Motion Artifacts from Robotic Arm Assisted Propagation Measurements", submitted to *IEEE Texas Symposium on Wireless and Microwave Circuits and Systems*, 2021.

5. A. Kachroo, S. Ekin, and A. Imran, "Statistical Modelling of Dynamic Interference Threshold and its Effect on Network Capacity", published in *IEEE Transactions on Vehicular Technology*, pp. 1–1, 2020.

6. A. Kachroo, A. Popuri, M. Ibrahim, A. Imran, S. Ekin, "Interference Spreading through Random Subcarrier Allocation Technique and Its Error Rate Performance in Cognitive Radio Networks", published in *MDPI Sensors*, 2020.

7. A. Kachroo, S. Vishwakarma, J. N. Dixon, H. Abuella, A. Popuri, Q. H. Abbasi, C. F.Bunting, J. D. Jacob, and S. Ekin, "Unmanned Aerial Vehicle-to-wearables(UAV2W) Indoor Radio Propagation Channel Measurements and Modeling," published in *IEEE Access*, vol. 7, pp. 73 741–73 750, 2019.

8. A. Kachroo and S. Ekin, "Impact of Secondary User Interference on Primary Network inCognitive Radio Systems," published in *2018 IEEE 88th Vehicular Technology Conference (VTC-Fall)*, Aug 2018, pp. 1–5.

REFERENCES

[1] J. Mitola, "Cognitive radio," *Licentiate proposal, KTH*, PhD thesis, Stockholm, Sweden 1998.

[2] J. Mitola and G. Q. Maguire, "Cognitive radio: making software radios more personal," *IEEE personal communications*, vol. 6, no. 4, pp. 13–18, 1999.

[3] S. Haykin, "Cognitive radio: brain-empowered wireless communications," *IEEE journal on selected areas in communications*, vol. 23, no. 2, pp. 201–220, 2005.

[4] K. Sithamparanathan and A. Giorgetti, *Cognitive radio techniques: spectrum sensing, interference mitigation, and localization*. Artech house, 2012.

[5] R. Zhang, S. Cui, and Y.-C. Liang, "On ergodic sum capacity of fading cognitive multiple-access and broadcast channels," *IEEE Transactions on Information Theory*, vol. 55, no. 11, pp. 5161–5178, 2009.

[6] R. Zhang and Y.-C. Liang, "Investigation on multiuser diversity in spectrum sharing based cognitive radio networks," *IEEE Communications Letters*, vol. 14, no. 2, 2010.

[7] Y.-U. Jang, "Performance analysis of cognitive radio networks based on sensing and secondary-to-primary interference," *IEEE Transactions on Signal Processing*, vol. 59, no. 11, pp. 5663–5668, 2011.

[8] A. Kachroo and S. Ekin, "Impact of Secondary User Interference on Primary Network in Cognitive Radio Systems," in *2018 IEEE 88th Vehicular Technology Conference (VTC-Fall)*, pp. 1–5, Aug 2018.

[9] H. Tran, M. A. Hagos, M. Mohamed, and H.-J. Zepernick, "Impact of primary networks on the performance of secondary networks," in *Computing, Management and Telecommunications (ComManTel), 2013 International Conference on*, pp. 43–48, IEEE, 2013.

[10] T. W. Ban, W. Choi, B. C. Jung, and D. K. Sung, "Multi-user diversity in a spectrum sharing system," *IEEE Transactions on Wireless Communications*, vol. 8, no. 1, pp. 102–106, 2009.

[11] R. Zhang, "On peak versus average interference power constraints for protecting primary users in cognitive radio networks," *IEEE Transactions on Wireless Communications*, vol. 8, no. 4, 2009.

[12] J. Chen, J. Si, Z. Li, and H. Huang, "On the performance of spectrum sharing cognitive relay networks with imperfect CSI," *IEEE Communications Letters*, vol. 16, no. 7, pp. 1002–1005, 2012.

[13] A. Kachroo, S. Ekin, and A. Imran, "Statistical modelling of dynamic interference threshold and its effect on network capacity," *IEEE Transactions on Vehicular Technology*, pp. 1–1, 2020.

[14] H. Price, "Federal Aviation Administration (FAA) Forecast Fiscal Years 2017-2038," *Accessed: 14 Feb 2021*, vol. 25, p. 2019, 2018.

[15] "3GPP." Technical specification group radio access network; Study on enhanced LTE support for aerial vehicles (release 15), Dec. 2017. Accessed: 2020-12-25.

[16] "3GPP." New SID on Enhanced Support for Aerial Vehicles, Tokyo, Japan, Mar. 2017. Accessed: 2020-12-25.

[17] "3GPP." Study on channel model for frequencies from 0.5 to 100 GHz (release 14), May 2017. Accessed: 2020-12-25.

[18] "ECC." Technical and regulatory aspects and the needs for spectrum regulation for unmanned aircraft systems (UAS),Electron. Commun. Committee, Copenhagen, Denmark, ECC Rep. 268, Feb. 2018. Accessed: 2020-12-25.

[19] "ITU-T." Functional Architecture for Unmanned Aerial Vehicles and Unmanned Aerial Vehicle Controllers Using IMT-2020 Networks, ITU-T, Geneva, Switzerland, 2017. Accessed: 2020-12-25.

[20] "ETSI." Use cases and spectrum considerations for UAS (unmanned aircraft systems), ETSI, Sophia Antipolis, France, Rep. 103 373, Feb. 2018. Accessed: 2020-12-25.

[21] "IEEE." Standard for Consumer Drones: Taxonomy and Definitions, IEEE Standard P2025.1, Oct. 2015. Accessed: 2020-12-25.

[22] "IEEE." Standard for Consumer Drones: Privacy and Security, IEEE Standard P2025.1, Oct. 2015. Accessed: 2020-12-25.

[23] L. Zhang, H. Zhao, S. Hou, Z. Zhao, H. Xu, X. Wu, Q. Wu, and R. Zhang, "A survey on 5G millimeter wave communications for UAV-assisted wireless networks," *IEEE Access*, vol. 7, pp. 117460–117504, 2019.

[24] M. Mozaffari, W. Saad, M. Bennis, Y.-H. Nam, and M. Debbah, "A tutorial on UAVs for wireless networks: Applications, challenges, and open problems," *IEEE Communications Surveys & Tutorials*, 2019.

[25] Y. Zeng, R. Zhang, and T. J. Lim, "Wireless communications with unmanned aerial vehicles: Opportunities and challenges," *IEEE Communications Magazine*, vol. 54, no. 5, pp. 36–42, 2016.

[26] S. Sekander, H. Tabassum, and E. Hossain, "Multi-tier drone architecture for 5G/B5G cellular networks: Challenges, trends, and prospects," *IEEE Communications Magazine*, vol. 56, no. 3, pp. 96–103, 2018.

[27] E. Vinogradov, H. Sallouha, S. De Bast, M. M. Azari, and S. Pollin, "Tutorial on UAV: A Blue Sky View on Wireless Communication," *arXiv preprint arXiv:1901.02306*, 2019.

[28] D. López-Pérez, M. Ding, H. Li, L. G. Giordano, G. Geraci, A. Garcia-Rodriguez, Z. Lin, and M. Hassan, "On the downlink performance of UAV communications in dense cellular networks," in *2018 IEEE Global Communications Conference (GLOBECOM)*, pp. 1–7, IEEE, 2018.

[29] C. Liu, M. Ding, C. Ma, Q. Li, Z. Lin, and Y.-C. Liang, "Performance analysis for practical unmanned aerial vehicle networks with LoS/NLoS transmissions," in *2018 IEEE International Conference on Communications Workshops (ICC Workshops)*, pp. 1–6, IEEE, 2018.

[30] M. Mozaffari, W. Saad, M. Bennis, and M. Debbah, "Drone small cells in the clouds: Design, deployment and performance analysis," in *2015 IEEE global communications conference (GLOBECOM)*, pp. 1–6, IEEE, 2015.

[31] M. Mozaffari, W. Saad, M. Bennis, and M. Debbah, "Unmanned aerial vehicle with underlaid device-to-device communications: Performance and tradeoffs," *IEEE Transactions on Wireless Communications*, vol. 15, no. 6, pp. 3949–3963, 2016.

[32] M. Mozaffari, W. Saad, M. Bennis, and M. Debbah, "Efficient deployment of multiple unmanned aerial vehicles for optimal wireless coverage," *IEEE Communications Letters*, vol. 20, no. 8, pp. 1647–1650, 2016.

[33] E. Yanmaz, R. Kuschnig, M. Quaritsch, C. Bettstetter, and B. Rinner, "On path planning strategies for networked unmanned aerial vehicles," in *2011 IEEE Conference on Computer Communications Workshops (INFOCOM WKSHPS)*, pp. 212–216, IEEE, 2011.

[34] V. Sharma, K. Srinivasan, H.-C. Chao, K.-L. Hua, and W.-H. Cheng, "Intelligent deployment of UAVs in 5G heterogeneous communication environment for improved coverage," *Journal of Network and Computer Applications*, vol. 85, pp. 94–105, 2017.

[35] Federal Aviation Administration, "FAA small unmanned aircraft regulations," 2020. accessed 2020-04-01.

[36] M. M. Khan, Q. H. Abbasi, A. Alomainy, and Y. Hao, "Performance of ultrawideband wireless tags for on-body radio channel characterization," *Hindawi international journal of antennas and propagation*, 2012.

[37] M. M. Khan, Q. H. Abbasi, A. Alomainy, Y. Hao, and C. Parini, "Experimental characterisation of ultra-wideband off-body radio channels considering antenna effects," *IET Microwaves, Antennas & Propagation*, vol. 7, no. 5, pp. 370–380, 2013.

[38] P. S. Hall and Y. Hao, "Antennas and propagation for body centric communications," in *First European Conference on Antennas and Propagation, 2006. EuCAP 2006.*, pp. 1–7, IEEE, 2006.

[39] J. Foerster, E. Green, S. Somayazulu, D. Leeper, *et al.*, "Ultra-wideband technology for short-or medium-range wireless communications," in *Intel technology journal*, Citeseer, 2001.

[40] Q. H. Abbasi, M. U. Rehman, K. Qaraqe, and A. Alomainy, *Advances in body-centric wireless communication: Applications and state-of-the-art*. Institution of Engineering and Technology, 2016.

[41] A. Alomainy, R. Di Bari, Q. H. Abbasi, and Y. Chen, *Co-operative and energy efficient body area and wireless sensor networks for healthcare applications*. Academic Press, 2014.

[42] A. Kachroo, S. Vishwakarma, J. N. Dixon, H. Abuella, A. Popuri, Q. H. Abbasi, C. F. Bunting, J. D. Jacob, and S. Ekin, "Unmanned aerial vehicle-to-wearables (uav2w) indoor radio propagation channel measurements and modeling," *IEEE Access*, vol. 7, pp. 73741–73750, 2019.

[43] B. Allen, M. Dohler, E. Okon, W. Malik, A. Brown, and D. Edwards, "UWB antenna and propagation for communications, radar and imaging. hoboken," 2007.

[44] 5G Spectrum Recommendations Bellevue WA USA Apr. 2017, 2017.

[45] T. S. Rappaport, S. Sun, R. Mayzus, H. Zhao, Y. Azar, K. Wang, G. N. Wong, J. K. Schulz, M. Samimi, and F. Gutierrez, "Millimeter wave mobile communications for 5G cellular: It will work!," *IEEE access*, vol. 1, pp. 335–349, 2013.

[46] I. A. Hemadeh, K. Satyanarayana, M. El-Hajjar, and L. Hanzo, "Millimeter-wave communications: Physical channel models, design considerations, antenna constructions, and link-budget," *IEEE Communications Surveys & Tutorials*, vol. 20, no. 2, pp. 870–913, 2017.

[47] G. A. Siles, J. M. Riera, and P. Garcia-del Pino, "Atmospheric attenuation in wireless communication systems at millimeter and THz frequencies [Wireless Corner]," *IEEE Antennas and Propagation Magazine*, vol. 57, no. 1, pp. 48–61, 2015.

[48] H. Hassanieh, O. Abari, M. Rodriguez, M. Abdelghany, D. Katabi, and P. Indyk, "Fast millimeter wave beam alignment," in *Proceedings of the 2018 Conference of the ACM Special Interest Group on Data Communication*, pp. 432–445, ACM, 2018.

[49] W. Khawaja, I. Guvenc, D. W. Matolak, U.-C. Fiebig, and N. Schneckenberger, "A survey of air-to-ground propagation channel modeling for unmanned aerial vehicles," *IEEE Communications Surveys & Tutorials*, 2019.

[50] D. Datla, A. M. Wyglinski, and G. J. Minden, "A spectrum surveying framework for dynamic spectrum access networks," *IEEE Transactions on Vehicular Technology*, vol. 58, no. 8, pp. 4158–4168, 2009.

[51] M. H. Islam, C. L. Koh, S. W. Oh, X. Qing, Y. Y. Lai, C. Wang, Y.-C. Liang, B. E. Toh, F. Chin, G. L. Tan, *et al.*, "Spectrum survey in Singapore: Occupancy measurements and analyses," in *2008 3rd International Conference on Cognitive Radio Oriented Wireless Networks and Communications (CrownCom 2008)*, pp. 1–7, IEEE, 2008.

[52] F. C. Commission *et al.*, "Spectrum policy task force report, FCC 02-155," 2002.

[53] T. Erpek, M. Lofquist, and K. Patton, "Spectrum Occupancy Measurements Loring Commerce Centre Limestone, Maine September 18-20, 2007," *The Shared Spectrum Company*, 2007.

[54] Y. Cao, N. Zhao, F. R. Yu, M. Jin, Y. Chen, J. Tang, and V. C. M. Leung, "Optimization or Alignment: Secure Primary Transmission Assisted by Secondary Networks," *IEEE Journal on Selected Areas in Communications*, vol. 36, pp. 905–917, April 2018.

[55] P. J. Kolodzy, "Interference temperature: a metric for dynamic spectrum utilization," *International Journal of Network Management*, vol. 16, no. 2, pp. 103–113, 2006.

[56] S. Ekin, M. M. Abdallah, K. A. Qaraqe, and E. Serpedin, "Random subcarrier allocation in OFDM-based cognitive radio networks," *IEEE Transactions on Signal Processing*, vol. 60, no. 9, pp. 4758–4774, 2012.

[57] L. Musavian and S. Aïssa, "Capacity and power allocation for spectrum-sharing communications in fading channels," *IEEE Transactions on Wireless Communications*, vol. 8, no. 1, pp. 148–156, 2009.

[58] X. Kang, R. Zhang, Y. Liang, and H. K. Garg, "Optimal Power Allocation Strategies for Fading Cognitive Radio Channels with Primary User Outage Constraint," *IEEE Journal on Selected Areas in Communications*, vol. 29, pp. 374–383, February 2011.

[59] S. Srinivasa and S. A. Jafar, "Soft Sensing and Optimal Power Control for Cognitive Radio," *IEEE Transactions on Wireless Communications*, vol. 9, pp. 3638–3649, December 2010.

[60] A. Tsakmalis, S. Chatzinotas, and B. Ottersten, "Interference constraint active learning with uncertain feedback for cognitive radio networks," *IEEE Transactions on Wireless Communications*, vol. 16, no. 7, pp. 4654–4668, 2017.

[61] Y. Noam and A. J. Goldsmith, "The one-bit null space learning algorithm and its convergence," *IEEE Transactions on Signal Processing*, vol. 61, no. 24, pp. 6135–6149, 2013.

[62] B. Gopalakrishnan and N. D. Sidiropoulos, "Cognitive transmit beamforming from binary CSIT," *IEEE Transactions on Wireless Communications*, vol. 14, no. 2, pp. 895–906, 2015.

[63] A. Tsakmalis, S. Chatzinotas, and B. Ottersten, "Centralized power control in cognitive radio networks using modulation and coding classification feedback," *IEEE Transactions on Cognitive Communications and Networking*, vol. 2, no. 3, pp. 223–237, 2016.

[64] Tsakmalis, Anestis and Chatzinotas, Symeon and Ottersten, Björn, "Modulation and coding classification for adaptive power control in 5g cognitive communications," in *Proceedings of IEEE International Workshop on Signal Processing Advances in Wireless Communications*, 2014.

[65] X. Li, N. Zhao, Y. Sun, and F. R. Yu, "Interference Alignment Based on Antenna Selection With Imperfect Channel State Information in Cognitive Radio Networks," *IEEE Transactions on Vehicular Technology*, vol. 65, pp. 5497–5511, July 2016.

[66] B. Sklar, "Rayleigh fading channels in mobile digital communication systems .I. Characterization," *IEEE Communications Magazine*, vol. 35, pp. 90–100, July 1997.

[67] A. Goldsmith, *Wireless communications*. Cambridge university press, 2005.

[68] V. S. Frost and B. Melamed, "Traffic modeling for telecommunications networks," *IEEE Communications Magazine*, vol. 32, no. 3, pp. 70–80, 1994.

[69] J. Cao, W. S. Cleveland, D. Lin, and D. X. Sun, "Internet traffic tends toward Poisson and independent as the load increases," in *Nonlinear estimation and classification*, pp. 83–109, Springer, 2003.

[70] J. Chen, R. G. Addie, M. Zukerman, and T. D. Neame, "Performance evaluation of a queue fed by a Poisson Lomax Burst process," *IEEE Communications Letters*, vol. 19, no. 3, pp. 367–370, 2015.

[71] K. Atefi, S. Yahya, A. Rezaei, and A. Erfanian, "Traffic behavior of Local Area Network based on M/M/1 queuing model using poisson and exponential distribution," in *Region 10 Symposium (TENSYMP), 2016 IEEE*, pp. 19–23, IEEE, 2016.

[72] S. Zhang, Z. Zhao, H. Guan, and H. Yang, "A modified poisson distribution for smartphone background traffic in cellular networks," *International Journal of Communication Systems*, vol. 30, no. 6, p. e3117, 2017.

[73] B. Mandelbrot, "Self-similar error clusters in communication systems and the concept of conditional stationarity," *IEEE Transactions on Communication Technology*, vol. 13, no. 1, pp. 71–90, 1965.

[74] V. S. Frost and B. Melamed, "Traffic modeling for telecommunications networks," *IEEE Communications Magazine*, vol. 32, no. 3, pp. 70–81, 1994.

[75] M. López-Benítez and F. Casadevall, "Time-dimension models of spectrum usage for the analysis, design, and simulation of cognitive radio networks," *IEEE transactions on vehicular technology*, vol. 62, no. 5, pp. 2091–2104, 2013.

[76] G. Ding, Y. Jiao, J. Wang, Y. Zou, Q. Wu, Y.-D. Yao, and L. Hanzo, "Spectrum inference in cognitive radio networks: Algorithms and applications," *IEEE Communications Surveys & Tutorials*, vol. 20, no. 1, pp. 150–182, 2017.

[77] A. Papoulis and S. U. Pillai, *Probability, random variables, and stochastic processes*. Tata McGraw-Hill Education, 2002.

[78] S. Miller and D. Childers, *Probability and random processes: With applications to signal processing and communications*. Academic Press, 2012.

[79] H. Pishro-Nik, *Introduction to probability, statistics, and random processes*. Kappa Research LLC, 2014.

[80] T. F. Griffin, "Distribution of the ratio of two poisson random variables," Master's thesis, Texas Tech University, 1992.

[81] J. Singh, "A characterization of positive poisson distribution and its statistical application," *SIAM Journal on Applied Mathematics*, vol. 34, no. 3, pp. 545–548, 1978.

[82] A. C. Cohen, "Estimating the parameter in a conditional Poisson distribution," *Biometrics*, vol. 16, no. 2, pp. 203–211, 1960.

[83] H. A. Suraweera, P. J. Smith, and M. Shafi, "Capacity limits and performance analysis of cognitive radio with imperfect channel knowledge," *IEEE Transactions on Vehicular Technology*, vol. 59, no. 4, pp. 1811–1822, 2010.

[84] A. Kachroo, S. Ekin, and A. Imran, "Statistical modelling of dynamic interference threshold and its effect on network capacity," *IEEE Transactions on Vehicular Technology*, pp. 1–1, 2020.

[85] M. Abramowitz and I. A. Stegun, *Handbook of mathematical functions: with formulas, graphs, and mathematical tables*, vol. 55. Courier Corporation, 1965.

[86] J. H. Curtiss, "On the Distribution of the Quotient of Two Chance Variables," *The Annals of Mathematical Statistics*, no. 4, pp. 409–421, 1941.

[87] M. Schootman, E. Nelson, K. Werner, E. Shacham, M. Elliott, K. Ratnapradipa, M. Lian, and A. McVay, "Emerging technologies to measure neighborhood conditions in public health: implications for interventions and next steps," *International journal of health geographics*, vol. 15, no. 1, p. 20, 2016.

[88] M. J. Lum, J. Rosen, H. King, D. C. Friedman, G. Donlin, G. Sankaranarayanan, B. Harnett, L. Huffman, C. Doarn, T. Broderick, *et al.*, "Telesurgery via unmanned aerial vehicle (UAV) with a field deployable surgical robot," *Stud Health Technol Inform*, vol. 125, pp. 313–5, 2007.

[89] C. Todd, M. Watfa, Y. El Mouden, S. Sahir, A. Ali, A. Niavarani, A. Lutfi, A. Copiaco, V. Agarwal, K. Afsari, *et al.*, "A proposed UAV for indoor patient care," *Technology and Health Care*, no. Preprint, pp. 1–8, 2015.

[90] S. M. Bae, K. H. Han, C. N. Cha, and H. Y. Lee, "Development of inventory checking system based on uav and rfid in open storage yard," in *2016 International Conference on Information Science and Security (ICISS)*, pp. 1–2, IEEE, 2016.

[91] F. Guérin, F. Guinand, J.-F. Brethé, H. Pelvillain, *et al.*, "Towards an autonomous warehouse inventory scheme," in *2016 IEEE Symposium Series on Computational Intelligence (SSCI)*, pp. 1–8, IEEE, 2016.

[92] M. Fleck, "Usability of lightweight defibrillators for UAV delivery," in *Proceedings of the 2016 CHI Conference Extended Abstracts on Human Factors in Computing Systems*, pp. 3056–3061, ACM, 2016.

[93] P. Tatham, F. Stadler, A. Murray, and R. Z. Shaban, "Flying maggots: a smart logistic solution to an enduring medical challenge," *Journal of Humanitarian Logistics and Supply Chain Management*, vol. 7, no. 2, pp. 172–193, 2017.

[94] W. G. Patrick, "Request apparatus for delivery of medical support implement by UAV," Apr. 5 2016. US Patent 9,307,383.

[95] Z. H. Hu, Y. I. Nechayev, P. S. Hall, C. C. Constantinou, and Y. Hao, "Measurements and statistical analysis of on-body channel fading at 2.45 GHz," *IEEE Antennas and Wireless Propagation Letters*, vol. 6, pp. 612–615, 2007.

[96] A. Alomainy, Y. Hao, A. Owadally, C. G. Parini, Y. Nechayev, C. C. Constantinou, and P. S. Hall, "Statistical analysis and performance evaluation for on-body radio propagation with microstrip patch antennas," *IEEE Transactions on Antennas and Propagation*, vol. 55, no. 1, pp. 245–248, 2007.

[97] Y. I. Nechayev, Z. H. Hu, and P. S. Hall, "Short-term and long-term fading of on-body transmission channels at 2.45 ghz," in *Antennas & Propagation Conference, 2009. LAPC 2009. Loughborough*, pp. 657–660, IEEE, 2009.

[98] Q. H. Abbasi, A. Sani, A. Alomainy, and Y. Hao, "Arm movements effect on ultra wideband on-body propagation channels and radio systems," in *IEEE Antennas & Propagation Conference, 2009*, pp. 261–264, IEEE, 2009.

[99] Q. Hussain Abbasi, A. Sani, A. Alomainy, and Y. Hao, "On-body radio channel characterization and system-level modeling for multiband OFDM ultra-wideband body-centric wireless network," *IEEE Transactions on Microwave Theory and Techniques*, vol. 58, no. 12, pp. 3485–3492, 2010.

[100] A. Alomainy, Q. H. Abbasi, A. Sani, and Y. Hao, "System-level modelling of optimal ultra wideband body-centric wireless network," in *Microwave Conference, 2009. APMC 2009. Asia Pacific*, pp. 2188–2191, IEEE, 2009.

[101] W. Khawaja, I. Guvenc, and D. Matolak, "UWB channel sounding and modeling for UAV air-to-ground propagation channels," in *Global Communications Conference (GLOBECOM), 2016 IEEE*, pp. 1–7, IEEE, 2016.

[102] J. Tiemann, F. Schweikowski, and C. Wietfeld, "Design of an UWB indoor-positioning system for UAV navigation in GNSS-denied environments," in *Indoor Positioning and Indoor Navigation (IPIN), 2015 International Conference on*, pp. 1–7, IEEE, 2015.

[103] "Octane Ultra-wideband antenna (BW-3000-10000-EG)." `http://www.pharad.com/pdf/UWB-Wearable-Antenna-Datasheet-Enhanced-Gain.pdf`, 2019.

[104] "3DR drones." `https://3dr.com/products/supported-drones/`, 2019.

[105] A. F. Molisch, "Ultra-wide-band propagation channels," *Proceedings of the IEEE*, vol. 97, no. 2, pp. 353–371, 2009.

[106] A. F. Molisch, D. Cassioli, C.-C. Chong, S. Emami, A. Fort, B. Kannan, J. Karedal, J. Kunisch, H. G. Schantz, K. Siwiak, *et al.*, "A comprehensive standardized model for ultrawideband propagation channels," *IEEE Transactions on Antennas and Propagation*, vol. 54, no. 11, pp. 3151–3166, 2006.

[107] C. G. Spiliotopoulos and A. G. Kanatas, "Channel measurements and modelling in a military cargo airplane," *Progress In Electromagnetics Research B*, vol. 26, pp. 69–100, 2010.

[108] C.-C. Chong, Y.-E. Kim, S. K. Yong, and S.-S. Lee, "Statistical characterization of the uwb propagation channel in indoor residential environment," *Wireless Communications and Mobile Computing*, vol. 5, no. 5, pp. 503–512, 2005.

[109] J. Karedal, S. Wyne, P. Almers, F. Tufvesson, and A. F. Molisch, "A measurement-based statistical model for industrial ultra-wideband channels," *IEEE transactions on wireless communications*, vol. 6, no. 8, pp. 3028–3037, 2007.

[110] A. Fort, C. Desset, P. De Doncker, P. Wambacq, and L. Van Biesen, "An ultra-wideband body area propagation channel model-from statistics to implementation," *IEEE Transactions on Microwave Theory and Techniques*, vol. 54, no. 4, pp. 1820–1826, 2006.

[111] K. P. Burnham and D. R. Anderson, *Model selection and multimodel inference: a practical information-theoretic approach*. Springer Science & Business Media, 2003.

[112] X. Hong, J. Wang, C.-X. Wang, and J. Shi, "Cognitive radio in 5G: a perspective on energy-spectral efficiency trade-off," *IEEE Communications Magazine*, vol. 52, no. 7, pp. 46–53, 2014.

[113] L. Liang, W. Xu, and X. Dong, "Low-complexity hybrid precoding in massive multiuser MIMO systems," *IEEE Wireless Communications Letters*, vol. 3, no. 6, pp. 653–656, 2014.

[114] Z. Ding, X. Lei, G. K. Karagiannidis, R. Schober, J. Yuan, and V. K. Bhargava, "A survey on non-orthogonal multiple access for 5G networks: Research challenges and future trends," *IEEE Journal on Selected Areas in Communications*, vol. 35, no. 10, pp. 2181–2195, 2017.

[115] C. Zhang and J. M. Kovacs, "The application of small unmanned aerial systems for precision agriculture: a review," *Precision agriculture*, vol. 13, no. 6, pp. 693–712, 2012.

[116] M. Erdelj, E. Natalizio, K. R. Chowdhury, and I. F. Akyildiz, "Help from the sky: Leveraging UAVs for disaster management," *IEEE Pervasive Computing*, vol. 16, no. 1, pp. 24–32, 2017.

[117] S. A. R. Naqvi, S. A. Hassan, H. Pervaiz, and Q. Ni, "Drone-aided communication as a key enabler for 5G and resilient public safety networks," *IEEE Communications Magazine*, vol. 56, no. 1, pp. 36–42, 2018.

[118] S. Hayat, E. Yanmaz, and R. Muzaffar, "Survey on unmanned aerial vehicle networks for civil applications: A communications viewpoint," *IEEE Communications Surveys & Tutorials*, vol. 18, no. 4, pp. 2624–2661, 2016.

[119] X. Wang, L. Kong, F. Kong, F. Qiu, M. Xia, S. Arnon, and G. Chen, "Millimeter wave communication: A comprehensive survey," *IEEE Communications Surveys & Tutorials*, vol. 20, no. 3, pp. 1616–1653, 2018.

[120] H. N. Qureshi and A. Imran, "On the tradeoffs between coverage radius, altitude, and beamwidth for practical uav deployments," *IEEE Transactions on Aerospace and Electronic Systems*, vol. 55, no. 6, pp. 2805–2821, 2019.

[121] G. R. MacCartney and T. S. Rappaport, "A flexible millimeter-wave channel sounder with absolute timing," *IEEE Journal on Selected Areas in Communications*, vol. 35, no. 6, pp. 1402–1418, 2017.

[122] X. Wu, Y. Zhang, C.-X. Wang, G. Goussetis, M. M. Alwakeel, *et al.*, "28 GHz indoor channel measurements and modelling in laboratory environment using directional antennas," in *2015 9th European Conference on Antennas and Propagation (EuCAP)*, pp. 1–5, IEEE, 2015.

[123] Dryden, *Flying qualities of piloted aircraft*. Department of Defense, 1990. MIL-STD-1797A.

[124] Dryden, *Flying qualities of piloted aircraft*. Department of Defense, 2012. MIL-HDBK-1791B.

[125] R. W. Beard and T. W. McLain, *Small Unmanned Aircraft - Theory and Practice*. Princeton University Press, 2012.

[126] T. Von Karman, "Progress in the statistical theory of turbulence," *Proceedings of the National Academy of Sciences*, vol. 34, no. 11, pp. 530–539, 1948.

[127] R. Beard, "Quadrotor dynamics and control rev 0.1," 2008.

[128] Allison, Sam and Bai, He and Jayaraman, Balaji, "Estimating Wind Velocity with a Neural Network using Quadcopter Trajectories," in *AIAA Scitech 2019 Forum*, p. 1596, 2019.

[129] S. Allison, H. Bai, and B. Jayaraman, "Wind Estimation Using Quadcopter Motion: A Machine Learning Approach," *arXiv preprint arXiv:1907.05720*, 2019.

[130] R. F. Bauer and P. Penfield, "De-embedding and unterminating," *IEEE Transactions on Microwave Theory and Techniques*, vol. 22, no. 3, pp. 282–288, 1974.

[131] "Adapter characterization." `http://na.support.keysight.com/pna/help/WebHelp10_25/Applications/CharacterizeAdaptor_Macro.htm`. Accessed: 2020-12-25.

[132] D. M. Pozar, *Microwave engineering*. John wiley & sons, 2011.

[133] G. R. MacCartney, S. Deng, and T. S. Rappaport, "Indoor Office Plan Environment and Layout-Based mmWave Path Loss Models for 28 GHz and 73 GHz," in *2016 IEEE 83rd Vehicular Technology Conference (VTC Spring)*, pp. 1–6, 2016.

[134] J. Senic, C. Gentile, P. B. Papazian, K. A. Remley, and J. K. Choi, "Analysis of E-Band Path Loss and Propagation Mechanisms in the Indoor Environment," *IEEE Transactions on Antennas and Propagation*, vol. 65, no. 12, pp. 6562–6573, 2017.

[135] A. Al-Samman, T. Rahman, M. Azmi, M. Hindia, I. Khan, and E. Hanafi, "Statistical modelling and characterization of experimental mm-wave indoor channels for future 5G wireless communication networks," *PloS one*, vol. 11, no. 9, p. e0163034, 2016.

[136] A. Dominek, W. Burnside, and W. Lin, "Scattering modulation of periodically rotating structure'," in *Annu. Meet. Symp. Antenna Measurement Tech. Assoc.*, pp. 3–24, 1989.

[137] C. R. Birtcher, C. A. Balanis, and D. Decarlo, "Rotor-blade modulation on antenna amplitude pattern and polarization: Predictions and measurements," *IEEE transactions on electromagnetic compatibility*, vol. 41, no. 4, pp. 384–393, 1999.

[138] J. Bredemeyer and T. Schrader, "Employing UAS to perform low altitude navaids measurements," in *International Flight Inspection Symposium (IFIS), Monterey, California*, 2018.

[139] F. Chollet, *Deep Learning with Python*. Greenwich, CT, USA: Manning Publications Co., 1st ed., 2017.

[140] P. S. Bithas, E. T. Michailidis, N. Nomikos, D. Vouyioukas, and A. G. Kanatas, "A survey on machine-learning techniques for uav-based communications," *Sensors*, vol. 19, no. 23, p. 5170, 2019.

[141] S. K. Goudos, G. V. Tsoulos, G. Athanasiadou, M. C. Batistatos, D. Zarbouti, and K. E. Psannis, "Artificial neural network optimal modeling and optimization of uav measurements for mobile communications using the l-shade algorithm," *IEEE Transactions on Antennas and Propagation*, vol. 67, no. 6, pp. 4022–4031, 2019.

[142] S. K. Goudos and G. Athanasiadou, "Application of an ensemble method to uav power modeling for cellular communications," *IEEE Antennas and Wireless Propagation Letters*, vol. 18, no. 11, pp. 2340–2344, 2019.

[143] J.-L. Wang, Y.-R. Li, A. B. Adege, L.-C. Wang, S.-S. Jeng, and J.-Y. Chen, "Machine learning based rapid 3d channel modeling for uav communication networks," in *2019 16th IEEE Annual Consumer Communications & Networking Conference (CCNC)*, pp. 1–5, IEEE, 2019.

APPENDICES

PROOF OF VALID PDF

For (2.3.12) to be a valid PDF, it should satisfy these two necessary conditions,

- $f_\psi(x) \geq 0, \ \forall x.$
- $\int_{-\infty}^{+\infty} f_\psi(x)dx = 1.$

where $f_\psi(x)$ is given as,

$$f_\psi(x) = \frac{\lambda_{pp}}{p} \sum_{\alpha_k \in \mathbb{R}^+} \frac{e^{-\lambda_p} \lambda_p^{\log(1+\alpha_k)}}{(1-e^{-\lambda_p}) \log(1+\alpha_k)!} \alpha_k e^{-\lambda_{pp}\alpha_k x/p}.$$

The first property is easy to prove. The second property can be proved as follows,

$$\int_0^\infty \frac{\lambda_{pp}}{p} \sum_{\alpha_k \in \mathbb{R}^+} \frac{e^{-\lambda_p} \lambda_p^{\log(1+\alpha_k)} \alpha_k}{(1-e^{-\lambda_p}) \log(1+\alpha_k)!} e^{-\lambda_{pp}\alpha_k x/p} dx = \frac{\lambda_{pp}}{p} \sum_{\alpha_k \in \mathbb{R}^+} \frac{e^{-\lambda_p} \lambda_p^{\log(1+\alpha_k)} \alpha_k}{(1-e^{-\lambda_p}) \log(1+\alpha_k)!}$$

$$\times \int_0^\infty e^{-\lambda_{pp}\alpha_k x/p} dx,$$

$$= \frac{e^{-\lambda_p}}{1-e^{-\lambda_p}} \sum_{\alpha_k \in \mathbb{R}^+} \frac{\lambda_p^{\log(1+\alpha_k)}}{\log(1+\alpha_k)!}.$$

Using Taylor series, the expression reduces to,

$$\int_0^\infty f_\psi(x)dx = \frac{e^{-\lambda_p}}{1-e^{-\lambda_p}}(e^{\lambda_p} - 1),$$
$$\int_0^\infty f_\psi(x)dx = 1.$$

Hence, it is a valid PDF.

PROOF OF VALID PDF

For (2.4.24) to be a valid CDF it should satisfy these two necessary conditions,

- $\lim_{x \to -\infty} F_{\gamma_s}(x)) = 0.$

- $\lim_{x\to\infty} F_{\gamma_s}(x)) = 1.$

where $F_{\gamma_s}(x))$ is given in (2.4.24). Now, at $x \to 0$ the second term in (2.4.24) will reduces to,

$$\frac{\lambda_{ps}}{\lambda_{ps} + \lambda_{ss}x} e^{-\frac{\lambda_{ss}\sigma^2 x}{p}} = 1. \tag{A.1}$$

while the third term is 0. Therefore $F_{\gamma_s}(x)) = 0$ as $x \to 0$. Evaluating at $x \to \infty$,

$$\begin{aligned} e^{-\frac{\lambda_{ss}\sigma^2 x}{p}} &= 0, \\ \Gamma(0, \infty) &= 0. \end{aligned} \tag{A.2}$$

Therefore, the second and third term in (2.4.24) becomes 0, and $F_{\gamma_s}(x))$ will be 1. Hence the expression is a valid CDF.

VITA

Amit Kachroo

Candidate for the Degree of

Doctor of Philosophy

Dissertation: STATISTICAL ANALYSIS AND CHANNEL MODELING IN NEXT GENERATION WIRELESS COMMUNICATION SYSTEMS

Major Field: Electrical Engineering

Biographical:

Education:

Completed the requirements for the Doctor of Philosophy in Electrical Engineering at Oklahoma State University, Stillwater, Oklahoma in May, 2021.

Completed the requirements for the Master of Science in Electronics and Computer Engineering at Istanbul Sehir University, Istanbul, Turkey in 2017.

Completed the requirements for the Bachelor of Technology in Electronics and Communication Engineering at National Institute of Technology, Srinagar, India in 2009.

Experience:

Applied Scientist Intern at Amazon Lab126, Summer 2021

Software Intern at Cadence Design Systems, Summer 2019

Project Engineer at Nokia Solutions and Networks, 2010-2014

Professional Membership:

IEEE student member